Technical Physics Letters, Vol. 28, No. 1, 2002, pp. 1–3. Translated from Pis'ma v Zhurnal Tekhnicheskoĭ Fiziki, Vol. 28, No. 1, 2002, pp. 3–10.

Thermal- and Field-Treatment Induced Reconstruction of a Carbon Fiber Crystal

V. M. Lobanov[a,*] and Yu. M. Yumaguzin[b,]**

[a] *Bashkir State University, Ufa, Bashkortostan, Russia*

** e-mail: rector@bsu.bashedu.ru*

[b] *Bashkir State Agricultural University, Ufa, Bashkortostan, Russia*

*** e-mail: bgau@soros.bashedu.ru*

Received June 18, 2001

Abstract—A carbon (PAN) fiber crystal was studied in a field electron microscope equipped with a dispersive energy analyzer. Annealing of the emitter crystal at a temperature of 750°C lead to a tenfold decrease in the emission current and to the appearance of an additional low-energy peak (shifted by 0.5 eV from the main peak toward lower energies) in the field electron energy distribution. An increase in the anode voltage restored both the initial emission current and the electron energy distribution. *© 2002 MAIK "Nauka/Interperiodica".*

Introduction. The phenomenon of crystal lattice reconstruction in metal and semiconductor field emission cathodes as a result of thermal annealing in a strong electric field has been known for a long time and studied in sufficient detail. This effect was discovered by E. Müller during the study of a tungsten cathode in a field electron projector. The main evidence of the crystal reconstruction at the emitting point tip was a change in the field electron image observed on the projector screen. The change is manifested by variation in the image size and brightness, the crystal packing density, and the electron work function of the emitting crystal faces, which is accompanied by modification of the current–voltage characteristics. The initial equilibrium crystal lattice parameters, the field electron image, and the current–voltage characteristics could be restored by annealing the emitter in the absence of an electric field.

Recently [1], we reported on a spontaneous (approximately tenfold) drop in the field electron emission current from a carbon crystal, a decrease in the emission spot brightness, and a shift of the current–voltage characteristics to the lowest position in response to decrease in the anode voltage down to a certain threshold level. The initial emission parameters could be restored by annealing the emitting sample at 750°C. This behavior was explained by assuming that heating of the emitting carbon crystal in a strong electric field is accompanied by a spontaneous reconstruction of the sample. The purpose of this study was to verify this assumption and to investigate the effect of annealing in a strong electric field on the electron structure of a carbon crystal.

Experimental. A sample of the poly(acrylonitrile) (PAN) fiber crystal with a length of ~1 mm was glued with Aquadag onto a thin tantalum foil strip welded to a tungsten arc. After drying, the sample was treated in vacuum at a temperature of 750°C (measured with an optical pyrometer). The pretreated field emission cathode was introduced into a high-vacuum chamber of USU-4 type equipped with a field electron microscope (Müller projector) and an electrostatic dispersive electron energy analyzer. A secondary-electron multiplier detector at the analyzer output operated in the pulse count mode.

Upon introduction into the vacuum chamber, the emitter was "formed" under rough vacuum conditions by increasing the total electron emission current to ~150 μA. This treatment allowed the PAN crystals on the fiber surface to be separated as a result of the amorphous carbon particles being sputtered by the residual gas ions [2]. Then the sample was outgassed and cleaned by heating to 750°C under ultrahigh vacuum conditions (as is known, the surface of graphite-carbon materials is almost completely cleaned on heating to ~650°C [3]).

After the thermal treatment, a surface layer of the cathode was repeatedly stripped away by the emission current pulses (~130 μA) unless a field emission image appeared with a bright spot in the central part. Then the system was adjusted so as to provide that the spot would be probed by the energy analyzer aperture. The field electron energy distribution (FEED) was measured as described elsewhere [4]. The Fermi level position was determined with the aid of a reference tungsten emitter. The probe current–voltage (I–U) characteristics were constructed using the values of the anode voltage U_a and the corresponding electron currents measured by the energy analyzer.

Results and discussion. After removal of the cathode surface layer by emission pulses in ultrahigh vacuum, the FEED curves exhibited a single maximum of rather large width. The full width at half-maximum

1063-7850/02/2801-0001$22.00

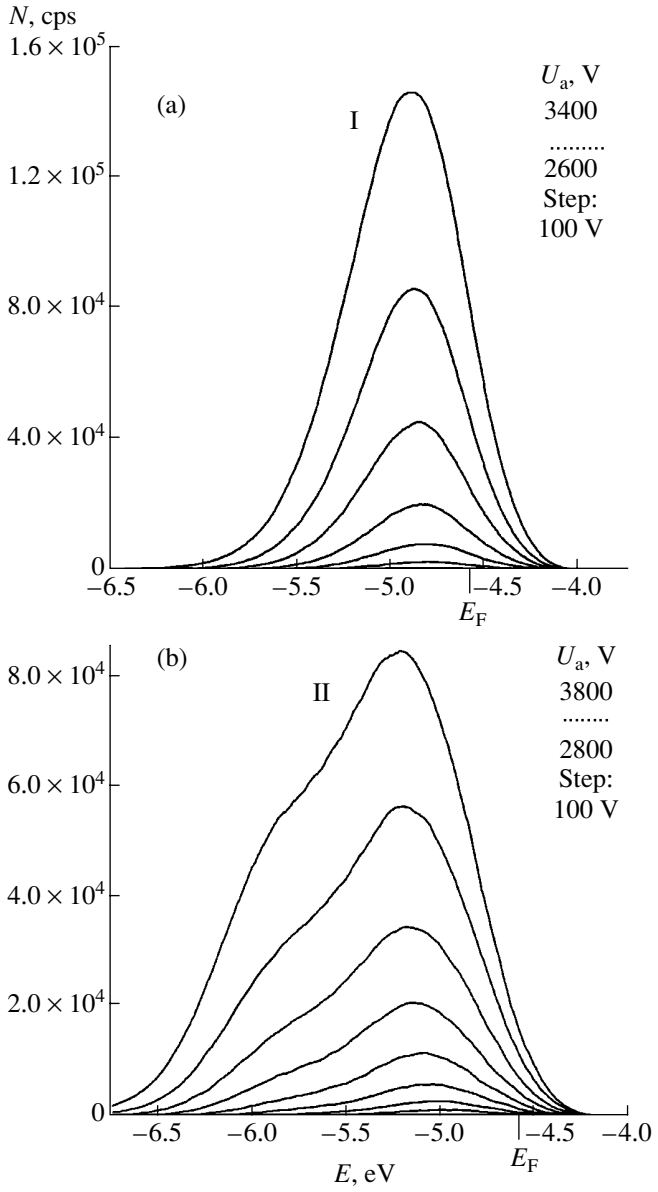

Fig. 1. A family of the field electron energy distributions for a carbon fiber crystal after annealing at 750°C (a) without the field (FEED I curves) and (b) in the field corresponding to the anode voltage of U_a = 3800 V (FEED II curves).

(FWHM) of the distributions increased from 0.55 to 0.7 eV with the anode voltage, while the corresponding *I–V* characteristic was virtually linear. A 15-min annealing of the sample at 750°C almost did not change the FEED shape, except for a small shift toward lower energies observed for the maximum U_a values (Fig. 1a, curve I) and a decrease in the probe current manifested by bending of the *I–U* characteristic (Fig. 2a, curve I).

Thus, the coincidence of the *I–U* curves (measured at low anode voltages) and the corresponding FEED profiles observed after stripping away the surface layer and the annealing at 750°C in ultrahigh vacuum showed that these treatments exposed a clean surface of the emitting crystal. The shift of the FEED curve toward lower energies was evidence of an increase in the voltage drop across the sample upon annealing.

The subsequent annealing of the emitter at the same temperature with an applied electric field (created by an anode voltage of 3800 V) led to a decrease in the probe current and the emission spot brightness. The FEED curves obtained by scanning in the interval of anode voltages from 2800 to 3800 V showed a significant increase in the FWHM value (from 0.6 to 1.25 eV) and revealed an additional low-energy maximum 0.45–0.5 eV below the main peak (Fig. 1b, curve II). Note that this position coincides with the position of a low-energy maximum in the FEED profiles observed as a result of a spontaneous reconstruction of the emitter crystal studied in [1]. The *I–U* characteristic corresponding to these FEED profiles (Fig. 2a, curve II) showed a more than tenfold decrease in the emission current, which also agrees well with a significant decrease in the emission current from the spontaneously reconstructed carbon crystal [1].

The FEED II profile measurements in the anode voltage interval from 2800 to 3800 V was accompanied by a shift toward lower energies. The presence of a linear portion in the plot of the main peak shift versus anode voltage (Fig. 2d, curve II) is indicative of the Zener effect manifestation. This is also evidence of a crystal structure of the probed region of a PAN fiber possessing a relatively small bandgap width [1].

An increase in the anode voltage up to 3900 V led to a sharp increase in the emission current and the emission spot brightness. Subsequent scanning of the FEED profiles showed that both the electron energy distribution and the *I–U* characteristic restored the initial shapes.

The procedure described above, including annealing of the emitter in the electric field at U_a = 3800 V, FEED measurements in the interval of U_a = 2800–3800 V, and the subsequent increase in U_a up to 3900 V (resulting in the spontaneous crystal reconstruction to the state featuring the initial characteristics) was multiply repeated. The resulting FEED profiles, *I–U* curves, and the displacement versus anode voltage plot depicted in Figs. 1 and 2 were well reproduced. While the probed spot brightness varied, the spot shape remained unchanged. The observed sequence of FEED transformations, manifested by the peak displacement and high-energy broadening in response to the anode voltage, increased from 2800 to 3900 V (Fig. 1, curve II), and the final spontaneous II ⟶ I reconstruction of the emitter from state II (corresponding to FEED profile II in Fig. 1 and *I–U* curve II in Fig. 2) to state I (corresponding to FEED profile I in Fig. 1 and *I–U* curve I in Fig. 2) completely coincided with the sequence of changes reported in [1] (also terminated by the spontaneous I ⟶ II reconstruction of the emitter crystal).

Thus, we concluded that the annealing of the emitter crystal in the electric field led to the same pattern of

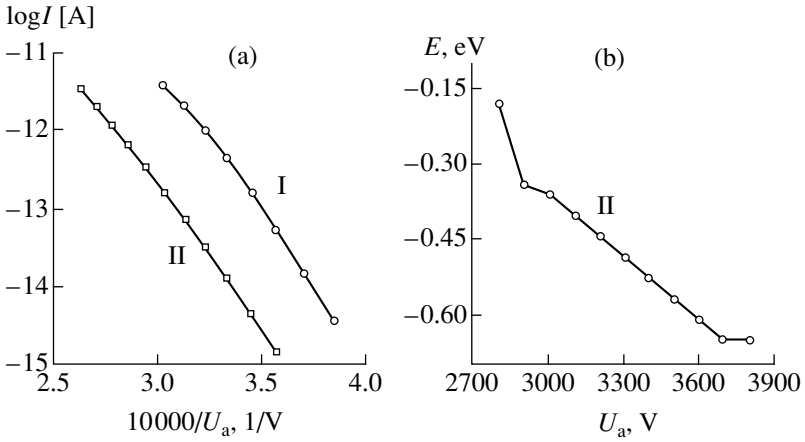

Fig. 2. (a) Probe current–voltage characteristics for a carbon fiber crystal after annealing at 750°C (I) without the field and (II) in the field corresponding to the anode voltage of U_a = 3800 V; (b) the plot of displacement of the main peak in FEED II versus anode voltage increased in the 2800–3800 V interval.

changes in the field electron energy distribution and the probe current–voltage characteristics as that observed for the spontaneous reconstruction reported in [1].

Conclusion. The results of this investigation confirm and complement the assumption concerning the spontaneous emitter crystal reconstruction as a result of heating in a strong electric field. Taking into account the data obtained previously [1], we can draw the following conclusions.

1. The spontaneous reconstruction of the emitter carbon crystal is determined by the ratio of the heating temperature and electric field strength. The process can proceed in both directions: from the state with normal FEED to that with an additional low-energy maximum and smaller emission current and vice versa, from the latter state to the initial state with a single FEED peak and a larger emission current.

2. The carbon crystal emitter reconstruction induced by the thermal and field treatment depends on the ratio of the annealing temperature and the electric field strength and is accompanied by a significant decrease in the emission current and the appearance of an additional low-energy maximum in the field electron energy distribution.

REFERENCES

1. V. M. Lobanov, Yu. M. Yumaguzin, and R. Z. Bakhtizin, Poverkhnost, No. 8, 53 (2000).
2. B. V. Bondarenko, A. Yu. Cherepanov, E. P. Sheshin, *et al.*, Radiotekh. Élektron. (Moscow) **30** (11), 2234 (1985).
3. *Chemistry and Physics of Carbon*, Ed. by Ph. Walker (Marcel Dekker, New York, 1965; Mir, Moscow, 1969).
4. R. Z. Bakhtizin, V. M. Lobanov, and Yu. M. Yumaguzin, Prib. Tekh. Éksp., No. 4, 247 (1987).

Translated by P. Pozdeev

Technical Physics Letters, Vol. 28, No. 1, 2002, pp. 10–12. Translated from Pis'ma v Zhurnal Tekhnicheskoĭ Fiziki, Vol. 28, No. 1, 2002, pp. 23–29.

The Effect of Illumination on the Characteristics of Acoustic Waves in a Piezoelectric Plate–Photoconducting Layer Structure

I. A. Borodina[a,*], I. E. Kuznetsova[a], B. D. Zaitsev[a], and S. G. Joshi[b]

[a] *Saratov Branch, Institute of Radio Engineering and Electronics, Russian Academy of Sciences, Saratov, Russia*
** e-mail: iren@ire.san.ru*
[b] *Marquette University, Milwaukee, WI 53201, USA*

Received March 11, 2001

Abstract—The effect of light on the characteristics of an acoustic wave with the transverse-horizontal polarization (SH_0) propagating in a piezoelectric plate–photoconducting layer structure was theoretically studied. Applied to the case of an *Y–X* cut lithium niobate (or *Y–X* potassium niobate) plate coated by a cadmium sulfide layer with the thicknesses h_1 and h_2, respectively, the results of this analysis show that the photosensitivity of such structures strongly depends on the h_1 and h_2 values, reaching a maximum for $h_1 = 0.1\lambda$ and $h_2 = 0.01\lambda$ (where λ is the acoustic wavelength). In the lithium niobate based structure with these parameters, the maximum value of the relative change in the wave velocity in response to the illumination intensity variation from 0.1 to 10^6 lx is 16% at a maximum damping rate of 5 dB/λ; the analogous values for potassium niobate are 47% and 17 dB/λ. These results show good prospects for the use of such a piezoelectric plate–photoconducting layer structures in photodetectors and optical radiation sensors. © *2002 MAIK "Nauka/Interperiodica".*

At present, considerable interest of researchers is drawn to the zero-order acoustic modes with the transverse-horizontal polarization (SH_0) propagating in thin (as compared to the acoustic wavelength) piezoelectric plates [1–3]. These waves are characterized by a significantly greater electromechanical coupling coefficient *K* as compared to that of the surface Rayleigh waves [4, 5]. For this reason, the use of SH_0 waves may considerably increase the efficiency of piezoelectric structures containing conducting layers sensitive with respect to external factors (light, electric and magnetic fields, etc.).

We have theoretically studied the effect of illumination on the velocity and damping of the SH_0 wave propagating in a piezoelectric plate (II)–photoconducting layer (III) structure (Fig. 1). The regions I ($x_3 < -h_1$) and IV ($x_3 > h_2$), where h_1 and h_2 are the thicknesses of the piezoelectric plate and the photosensitive layer, respectively, are assumed to be vacuum. We consider a two-dimensional problem whereby all values are assumed to be constant along the x_2 axis.

The wave propagating along the x_1 axis is described by a standard system of equations including the equation of motion (1), the Laplace equation (2) (or the Poisson equation (3)), material equations for the mechanical stress (4) and electric induction (5), the equation of charge conservation (6), and the equation describing the electric current with an allowance for the charge carrier diffusion (7):

$$\rho^{\mathrm{II,\,III}}\partial^2 U_{ij}^{\mathrm{II,\,III}}/\partial t^2 = \partial T_{ij}^{\mathrm{II,\,III}}/\partial x_j, \quad (1)$$

$$\partial D_j^{\mathrm{II}}/\partial x_j = 0, \quad (2)$$

$$\partial D_j^{\mathrm{III}}/\partial x_j = -\delta_v, \quad (3)$$

$$T_{ij}^{\mathrm{II,\,III}} = C_{ijkl}^{\mathrm{II,\,III}}\partial U_l^{\mathrm{II,\,III}}/\partial x_k + e_{kij}^{\mathrm{II,\,III}} - \partial\Phi^{\mathrm{II,\,III}}/\partial x_k, \quad (4)$$

$$D_j^{\mathrm{II,\,III}} = -\varepsilon_{jk}\partial\Phi^{\mathrm{II,\,III}}/\partial x_k + e_{jlk}^{\mathrm{II,\,III}}\partial U_l^{\mathrm{II,\,III}}/\partial x_k, \quad (5)$$

$$\partial J_r^{\mathrm{III}}/\partial x_r = -\partial\delta_v/\partial t, \quad (6)$$

$$J_r^{\mathrm{III}} = -\sigma_{rn}^{v}\partial\Phi^{\mathrm{III}}/\partial x_n + d_{rp}\partial\delta_v/\partial x_p. \quad (7)$$

Here, ρ is the density of medium; U_i is the *i*th component of the mechanical displacement of particles; T_{ij} is the mechanical stress tensor; Φ is the electric poten-

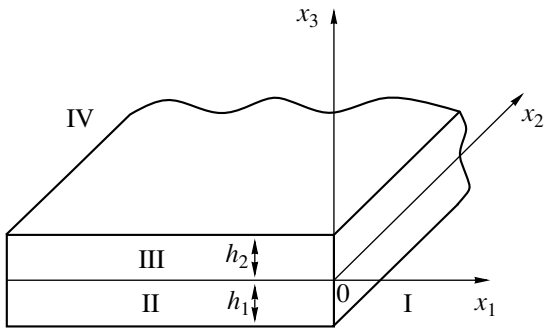

Fig. 1. A Schematic diagram of the structure studied: (I, IV) vacuum; (II) piezoelectric plate with the thickness h_1; (III) photoconducting layer with the thickness h_2.

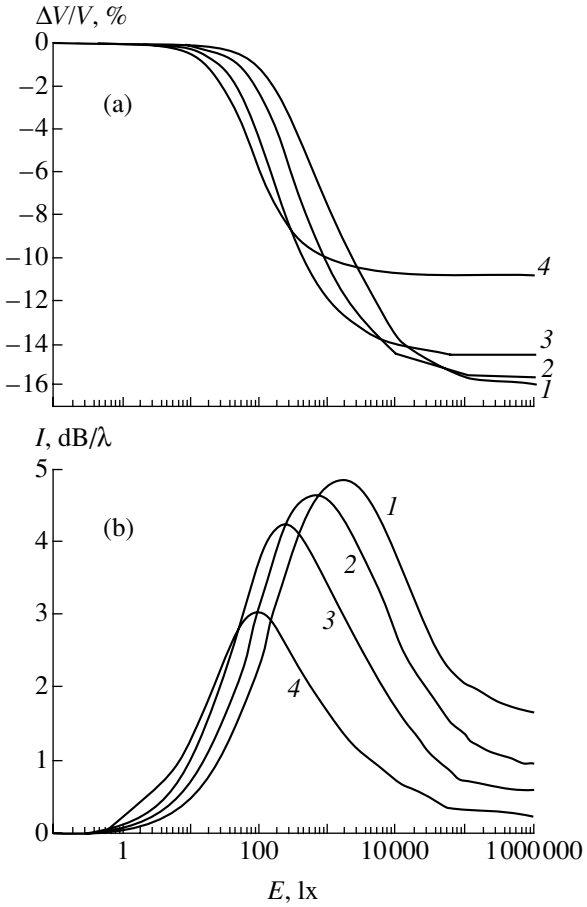

Fig. 2. Plots of (a) the relative change $\Delta V/V$ in the acoustic wave velocity and (b) the wave damping I versus illumination E for the SH_0 wave propagating in a $LiNbO_3$–CdS structure with the fixed piezoelectric ($LiNbO_3$) layer thickness $h_1 = 0.1\lambda$ and various photosensitive (CdS) layer thicknesses $h_2 = 0.01\lambda$ (*1*), 0.03λ (*2*), 0.05λ (*3*), and 0.1λ (*4*).

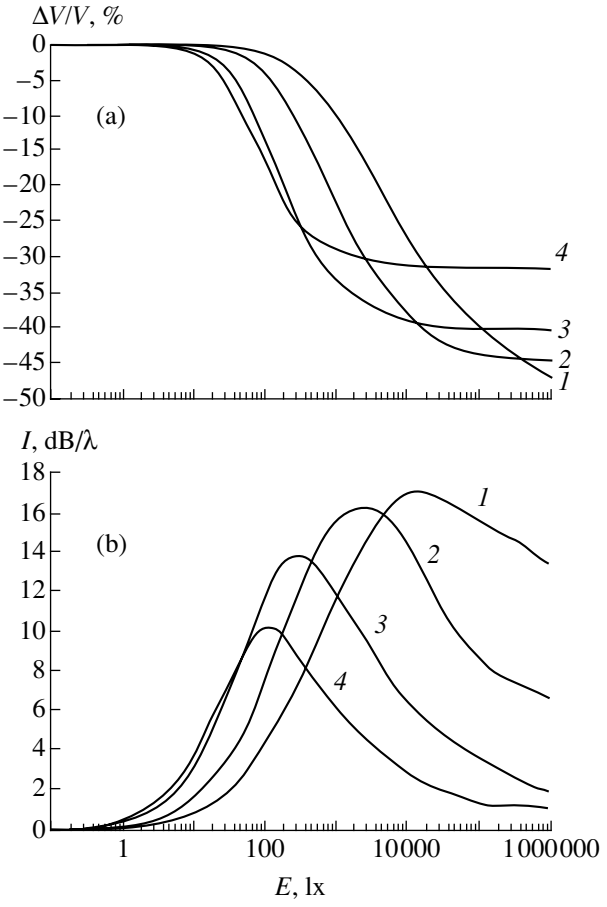

Fig. 3. Plots of (a) the relative change $\Delta V/V$ in the acoustic wave velocity and (b) the wave damping I versus illumination E for the SH_0 wave propagating in a $KNbO_3$–CdS structure with the fixed piezoelectric ($KNbO_3$) layer thickness $h_1 = 0.1\lambda$ and various photosensitive (CdS) layer thicknesses $h_2 = 0.01\lambda$ (*1*), 0.02λ (*2*), 0.05λ (*3*), and 0.1λ (*4*).

tial; C_{ijkl}, e_{ijk}, and ε_{jk} are the elastic, piezoelectric, and dielectric constants, respectively; D_j is the jth component of the electric induction vector; t is time; δ_v is the volume charge density; J_r^{III} is the conduction current in region III; σ_{rn}^v is the bulk conductivity; and d_{rp} is the diffusion coefficient.

In regions I and IV (vacuum), the electric potential satisfies the Laplace equation

$$\partial D_j^{I, IV}/\partial x_j = 0. \tag{8}$$

The system of Eqs. (1)–(8) was solved together with the standard mechanical boundary conditions

$$\begin{aligned} &U_i^{II} = U_i^{III}, \quad T_{3j}^{II} = T_{3j}^{III}, \quad x_3 = 0; \\ &T_{3j}^{II} = 0, \quad x_3 = -h_1; \quad T_{3j}^{III} = 0, \quad x_3 = h_2; \end{aligned} \tag{9}$$

and electrical boundary conditions

$$\begin{aligned} &\Phi^{I} = \Phi^{II}, \quad D_j^{I} = D_j^{II}, \quad x_3 = -h_1; \\ &\Phi^{II} = \Phi^{III}, \quad D_j^{II} = D_j^{III}, \quad x_3 = 0; \end{aligned} \tag{10}$$

$$\Phi^{III} = \Phi^{IV}, \quad D_j^{III} = D_j^{IV}, \quad x_3 = h_2; \tag{11}$$

$$J_3^{III} = 0, \quad x_3 = 0, \quad x_3 = h_2. \tag{12}$$

The problem (1)–(12) was solved by the well-known numerical method [6].

A solution was obtained for a piezoelectric plate of *Y–X* cut lithium niobate $LiNbO_3$ (or *Y–X* potassium niobate $KNbO_3$) characterized by a high electromechanical coupling coefficient K for the SH_0 mode [5, 7]. The photoconducting material was single crystal cadmium sulfide (*Z* cut CdS).

First, we analyzed the effect of the bulk conductivity of CdS on the relative change in the SH_0 wave velocity and on the wave damping for various values of layer

thicknesses h_1 and h_2. Then, a relationship between changes in the wave velocity and damping, on the one hand, and the illumination level, on the other hand, was established with an allowance for the known dependence of the bulk conductivity on the illumination [8].

Figure 2 shows the plots of the relative change in the wave velocity ($\Delta V/V$) and damping I of the SH_0 wave on the illumination E for a $LiNbO_3$–CdS structure with the fixed piezoelectric layer thickness h_1 and various photosensitive layer thicknesses h_2. Figure 3 shows the analogous data for a $KNbO_3$–CdS structure. As can be seen from Figs. 2 and 3, the maximum value of the relative change in the wave velocity in response to the illumination intensity variation from 0.1 to 10^6 lx for the $LiNbO_3$ based structure is 16% at a maximum damping rate of 5 dB/λ (for $h_1 = 0.1\lambda$ and $h_2 = 0.01\lambda$); the analogous maximum values for $KNbO_3$ are 47% and 17 dB/λ.

In addition, the analysis showed that a change in the diffusion coefficient (within at least two orders of magnitude) virtually does not affect the SH_0 wave characteristics in the structures studied. This implies that the results are applicable both to CdS single crystals and to the structures involving CdS films.

On the whole, the obtained results demonstrated high photosensitivity of the two-layer piezoelectric-photoconductor structures studied and can be used for the development of effective photodetectors and optical radiation sensors.

Acknowledgments. This study was supported by the Russian Foundation for Basic Research (project no. 01-02-16266) and by a grant from the National Science Foundation (USA).

REFERENCES

1. S. W. Wenzel and R. M. White, IEEE Trans. Electron Devices **35** (6), 735 (1988).
2. M. J. Vellekoop, Ultrasonics **36** (1-5), 7 (1998).
3. D. S. Ballantine, R. M. White, S. J. Martin, A. J. Ricco, E. T. Zellers, G. C. Frye, and H. Wohltjen, *Acoustic Wave Sensors* (Academic, San Diego, 1997), Ch. 3.
4. S. G. Joshi and Y. Jin, IEEE Trans. Ultrason., Ferroelectr. Freq. Control **43** (3), 491 (1996).
5. B. D. Zaitsev, S. G. Joshi, and I. E. Kuznetsova, IEEE Ultrason., Ferroelectr. Freq. Control **46** (5), 1298 (1999).
6. M. K. Balakirev and I. A. Gilinskii, *Waves in Piezocrystals* (Nauka, Novosibirsk, 1982).
7. I. E. Kuznetsova, B. D. Zaitsev, S. G. Joshi, and I. A. Borodina, Electron. Lett. **34** (23), 2280 (1998).
8. A. O. Olesk, *Photoresistors* (Énergiya, Moscow, 1966).
9. Yu. V. Gulyaev, I. E. Kuznetsova, B. D. Zaitsev, *et al.*, Pis'ma Zh. Tekh. Fiz. **25** (8), 21 (1999) [Tech. Phys. Lett. **25**, 302 (1999)].

Translated by P. Pozdeev

Technical Physics Letters, Vol. 28, No. 1, 2002, pp. 13–14. Translated from Pis'ma v Zhurnal Tekhnicheskoĭ Fiziki, Vol. 28, No. 1, 2002, pp. 30–33.

The Effect of Irradiation with Fast Argon Ions on the Characteristics of Planar Silicon Heterostructures

S. S. Karatetskiĭ, O. P. Korovin, and V. I. Sokolov

Ioffe Physicotechnical Institute, Russian Academy of Sciences, St. Petersburg, 194021 Russia

Received April 19, 2001; in final form, August 20, 2001

Abstract—Irradiation of a silicon-based planar heterostructure with 40-MeV argon ions leads to a decrease in the MOS structure capacitance and in the *p–n* junction photosensitivity range. The effects are explained by special features of the damage produced by fast ions in the crystal target. © *2002 MAIK "Nauka/Interperiodica".*

Irradiation with fast ions significantly modifies the physical properties of various materials. These changes are related to the process of fast ion stopping, which produces damage in the irradiated material structure and leads to a partial decomposition of chemical compounds in a local region near the particle track [1]. We have experimentally studied the effect of irradiation with 40-MeV argon ions on the properties of planar heterostructure in order to determine the possibility of using this treatment for controlled modification of the material parameters.

The samples were made of (100)-oriented *n*-type silicon single crystal wafers with a resistivity of 20 Ω cm. The metal–oxide–semiconductor (MOS) capacitors with a metal electrode area of 1 mm^2 were prepared by depositing aluminum onto a 100-nm-thick thermal oxide layer grown by exposure to dry oxygen at 1050°C. The diode structures were obtained by local boron diffusion in a 25 mm^2 window to a depth of 1.5 μm. The heterostructures were irradiated with 40-MeV argon ions (stopping range, 2 mg/cm^2) to a total dose of 5×10^{11} or 5×10^{12} cm^{-2}. Before and after the irradiation, the samples were characterized be measuring the capacitance–voltage characteristics of MOS capacitors, current–voltage curves, and spectral characteristics of the diodes.

It was found that the total argon ion dose plays a determining role in modification of the observed characteristics. At a dose of 5×10^{11} cm^{-2}, which corresponds to the single ion damaging a local area of 200 nm^2, the parameters of the irradiated planar structures exhibited virtually no changes. When the dose increased to 5×10^{12} cm^{-2}, the irradiated MOS capacitors showed a decrease in capacitance measured in the enrichment regime and some increase in this parameter measured in the inversion regime (Fig. 1). These changes are apparently caused by a partial compensation or inversion in the subsurface region of *n*-type silicon related to the radiation-induced defects. It is interesting to note that, although the absorbed dose is on the order of 10^8 Gy, no increase in the concentration of surface states was detected in the samples irradiated by fast argon ions, in contrast to changes observed in the analogous MOS structures irradiated with neutrons or gamma quanta to a much lower dose on the order of 10^3 Gy [3].

The ion irradiation resulted in some increase in the reverse diode current and a fivefold growth in the photoinduced current. These changes are apparently also cased by radiation defects introduced into the subsurface region, which create deep levels in the forbidden band of the semiconductor and lead to a decrease in the charge carrier lifetime.

As is well known, the appearance of radiation defects in semiconductors expands the range of photo-

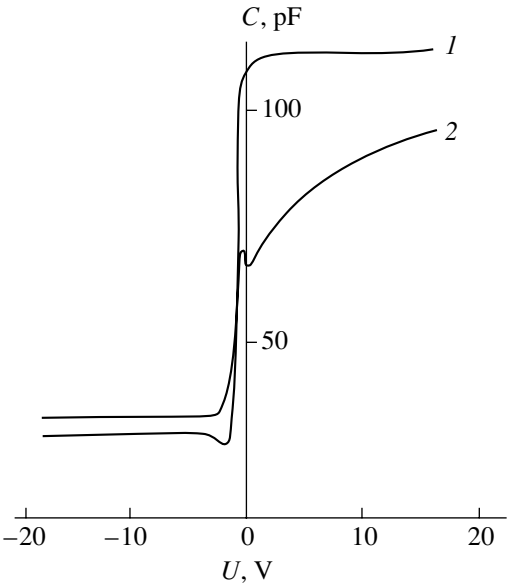

Fig. 1. Capacitance–voltage characteristics of MOS structures (*1*) before and (*2*) after irradiation with fast argon ions.

1063-7850/02/2801-0013$22.00 © 2002 MAIK "Nauka/Interperiodica"

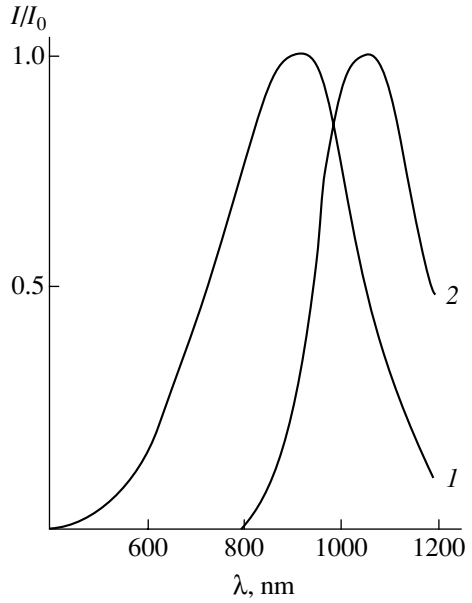

Fig. 2. The relative photoresponse spectrum of a planar silicon diode (*1*) before and (*2*) after irradiation with fast argon ions.

sensitivity and shifts the photoresponse curve toward longer wavelengths. The irradiation with fast argon atoms also shifted the photosensitivity maximum toward longer wavelengths (Fig. 2), but the range of photosensitivity significantly narrowed. We believe that this may be related to sharp changes in the semiconductor structure and parameters at the end of the ion stopping range caused by the possible formation of melted zones and their subsequent recrystallization.

REFERENCES

1. J. Jensen, A. Dunlop, and S. Della-Negra, Nucl. Instrum. Methods Phys. Res. B **146** (1-4), 399 (1998).
2. S. Kaschieva and A. Djakov, Radiat. Eff. Express **1**, 115 (1987).
3. H. F. Matare, *Defect Electronics in Semiconductors* (Wiley, New York, 1971; Mir, Moscow, 1974).

Translated by P. Pozdeev

Technical Physics Letters, Vol. 28, No. 1, 2002, pp. 15–16. Translated from Pis'ma v Zhurnal Tekhnicheskoĭ Fiziki, Vol. 28, No. 1, 2002, pp. 34–38.

Photovoltaic X-ray Detectors Based on Epitaxial GaAs Structures

R. A. Achmadullin, V. F. Dvoryankin, G. G. Dvoryankina, Yu. M. Dikaev, M. G. Ermakov, O. N. Ermakova, A. I. Krikunov, A. A. Kudryashov, A. G. Petrov, and A. A. Telegin

Fryazino Branch, Institute of Radio Engineering and Electronics, Russian Academy of Sciences, Fryazino, Moscow oblast, Russia

e-mail: vfd217@ire216.msk.su

Received August 14, 2001

Abstract—A new type of the photovoltaic X-ray detector based on epitaxial p^+–n–n'–n^+ GaAs structures is proposed, which provides for a high efficiency of charge carrier collection in a nonbiased operation regime at room temperature. The GaAs structures were grown by vapor phase epitaxy on heavily doped n^+-GaAs substrates. The X-ray sensitivity range covers the effective energies from 8 to 120 keV. The maximum output signal in the short-circuit regime is 30 μA min/(Gy cm^2). The detector response to γ-radiation from a ^{137}Cs [660 keV] radioactive isotope was measured. © *2002 MAIK "Nauka/Interperiodica".*

In the X-ray detectors based on *p*–*i*–*n* structures and Schottky barrier diodes, a high efficiency in the charge carrier collection is reached at the expense of using high reverse bias voltages [1]. For example, GaAs detectors of these types require a 1–2 V/μm bias, which results in room-temperature leak current densities as high as 10–30 nA/mm^2 [2, 3]. An advantage of the photovoltaic semiconductor detectors, which are capable of operating in a nonbiased regime, is an extremely small level of leaks.

We have developed a new photovoltaic X-ray detector based on the epitaxial GaAs structures [4], which ensure a high efficiency of charge carrier collection in a nonbiased operation regime at room temperature.

The required epitaxial p^+–n–n'–n^+ GaAs structures were grown by vapor phase epitaxy (VPE) on heavily doped 400-μm-thick n^+-GaAs substrates. The structure comprises three epitaxial layers: the upper layer with a thickness of 1–2 μm, the intermediate active lightly doped 80–100 μm-thick *n*-GaAs layer, and the lower buffer *n*'-GaAs layer with a thickness of 2–5 μm and $n' = 5 \times 10^{17}$ cm^{-3}. The heterostructure was completed by depositing ohmic contacts above the upper layer and onto the rear side of the substrate.

The thickness of a depleted region in the epitaxial *n*-GaAs layer was determined by measuring the capacitance–voltage (*C*–*U*) characteristics of the diode structures. By these data, the structures with a depleted region thickness close to the active epitaxial layer thickness were selected. The built-in electric field configuration in the depleted region was optimized by changing the donor impurity concentration in the *n*-GaAs layer. A criterion of the optimum field configuration was the maximum efficiency of charge carrier collection, which was determined using radiation from an ^{241}Am [60 keV] isotope measured in a nonbiased regime and with a reverse bias of 17 V. For the selected structures, the charge collection efficiency in these regimes was 93.4 and 93.6%, respectively.

For the X-ray photon energies below 120 keV, the process of the radiation absorption in GaAs is determined by the photoelectric effect. According to this, the absorbed photon energy is converted into the kinetic energy of photoelectrons and Auger electrons. The kinetic energies of photoelectrons are determined by the difference between the primary photon energy and the electron binding energies in Ga and As atoms. Since the photoelectric effect involves only the bound electrons, a cross section for this effect is maximum for the *K*-shells of Ga and As atoms.

The electron binding energies on these shells are 10.371 and 11.871 keV, respectively [5]. Thus, for photon energies above 12 keV, the photoelectrons excited as a result of the photoelectric effect may possess a significant kinetic energy. Moving in the depleted region, the high-energy electrons loose the energy for ionization and generate a large number of secondary (low-energy) electrons that can take part in the electron–hole pair production. The energy necessary for a single electron–hole pair production in GaAs is 4.2 eV.

The energies of Auger electrons generated in the *KLL* Auger transitions in Ga and As amount to 7.705–8.027 and 8.742–9.654 keV, respectively [6]. These Auger electrons also contribute to the electron–hole pair production. Thus, the internal photoelectric quantum yield in X-ray irradiated GaAs is sufficiently large. The photocurrent generated in the X-ray detector in the short-circuit regime depends on the quantum yield and

1063-7850/02/2801-0015$22.00

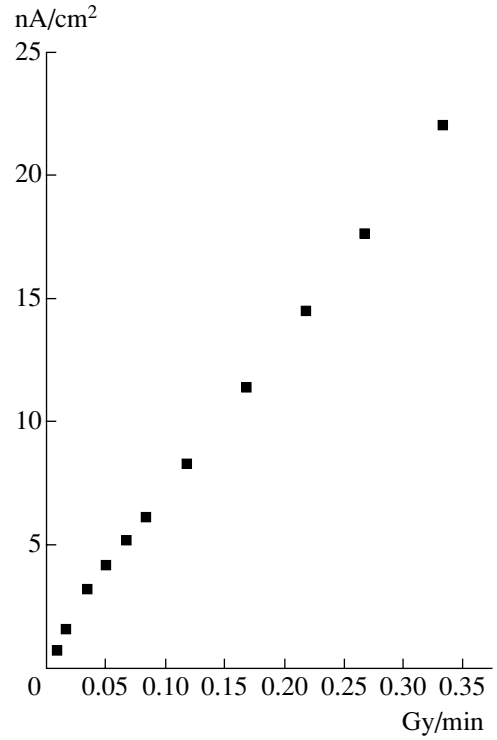

The experimental plot of output photocurrent density versus dose power measured using γ-radiation from a ^{137}Cs [660 keV] radioactive isotope.

can be expressed as $i = \eta q N_q$, where η is the total quantum yield, q is the electron charge, and N_q is the number of primary X-ray photons incident onto the detector surface.

The sensitivity range of the epitaxial GaAs photovoltaic X-ray detector, measured using the bremsstrahlung radiation from an X-ray tube with a tungsten anode, covers the effective energies from 8 to 120 keV. A maximum response of the detector operating in the short-circuit regime, normalized to the surface dose power, was observed at an energy of 35 keV and amounted to 30 μA min/(Gy cm^2). At a fixed energy, the photoresponse is a linear function of the dose power. Above 35 keV, the detector sensitivity decreases but at a lower rate as compared to the decrease in the X-ray absorption coefficient in GaAs [7]. This is probably explained by the high efficiency of the conversion of X-ray photons into charge in the epitaxial GaAs structures employed.

The detector was also tested for sensitivity with respect to γ-radiation. An experimental plot of the output signal versus dose power measured using a ^{137}Cs [660 keV] radioactive isotope is presented in the figure. As can be seen, the output photocurrent exhibits a break at a dose power of 0.03 Gy/min. For a primary photon energy of 660 keV, the detector operates in the regime of a solid-state ionization chamber. The γ-photons are absorbed in GaAs by the inelastic Compton scattering mechanism, which is accompanied by the production of a recoil electron and a secondary X-ray photon. The energy of the recoil electrons was approximately estimated at 237 keV, which corresponds to an electron mean free path of about 100 μm in GaAs [8].

Thus, we have created a photovoltaic X-ray detector based on epitaxial GaAs structures, which can be employed, for example, in low-dose X-ray equipment for medicine.

REFERENCES

1. W. Bencivelli, R. Bertini, E. Bertolucci, *et al.*, Nucl. Instrum. Methods Phys. Res. A **338**, 549 (1994).
2. C. M. Buttar, Nucl. Instrum. Methods Phys. Res. A **395**, 1 (1997).
3. R. L. Butes, S. M. Manolopoulos, K. Mathieson, *et al.*, Nucl. Instrum. Methods Phys. Res. A **434**, 1 (1999).
4. R. A. Achmadullin, V. F. Dvoryankin, M. G. Ermakov, *et al.*, in *Proceedings of the 5th International Conference "Applications of Semiconductor Detectors in Nuclear Physics Problems," Riga, Latvia, 1998*, p. 84.
5. T. A. Carlson, *Photoelectron and Auger Spectroscopy* (Plenum, New York, 1975; Mashinostroenie, Leningrad, 1980).
6. F. P. Larkins, J. Phys. B **8**, 47 (1976).
7. E. Storm and H. Israel, *Photon Cross Sections—from 0.001 to 100 MeV for Elements 1 through 100* (Los Alamos Scientific Laboratory, New Mexico, 1967; Atomizdat, Moscow, 1973).
8. J. A. Gledhill, J. Phys. A **6**, 1420 (1973).

Translated by P. Pozdeev

Technical Physics Letters, Vol. 28, No. 1, 2002, pp. 17–20. Translated from Pis'ma v Zhurnal Tekhnicheskoĭ Fiziki, Vol. 28, No. 1, 2002, pp. 39–48.

Nanoscale Ion Beam Polishing of Optical Materials

A. I. Stognij, N. N. Novitskii, and O. M. Stukalov

Institute of Solid State and Semiconductor Physics, National Academy of Sciences of Belarus, Minsk, Belarus

e-mail: stognij@ifttp.bas-net.by

Received June 9, 2001; in final form, August 27, 2001

Abstract—A method of ion beam polishing is described, the special features of which consist in (i) preferential ion beam assisted deposition of a nanometer-thick layer into depressions of the initial relief by oxygen-ion sputtering of a target with a composition identical to that of the processed object; (ii) sputtering of the resulting surface structure by a normally incident low-energy oxygen ion beam to a depth reaching approximately two layers of the deposited material; and (iii) deposition–sputtering cycles repeated with gradually decreasing thickness of the deposited layer until the necessary final state of the surface is attained. Examples of the surface of quartz, sitall (glass ceramic), and BK-7 optical glass processed using the proposed ion beam polishing method show a more than twofold decrease in the height of the relief protrusions as compared to that on the initial surface. On the ion beam processed quartz surface areas with dimensions 2.5×2.5 μm, the maximum roughness height did not exceed 0.8 nm. *© 2002 MAIK "Nauka/Interperiodica".*

Introduction. The phenomenon of preferential sputtering of the relief protrusions (hills) against depressions (valleys) on the surface irradiated by obliquely incident keV-energy ion beams is successfully employed for the surface relief planarization over small areas containing roughnesses on both a microscopic [1] and atomic scale [2]. However, the present-day problems posed by the development of nanoelectronics and microwave optics (including high-power applications) require that the surface finish of some materials, such as quartz, sitall (devitrified silicon glass ceramic of the Pyroceram type), and BK-7 optical glass, would reach a level of nanometer or even subnanometer roughness, with processed surface areas up to 10–100 cm^2. In addition, it is necessary to minimize radiation damage in the processed material, which implies that the ion beam energies should be reduced to an acceptable level. However, the obtaining of ion beams with a current density exceeding 0.1 mA/cm^2 and an energy of several hundred electronvolts, capable of uniformly processing a large surface area at a glancing angle, is presently a difficult technological problem [3].

In connection with the problems outlined above, it should be noted that it is possible to provide for the surface planarization on a submicron level using normally incident ion beams [4, 5]. Prior to sputtering, Johnson *et al.* [4] leveled the initial surface relief by depositing a thick layer of a material characterized by a sputtering yield equal to that of the sample. In our recent study [5], the planarization effect was achieved due to preferential redeposition of the sputtered material into valleys of the initial surface relief in the course of prolonged irradiation of the sample with a low-energy oxygen ion beam. Using an oxygen ion beam and conducting the process in an oxygen atmosphere allowed the level of foreign impurities to be significantly reduced even for the process carried out under technical vacuum conditions (residual pressures from 10^{-2} to 10^{-3} Pa).

It is also necessary to mention the recent review [6], which treats in much detail evolution of the surface relief in the course of ion beam sputtering for a large variety of materials, with special emphasis on the effects of surface planarization. It was pointed out that the problem of nanoscale and subnanoscale surface polishing over the areas of 10–100 cm^2, together with the task of minimizing the risk of damaged surface and subsurface layer formation, are still of urgent importance. For example, Koslowski *et al.* [7] reported on successful nanoscale polishing of a diamond surface over a 3×3 mm surface area (only provided by a combination of mechanochemical polishing, ion beam sputtering, and plasma etching techniques) and analyzed the drawbacks hindering realization of the nanoscale surface finish by the conventional mechanochemical methods and those based on the ion, reactive ion beam, ion beam, and ion–plasma etching techniques, as well as the methods using pulsed IR and UV lasers, etc.

This study, performed in developing previous ideas and results [4, 5], showed the possibility of polishing the surface of the aforementioned materials to a level of nanometer and even subnanometer roughness by a method based on the following processes: (i) preferential ion beam assisted deposition of a nanometer-thick layer (with a thickness equal to about half of the characteristic roughness height) into valleys of the initial relief by oxygen ion beam sputtering of a target with a composition identical to that of the processed object; (ii) sputtering of the resulting surface structure by a normally incident low-energy oxygen ion beam to a depth reaching approximately two layers of the previ-

1063-7850/02/2801-0017$22.00

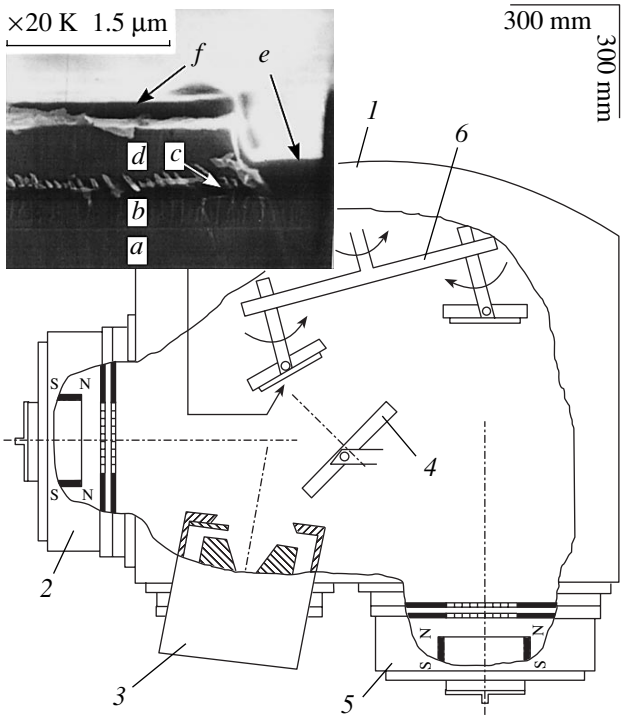

Fig. 1. A schematic diagram of the ion beam polishing setup: (*1*) vacuum chamber; (*2*) ion source; (*3*) open-edge ion source; (*4*) target; (*5*) ion source; (*6*) substrate holder. The inset shows a SEM micrograph of the transverse cleavage of a test ridge–groove structure: (*a*) silicon substrate; (*b*) thermal silicon dioxide layer; (*c*) adhesive underlayer; (*d*) aluminum layer; (*e*) SiO_x layer on the groove bottom; (*f*) SiO_x layer on the ridge top.

ously deposited material; and (iii) repeated deposition–sputtering cycles with gradually decreasing thickness of the deposited layer until attainment of the state of the surface with approximately equal roughness height before and after the deposition–sputtering cycle.

Experimental. Figure 1 shows a schematic diagram of the ion beam polishing setup. The main parts are a vacuum chamber *1*, a thin layer deposition unit (analogous to that described in [8]) with a wide-aperture oxygen ion source *2*, low-energy Kaufman open-edge ion source *3* of the Hall type, and a target *4* (oriented at an angle of 45° relative to the axis of the ion source *2*). Another wide-aperture oxygen ion source *5* (with a design analogous to that described in [9]) is used to sputter the targets with an area of up to 100 cm^2 mounted in a mobile substrate holder *6*. Chamber *1* is evacuated with an oil diffusion pump to a residual pressure not exceeding 10^{-3} Pa. The working pressure after the admission of oxygen via ion sources *2* and *5* (with a total gas flow rate of up to 8 cm^3/min) and argon via ion source *3* (up to 2 cm^3/min) does not exceed 4×10^{-2} Pa. The initial, intermediate, and final states of the sample surface were monitored, and the sputtering and deposition rates were determined with the aid of a Hitachi S-806 scanning electron microscope (SEM) and a Femtoskan-001 atomic-force microscope (AFM) (Advanced Technology Center, Moscow State University) with a 2.5×2.5 μm scanned field area. The AFM was operated in a contact regime using silicon cantilevers (MicroMash, www.spmtips.com, Estonia).

The rate of deposition of a nanometer-thick layer was estimated using a calibration plot of the layer thickness versus deposition time constructed for the same material deposited onto a silicon substrate during 20, 30, 40, and 50 min and interpolated to shorter times. The deposited layers were sputtered by an oxygen ion beam with a current density of 0.12 mA/cm^2 produced by the ion source *5* operating at an ion extraction voltage of 300 V. The sputtering rate was estimated using a calibration plot of the sputtered layer thickness change versus sputtering time constructed for the same material sputtered during 10, 15, 20, and 25 min. This average estimated sputtering rate was 1.4 nm/min (to within a 30% accuracy for the cases considered below). The average rates of deposition of the products sputtered from the quartz, sitall, and optical glass (BK-7) targets was maintained at a level below 2 nm/min (i.e., several times smaller than in [8]), which was possible owing to a decrease in the output parameters of ion sources *2* and *3*.

The sample surface was oriented at 30° with respect to the targets and at 50° relative to the assisting ion beam source *3*. The average current density of the assisting ion beam was 0.6 mA/cm^2 at an average ion energy below 50 eV, which (together with the indicated sample surface orientation) provided for the main condition of realization of the proposed polishing method: the rate of filling of the relief valleys must be 1.4–1.8 times that of the rate of deposition onto the relief hills. The latter is illustrated by the inset in Fig. 1, which shows the result of deposition of a material sputtered from a quartz target onto a test structure containing a rectangular groove with 0.5×0.5 μm cross section. As can be seen, the ratio of the deposited SiO_x layer thicknesses on the groove bottom and on the ridge top is about 1.8; note also that the side walls of the groove are only partly coated with the sputtered material deposited at the bottom ($x \approx 2.1$ [8]). In order to increase reliability of the SEM micrograph, the test sample was prepared with a relatively thick SiO_x layer. The results of our preliminary experiments agree with the commonly accepted opinion that deposition under the ion beam assisted conditions eliminates differences between the properties of an optical material in the deposited films and in the bulk form (see, e.g., [8, 10]).

Results and discussion. Smoothening of the surface relief of the initial material as a result of deposition of a thin layer with close composition and properties decreases selectivity of the subsequent ion sputtering process with respect to hills and valleys present in the initial surface. In addition, the deposited and gradually sputtered layer produces partial screening of the sam-

ple, thus reducing the level of the radiation damage. The results of simulation of the ion sputtering process using the well-known SRIM-2000 program [6] and the elementary geometric analysis based on the proposed polishing scheme indicate that the optimum polishing conditions are realized when the thickness of the preliminarily deposited layer does not exceed half of the characteristic roughness height in the initial surface, and the resulting surface structure is sputtered to a depth equal to about two layers of the deposited material. The sputtering should be performed with oxygen ions possessing an energy such that the ion range in the initial target material does not exceed one deposited layer thickness. The latter requirement agrees with the experimental conditions studied.

Figure 2 shows a series of SEM micrographs and AFM images of a quartz sample, which clearly illustrate evolution of the sample surface in the course of the ion beam polishing according to the proposed method. The initial quartz surface was thoroughly polished by a mechanochemical technique. No relief features on the initial surface could be revealed by SEM micrographs taken at a magnification of ×20000. However, the SEM micrographs taken with a magnification of ×50000 (Fig. 2a) and the AFM images (Fig. 2d) reveal separate elongated protrusions with a characteristic length below 100 nm and a height below 4 nm, as well as a number of roughnesses with smaller area and lower height on a generally flat background. Deposition of a layer with a thickness below 3 nm onto the initial sample surface by means of sputtering of a quartz target makes the coarse protrusions less pronounced on the common flat background: these features acquire a more regular rounded shape with a characteristic length reduced to 60 nm (Fig. 2b). The subsequent sputtering of this surface structure to a preset depth of 6 nm, followed by sputter deposition of 3- and 1.5-nm-thick layers and sputter removal of 6- and 3-mm-thick layers, yielded a surface in which even the SEM micrographs with a magnification of ×50000 reveal no relief features (Fig. 2c), while the AFM images (Fig. 2e) display only separate sharp cusps less than 0.8 nm in height relative to the relief bottom level along a 1-μm-long line drawn along the most inhomogeneous surface region with dimensions 2.5×2.5 μm.

The initial sitall samples obtained after a preliminary mechanochemical treatment had a surface quality inferior to that of the primary quarts samples (Fig 3a). In this pattern we may conventionally distinguish between surface inhomogeneities of three types: (i) rare elongated islands with a length of up to 100 nm and a height of up to 11 nm; (ii) coarse domains with smooth boundaries and a height of up to 9 nm, occupying almost the whole surface; and (iii) small cone-shaped protrusions with a height of up to 5 nm situated between the above domains. In this case, deposition of an approximately 5-nm-thick layer by sputtering a sitall target leads to smoothening of the initial surface relief and decreases the maximum roughness height to 7 nm

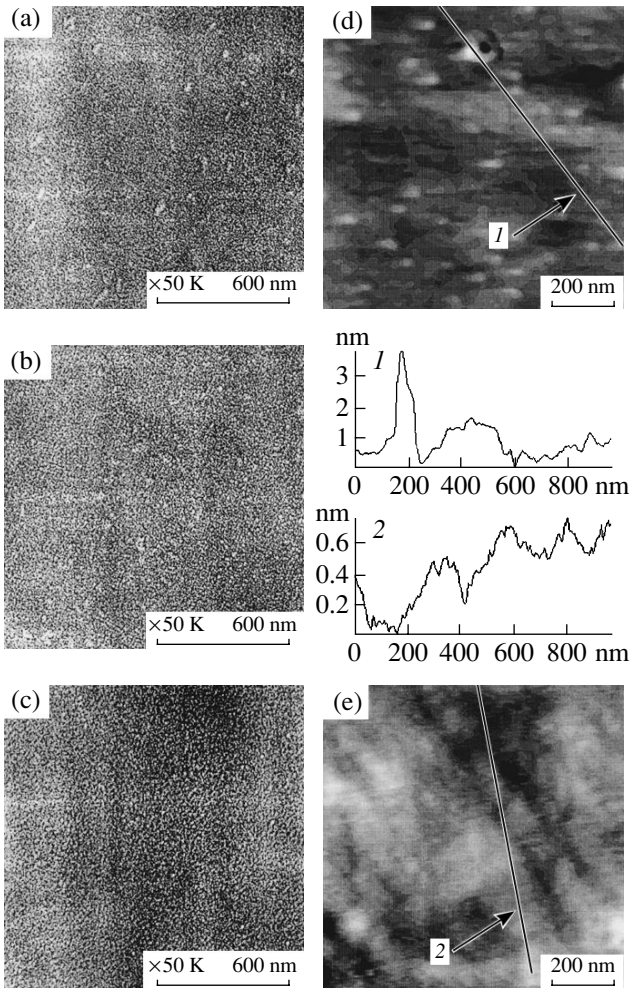

Fig. 2. Quartz surface evolution in the course of ion beam polishing: (a, b, c) SEM micrographs of the initial, SiO_x-coated (~3 nm), and final sample surface, respectively; (d, e) AFM images of the initial and final surface, respectively, and (*1*, *2*) the corresponding relief cross section profiles along the indicated lines.

(Fig. 3b). After sputtering of this surface structure to a depth of approximately 12 nm, followed by double sputter deposition of 3-nm-thick layers and sputter removal of 6-nm-thick layers, the sample surface reached the final state (Fig. 3c), still displaying separate protrusions with a maximum height of up to 5 nm relative to the relief bottom level along 1-μm-long lines. The proposed polishing procedure did not allow these inhomogeneities to be eliminated. However, these surface features are probably related to the sitall manufacturing technology rather than to the surface processing.

BK-7 optical glass offers an example of more plastic and chemically active material as compared to quartz and sitall. For this reason, the BK-7 samples were polished using a more complicated scheme. According to the AFM images, inhomogeneity of the initial glass surface was determined by scratches with a length of up to 100 nm and a depth of up to 4 nm (Fig. 3d). Aimed at

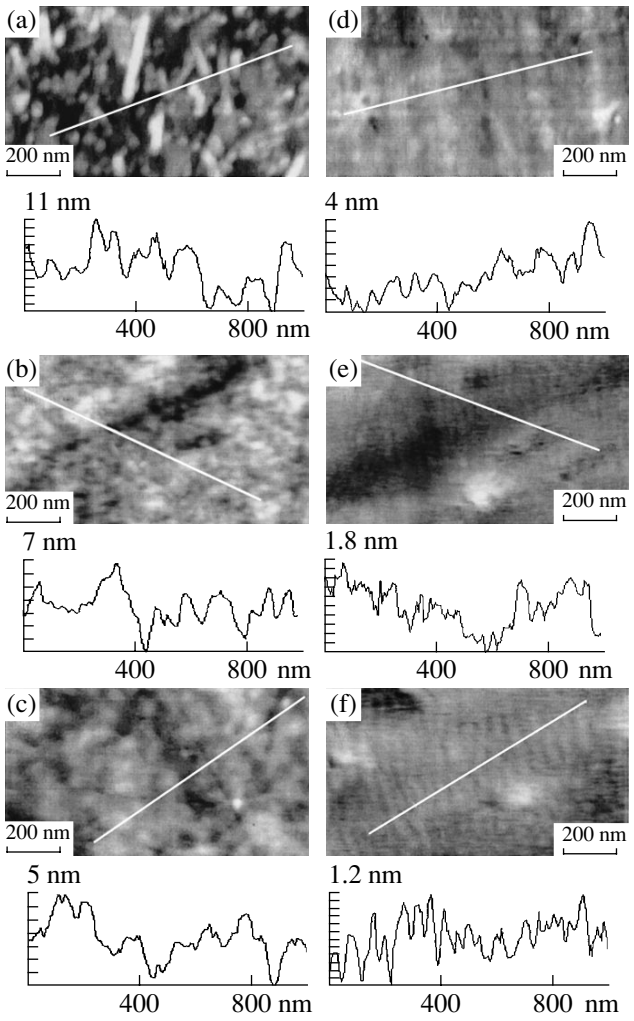

Fig. 3. Sitall and BK-7 glass surface evolution in the course of ion beam polishing: (a, b, c) AFM images of the initial, ion beam assisted sputter-deposition coated (~5 nm), and final sample sitall surface, respectively; (d, e, f) AFM images of the initial, oxygen ion etched, and final (for the process schedule, see the text) surface, respectively; the relief cross section profiles refer to the lines indicated in the corresponding AFM images.

the surface cleaning and damaged layer removal, preliminary sputtering of these samples with oxygen ions at an energy of up to 500 eV resulted in the formation of nanometer-sized cones concentrated in the regions of intersection of the scratch traces (Fig. 3e). Subsequent cycles of the sputter deposition of a BK-7 layer on the initial sample surface (2×4 nm + 3×2 nm) followed by sputter removal of a layer two times as thick allowed the final surface to be obtained with a minimum roughness height of 1.2 nm, which contained neither scratches nor cones (Fig. 3f).

Conclusion. Thus, we have developed a method for ion beam polishing of optical materials, which allows processing of the samples with a surface area of up to 100 cm^2, decreases the characteristic nanoscale roughness height to less than half of the initial value, and produces general smoothening of the shape of surface inhomogeneities. The proposed method can also be used for polishing materials other than those reported here, for example, garnet ferrite films, gallium nitride, and yttrium barium cuprates, the oxygen ion beam sputter products of which are not volatile.

Acknowledgments. This study was supported by the International Scientific-Technological Center, project no. B-176.

REFERENCES

1. P. H. Schmidt, E. G. Spencer, and E. M. Walters, J. Appl. Phys. **41** (11), 4740 (1970).
2. M. Wissing, M. Holzwarth, D. S. Simeonova, and K. J. Snowdon, Rev. Sci. Instrum. **64** (12), 4314 (1996).
3. Huashun Zhang, *Ion Sources* (Science Press: Springer, New York, 1999).
4. L. F. Johnson, J. C. North, and R. Wolfe, Appl. Phys. Lett. **44** (10), 4753 (1973).
5. A. I. Stognij, S. V. Koryakin, and V. A. Virchenko, Zh. Tekh. Fiz. **71** (6), 87 (2001) [Tech. Phys. **46**, 729 (2001)].
6. V. S. Smentkowski, Prog. Surf. Sci. **64**, 1 (2000).
7. B. Koslowski, S. Strobel, and P. Zeimann, Diamond Relat. Mater. **9**, 1159 (2000).
8. A. I. Stognij, V. T. Svirin, S. D. Tushina, *et al.*, Prib. Tekh. Éksp., No. 3, 151 (2001).
9. A. I. Stognij and S. V. Koryakin, Prib. Tekh. Éksp., No. 6, 64 (2000).
10. M. Alvisi, L. Mirenghi, L. Tapfer, *et al.*, Appl. Surf. Sci. **157**, 52 (2000).

Translated by P. Pozdeev

Technical Physics Letters, Vol. 28, No. 1, 2002, pp. 21–22. Translated from Pis'ma v Zhurnal Tekhnicheskoĭ Fiziki, Vol. 28, No. 1, 2002, pp. 49–53.

Dependence of the Spectral Resolution of an X-ray Diffractor on the Shape and Curvature of the Reflecting Surface

E. M. Latush and M. I. Mazuritsky*

Rostov State University, Rostov-on-Don, Russia

** e-mail: mazurmik@icomm.ru*

Received July 30, 2001

Abstract—Dependence of the spectral resolution of a focusing X-ray diffractor on the shape of the reflecting crystallographic planes was theoretically studied in the point source approximation. An analytical expression describing the resolution as a function of the crystal curvature in the focusing circle plane was derived. An optimum radius of the curvature ensuring the best spectral resolution was determined for a nonsymmetric diffractor scheme. © *2002 MAIK "Nauka/Interperiodica".*

X-ray radiation is usually monochromatized with the aid of perfect and mosaic crystals (quartz, silicon, germanium, lithium fluoride, mica, graphite, etc.). The traditional crystal diffraction schemes were developed and described in sufficient detail [1–4]. The spectral resolution is conventionally characterized by a dimensionless ratio $\Delta E/E$ or $\Delta\lambda/\lambda$, where E is the X-ray quantum energy and λ is the corresponding wavelength. If θ denotes the Bragg angle between the incident radiation beam and the tangent to the atomic plane of the crystal, the Bragg diffraction law stipulates that the admitted range of the Bragg angle variation $\Delta\theta$ is related to the resolution as

$$\Delta\lambda/\lambda = \Delta\theta/\tan\theta \quad (1)$$

and depends primarily on the following factors: the mosaic imperfection of the crystal, the method used for the X-ray radiation expansion into the spectrum, and the size of the Bragg zone on the reflecting surface of a crystal diffractor.

The Bragg (diffraction) reflection zone is defined as a set of points on the crystal surface for which the Bragg angle falls within $\theta - \Delta\theta \le \theta_1 \le \theta + \Delta\theta$ for a given wavelength interval $\lambda - \Delta\lambda \le \lambda_1 \le \lambda + \Delta\lambda$. The greater the $\Delta\theta$ value, the larger the diffraction zone and, hence, the higher the system aperture (transmission) and the intensity of the spectrum. However, it is usually required to provide for both large intensity and high spectral resolution (i.e., small value of the $\Delta\lambda/\lambda$ ratio). Meeting the high resolution requirement unavoidably leads to a loss of the signal intensity, so that practice usually presents a compromise between the two parameters.

At present, X-ray radiation is frequently monochromatized by reflection from flat or bent crystals. The latter diffractor type is usually employed with point radiation sources (i.e., those with dimensions not exceeding the crystal curvature radius multiplied by the resolution parameter $\Delta\lambda/\lambda$) to focus the primary X-ray beam with a given wavelength on the detector entrance window. Previously [5], we described an algorithm for and presented the results of the computer simulation of the shape of the Bragg zone on the surface of a bent crystal.

Let us study the spectral resolution of a focusing X-ray diffractor as a function of the crystal curvature in the focusing circle plane. A schematic diagram showing mutual arrangement of the radiation source *S*, the crystal diffractor *K*, and the detector *D* in the focusing circle plane is shown in the figure; *XOY* is the coordinate system; and *O*', *O* are the centers of the focusing circle and the crystal curvature, respectively. Below, *r* will denote the length of the *O'A* segment, that is, the focusing circle radius. Thus, the focusing circle in the *XOY* plane passes through the source *S*, the diffractor apex *A*, and the detector *D*.

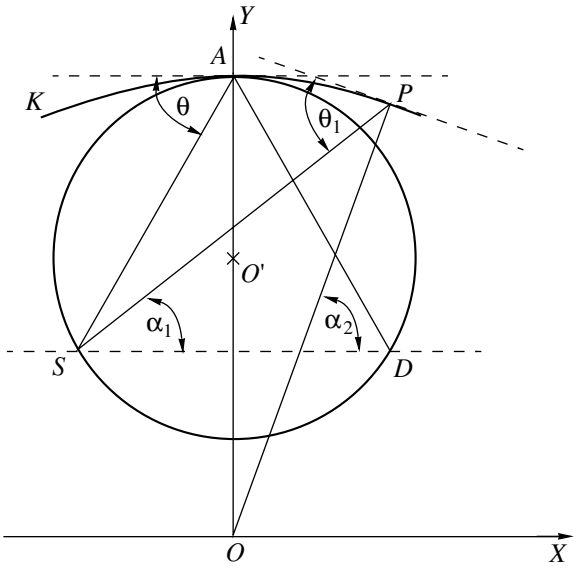

A schematic diagram showing mutual arrangement of the radiation source *S*, the crystal diffractor *K*, and the detector *D* in the focusing circle plane of a diffractor.

1063-7850/02/2801-0021$22.00 © 2002 MAIK "Nauka/Interperiodica"

Consider the most typical bent crystal shapes: cylindrical, spherical, ellipsoidal, and toroidal. A crystal section by the *XOY* plane is an arc of the circle with the radius $OA = R$, centered at the point *O*. The focusing circle plane is the symmetry plane of the crystal. Thus, the figure represents the general case of the diffractor crystal section by the focusing circle plane, which describes all types of a bent crystal. As can be seen, for any point *P* (different from the diffractor apex *A*) belonging to the reflecting crystal surface in the focusing plane, the angles θ_1 and θ are not equal. In other words, a beam strikes the point *P* at a somewhat different angle relative to the tangent as compared to the analogous angle at the point *A*. The greater the distance from point *P* to the crystal apex, the greater the difference between angles θ_1 and θ. Thus, the deviation $\Delta\theta = \theta_1 - \theta$ of the diffraction angle θ_1 from the true Bragg angle θ depends on *x* (the abscissa of point *P*). For a fixed *x*, the $\Delta\theta$ value depends on *R* (the radius of crystal bending in the *XOY* plane).

Let us study the behavior of the function $\Delta\theta = F(R)$ on the set $R \in [r, \infty)$ at a fixed value of $x \neq 0$ (for $x = 0$, $\theta_1 = \theta$ and $F(R) = 0$ for $\forall R$). We will demonstrate that $F(R)$ for $x \neq 0$ changes sign on the set $R \in [r, \infty)$ and acquires zero value at a single point of this set. Denoting the angles of *PS* and *PO* segments relative to the *X* axis by α_1 and α_2 and using the coordinates of points *P*, *O*, and *S*, we readily obtain the expressions for the slopes of these segments:

$$\tan\alpha_1 = \frac{\sqrt{R^2 - x^2} - R + 2r\sin^2\theta}{x + 2r\sin\theta\cos\theta}, \qquad \tan\alpha_2 = \frac{\sqrt{R^2 - x^2}}{x}. \tag{2}$$

Taking into account that $\theta_1 = 90° - (\alpha_2 - \alpha_1)$ (see the figure), these expressions can be transformed to

$$\tan\theta_1 = \frac{1 + \tan\alpha_2\tan\alpha_1}{\tan\alpha_2 - \tan\alpha_1} \quad \text{and}$$
$$\tan\Delta\theta = \frac{\tan\theta_1 - \tan\theta}{1 + \tan\theta\tan\theta_1}, \quad \text{where} \quad \Delta\theta = \theta_1 - \theta. \tag{3}$$

As is known, diffractors employed in X-ray spectroscopy are characterized by small values of $|x/R|$ (typically $|x/R| \leq 10^{-2}$). Expanding the quantity $\sqrt{R^2 - x^2} = R\sqrt{1 - (x/R)^2}$ into the Taylor series and ignoring the terms with x/R in powers greater than two, we obtain to within second-order terms

$$\sqrt{R^2 - x^2} \approx R - \frac{x^2}{2R}. \tag{4}$$

Using formulas (2)–(4), we can write

$$\tan\Delta\theta \approx \frac{x}{R}\frac{(2r + (x\cot\theta)/2) - R}{x\cot\theta + 2r + x^2(R - 2r)/(2R^2)}, \tag{5}$$

and

$$\Delta\theta \approx \arctan\left(\frac{x}{R}\frac{(2r + (x\cot\theta)/2) - R}{x\cot\theta + 2r + x^2(R - 2r)/(2R^2)}\right). \tag{6}$$

Since $|\Delta\theta| \leq 10^{-2}$, we may conclude that the zeros of $\Delta\theta$ coincide with the zeros of $\tan\Delta\theta$. In formula (5), the denominator is positive for any $R \in [r, \infty)$ because the parameters are determined on the segments $\theta \in [20°, 60°]$, $r \in [100\text{ mm}, 1000\text{ mm}]$, and $|x/R| \leq 10^{-2}$. Thus the $F(R)$ for $x \neq 0$ changes sign on the set $R \in [r, \infty)$ and acquires zero value at a single point of this set where the numerator is zero:

$$R = 2r + \frac{x\cot\theta}{2}. \tag{7}$$

The above-proved implies that the minimum value of $|\Delta\theta|$ is achieved under the condition (7). Since $\Delta\theta$ determines the spectral resolution (1) of the X-ray diffractor, the best spectral resolution at an arbitrary point $P(x, y)$ in the focal circle plane is achieved precisely for $R = 2r + (x\cot\theta)/2$. However, since the coordinates *x* vary at various points of the diffractor, there is no single optimum *R* value for all points of the reflecting surface. For $2r \gg (x\cot\theta)/2$, it is a common practice to take the curvature radius in the focusing circle plane equal to $R = 2r$, assuming this to be closest to optimum.

Sometimes the diffractors are designed asymmetric relative to the *YOZ* plane passing through the point *A*. An example is offered by a commercial X-ray prober microanalyzer of the Camebax-Micro type (CAMECA, France), in which the diffractor width is 37 mm on the right and 23 mm on the left of point *A*. In such cases, a minimum resolution parameter is achieved for the *R* value that is different from $2r$. Substituting $\theta = 30°$, $r = 160$ mm, and $x = 37$ mm or $x = -23$ mm into formula (7), we obtain $\Delta\theta_R$ and $\Delta\theta_L$ values for the right- and left-hand parts of the diffractor, respectively. Solving the equation $\Delta\theta_R = \Delta\theta_L$, we obtain an optimum radius $R \approx 328$ mm, which is somewhat greater than $2r = 320$ mm.

REFERENCES

1. A. K. Freund, *X-ray Optics* (ESRF, Grenoble, 1987), p. 54.
2. C. Bonnelle and C. Mande, *Advances in X-ray Spectroscopy* (Pergamon, Oxford, 1982).
3. J. W. M. DuMond and A. Kirpatrick, Rev. Sci. Instrum. **1**, 88 (1930).
4. H. H. Johann, Z. Phys. **69**, 185 (1931).
5. M. I. Mazuritskiĭ, A. V. Soldatov, E. M. Latush, *et al.*, Pis'ma Zh. Tekh. Fiz. **25** (19), 11 (1999) [Tech. Phys. Lett. **25**, 763 (1999)].

Translated by P. Pozdeev

Technical Physics Letters, Vol. 28, No. 1, 2002, pp. 23–25. Translated from Pis'ma v Zhurnal Tekhnicheskoĭ Fiziki, Vol. 28, No. 1, 2002, pp. 54–59.

Self-Similar Relief Structures on a Deformed Crystal Surface

N. N. Gorobeĭ, S. A. Knyazev, V. E. Korsukov*, A. S. Luk'yanenko, B. A. Obidov, and V. E. Khartsiev

Ioffe Physicotechnical Institute, Russian Academy of Sciences, St. Petersburg, 194021 Russia

** e-mail: Vjacheslav.Korsukov@pop.ioffe.rssi.ru*

Received August 27, 2001

Abstract—The formation of self-similar roughnesses on a deformed Ge(111) single crystal surface was observed by two independent methods: scanning tunneling microscopy and low-energy electron diffraction. In the interval of loads studied, the geometric relief parameters—lateral and vertical roughness dimensions—were in a certain ratio (5 : 1). It is suggested that this surface relief is formed by a diffusion mechanism. © *2002 MAIK "Nauka/Interperiodica".*

The method of scanning tunneling microscopy (STM) was originally applied to investigation of the influence of a biaxial tension on the surface relief of Ge(111) single crystals in [1], where we observed a pronounced effect of the mechanical loading manifested in a growth of the surface roughness over the whole scanned sample surface. The effect exhibited a threshold character and was to a considerable extent reversible with respect to the load. The maximum level of the surface roughness observed in those experiments reached several tens of nanometers in height and hundreds of nanometers in the lateral directions. Now we have studied the geometry of the surface roughness on various scales in more detail using a combination of STM with low-energy electron diffraction (LEED).

The methods of sample preparation and the experimental procedures with the sample loaded *in situ* in the scanning tunneling microscope were described elsewhere [1]. Figure 1a shows a typical relief of a deformed Ge(111) single crystal surface measured in a stationary regime (after a 1-h growth stage). As can be seen, the sample surface exhibits, in addition to the aforementioned large-scale roughness variations, certain small-scale structure levels. By increasing the STM resolution, it was possible to reveal still smaller details of the surface relief.

An analysis of the STM profiles showed that the slope of the relief details in all the scale levels does not exceed 10° (the overall descent reflects a small, about 1°, inclination of the sample). Taking into account that the relief of a crystal surface on the atomic level features a stepped structure (mostly with monoatomic steps) such as that schematically depicted in Fig. 1b, the maximum slope corresponds to a 5 : 1 ratio of the terrace width to the step height. The presence of this proportion of various scale levels is indicative of a certain self-similarity in the relief of a deformed Ge(111) single crystal surface. However, the resolving power of our scanning tunneling microscope was insufficient to follow the observed proportion reliably up to the atomic scale level.

The atomic resolution level in our experiments was reached with the aid of LEED. Previously [2], we employed this technique in studying features of the elastic deformation and fracture of the Ge(111) crystal face under the action of biaxial tension. Here we will consider another aspect of the effect of sample loading on the LEED patterns: anisotropic broadening of the diffraction reflections. Figure 2 shows the angular profiles of a LEED reflection measured by the photometry

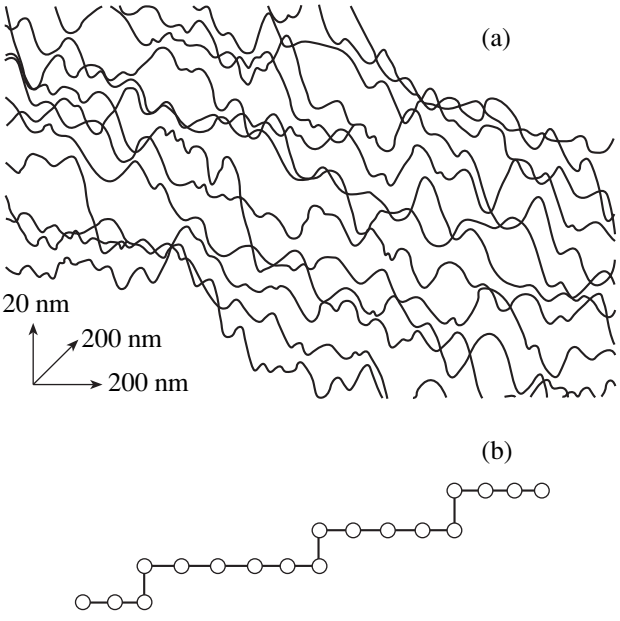

Fig. 1. (a) Typical STM profiles of the relief of a loaded Ge(111) single crystal surface (σ = 0.1 GPa); (b) a schematic diagram of the stepped relief structure on the atomic scale.

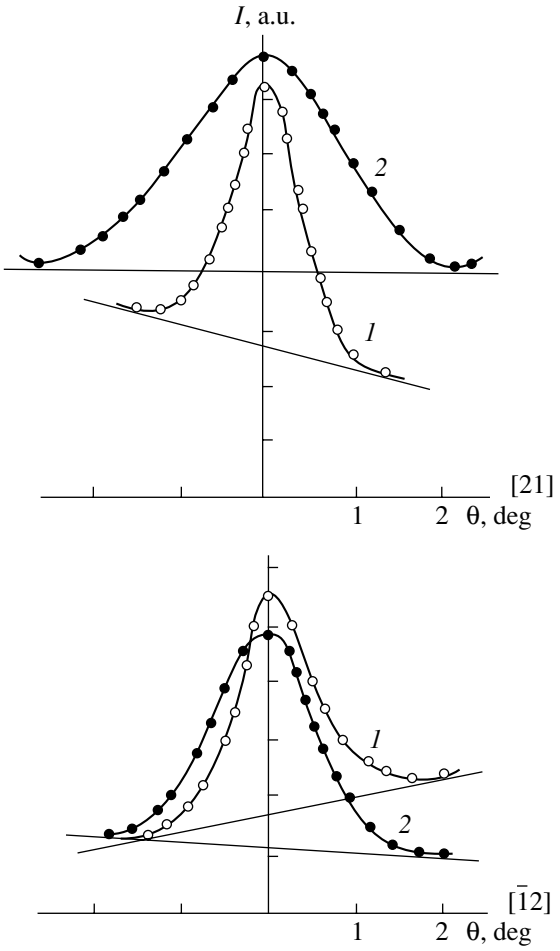

Fig. 2. Angular profiles of a LEED reflections in the two mutually perpendicular azimuthal directions for a sample loaded to $\sigma = 0.2$ (*1*) and 0.3 GPa (*2*).

in two mutually perpendicular azimuthal directions. As can be seen, the angular width of the LEED reflection in the [21] direction on the deformed surface is about three times the initial value, while there is virtually no additional broadening in the perpendicular direction. It was also found that the extent of broadening was not the same for different reflections in the LEED pattern, depending in a nonmonotonic manner on the primary electron beam energy.

Our interpretation of the anisotropic broadening effect is based on the Henzler theory [3] of the electron diffraction on a periodic stepped surface relief. According to this theory, a surface with a corrugated relief must exhibit a periodic (electron energy dependent) doubling of the diffraction reflections. The amplitude of this doubling is determined by the angle of the electron beam scattering for a given reflection and by the parameters of the stepped surface geometry. In our samples, the stepped surface structure was apparently not regular and, hence, the doubling of reflections reduces to their effective broadening. For the small-angle reflections studied in our case, the broadening is virtually insensitive to the step height and is determined primarily by the terrace width.

Estimates of the average terrace width using the Henzler theory for the experimentally observed broadening of the LEED reflections (Fig. 2) are about 30 Å, which corresponds to approximately five lattice periods. With a allowance for the most probable monoatomic step height, we arrive at the same terrace width to step height proportion of 5 : 1. However, this estimate refers to the relief of a deformed Ge(111) single crystal surface measured on the atomic scale level. Thus, the LEED data confirmed the formation of roughnesses on the deformed crystal surface with approximately the same geometric proportions as those revealed by the STM topographs. As for the azimuthal orientation of the stepped structure observed in the LEED patterns, we suggest that this feature is mostly due to the vicinal angle of the surface studied (in our case, this angle was about 0.5°).

We believe that one possible physical mechanism for the formation of roughnesses on a mechanically deformed Ge[111] single crystal face is the surface self-diffusion. Note that the roughness formation is a channel of the elastic energy release, provided that no other, more favorable channels (such as the plastic deformation) are operative [4]. In our opinion, the plastic effects, even if they take place [5], do not play a determining role on the given Ge single crystal face in the interval of loads studied. This is confirmed by reversibility of the observed effect with respect to the load magnitude. At the same time, the mechanical loading is a factor enhancing the diffusion mass transfer, provided that stress concentrators are available on the surface in the form of relief features sufficiently extended in the lateral directions.

An example is offered by an adlayer (representing an incompletely filled atomic monolayer) on a deformed crystal surface, which is strongly deformed at the edges. This implies a misfit deformation, which is mostly of a shear nature, although tensile deformations may take place as well. The magnitude of this effect is as follows: for an average substrate deformation of $\varepsilon_0 \sim 0.1\%$, the adlayer edge exhibits a shear deformation of ~10% and a tensile deformation of ~1%. These levels are critical both for the formation of misfit dislocations and for the intensive generation of adatoms involved in the diffusion mass transfer on the surface. It should be emphasized that such stress concentrators may appear only on a relief features sufficiently extended (on the order of several hundreds of nanometers for $\sigma \sim 0.1$ GPa) in the lateral directions.

Thus, biaxial tension of the Ge(111) single crystal face leads to the formation of surface roughnesses characterized by certain geometric parameters. The lateral roughness size is restricted to hundreds of nanometers, while the vertical size is such that it provides for an ele-

ment slope corresponding to a 5 : 1 lateral to vertical size ratio on all the scale levels of roughness. If our hypothesis concerning a diffusion mechanism of the surface roughness formation in a mechanical deformation field is valid, the limited slope of the atomic stepped surface structure should be attributed to the well-known effect of the step repulsion [6], which introduces elements of nonlinearity into the diffusion kinetics. Therefore, the self-similar character of the relief structure on a deformed crystal surface is a result of self-organization in a stochastic process of the diffusion mass transfer. It should be noted that a similar effect of the surface roughness formation was observed for epitaxial layers possessing a lattice misfit with respect to a substrate [7, 8].

Acknowledgments. This study was supported by the Russian Foundation for Basic Research, project nos. 99-02-18287 and 2000-00-00482).

REFERENCES

1. S. N. Zhurkov, V. E. Korsukov, A. S. Luk'yanenko, *et al.*, Pis'ma Zh. Éksp. Teor. Fiz. **51** (6), 324 (1990) [JETP Lett. **51**, 370 (1990)].
2. V. E. Korsukov, A. S. Luk'yanenko, R. R. Nazarov, *et al.*, Poverkhnost, No. 2, 69 (1988).
3. M. Henzler, Surf. Sci. **73**, 240 (1978).
4. J. Tersoff and F. K. LeGoues, Phys. Rev. Lett. **72** (22), 3570 (1994).
5. V. P. Alekhin, *Physics of Strength and Plasticity of the Surface Layers of Materials* (Nauka, Moscow, 1983).
6. J. Erlenbacher, M. J. Aziz, E. Chason, *et al.*, Phys. Rev. Lett. **84** (25), 5800 (2000).
7. C. V. Snyder, B. G. Orr, D. Kessler, *et al.*, Phys. Rev. Lett. **66** (23), 3032 (1991).
8. P. Sutter and M. G. Lagally, Phys. Rev. Lett. **84** (20), 4637 (2000).

Translated by P. Pozdeev

Technical Physics Letters, Vol. 28, No. 1, 2002, pp. 26–29. Translated from Pis'ma v Zhurnal Tekhnicheskoĭ Fiziki, Vol. 28, No. 1, 2002, pp. 60–66.

The Effect of Uniaxial Tension on the Relief Geometry of the Surface of an $Fe_{77}Ni_1Si_9B_{13}$ Amorphous Alloy

V. I. Betekhtin, P. N. Butenko, V. L. Gilyarov, V. E. Korsukov*, A. S. Luk'yanenko, B. A. Obidov, and V. E. Khartsiev

Ioffe Physicotechnical Institute, Russian Academy of Sciences, St. Petersburg, 194021 Russia

** e-mail: Vjacheslav.Korsukov@pop.ioffe.rssi.ru*

Received August 16, 2001

Abstract—The effect of uniaxial tension in a wide range of applied stress (0–3 GPa) on the surface topography of an $Fe_{77}Ni_1Si_9B_{13}$ amorphous alloy was studied by scanning tunneling microscopy. It was found that the distributions of the surface defects with respect to lateral and vertical dimensions exhibit a change manifested by an increase in the proportion of large-scale defects and in the fractal dimension of the surface with increasing load. It is suggested that this surface relief is formed by a diffusion mechanism and that the observed effects are involved in the fracture focus nucleation on the sample surface. *© 2002 MAIK "Nauka/Interperiodica".*

In recent years, there has been extensive investigation of the structure of solid surfaces [1], including amorphous metal ribbons, on the micro- and nanoscale levels in the course of changes induced by mechanical factors. This research is important for evaluation and explanation of the physical properties of these promising materials [2]. Previously [3], we applied the method of scanning tunneling microscopy (STM) to investigate the surface of a uniaxially stretched amorphous alloy foil.

In this study, our aim was to monitor transformations of the surface relief geometry of the surface of an amorphous metal alloy in the course of a stepwise increase in the load up to the fracturing of the sample. Since there exists no commonly accepted system for the classification of structural defects in amorphous materials, we have developed a "spectroscopic" approach to determine the geometric parameters for description of the transformation of a surface relief. According to this approach, the spectral state of a given surface relief is described by distributions of the heights and halfwidths of protrusions (hills) in two directions. This pattern is analogous to representation of the parameters of intensity peaks, for example, in the optical spectra of anisotropic crystals. The relief features of opposite sign, representing depressions (wells), are also described by the analogous parameters of depth and halfwidth.

The purpose of our experiments was to study the spectral and fractal state of the surface of amorphous metal ribbons depending on the level of applied mechanical load. The main analytical method was STM; additional information on the chemical composition of the sample surface was provided by Auger electron spectroscopy (AES).

The samples were prepared from $Fe_{77}Ni_1Si_9B_{13}$ amorphous alloy ribbons obtained by spin-quenching from melt in air and in vacuum. No qualitative changes were observed between the ribbons quenched under different conditions. The data presented below refer to the amorphous metal ribbons obtained in air. The samples were cut in the form of 20-mm-long, 8-mm-wide, and 20-μm-thick strips. The sample ends were clamp-fastened in a special loading device ensuring constant applied tensile stress. The load could be varied in a stepwise manner from 0 to 3 GPa.

In order to localize the fracture, half-circle cuts with a diameter of 3 mm were made on the opposite edges in the middle part of the samples. As a result, the load-carrying part of the sample had a width of 2 mm. In a sample with this geometry, a maximum of the longitudinal load in the tress profile is localized at the point of intersection of the longitudinal sample axis and the line connecting the centers of half-circle cuts. During the STM measurements, the microscope point probe was scanned in the vicinity of this very section on the sample surface. The measurements were performed on the "outer" ribbon face not contacting with the cooling wheel surface; this surface was not subjected to any pretreatment except for washing with alcohol, rinsing in distilled water, and drying. The experiments were carried out in a dry nitrogen atmosphere. The STM topographs were measured at room temperature. The images were obtained in a digitized form and processed on a computer. The spectral and fractal analyses of the STM topographs were conducted using specially developed computer software.

1063-7850/02/2801-0026$22.00 © 2002 MAIK "Nauka/Interperiodica"

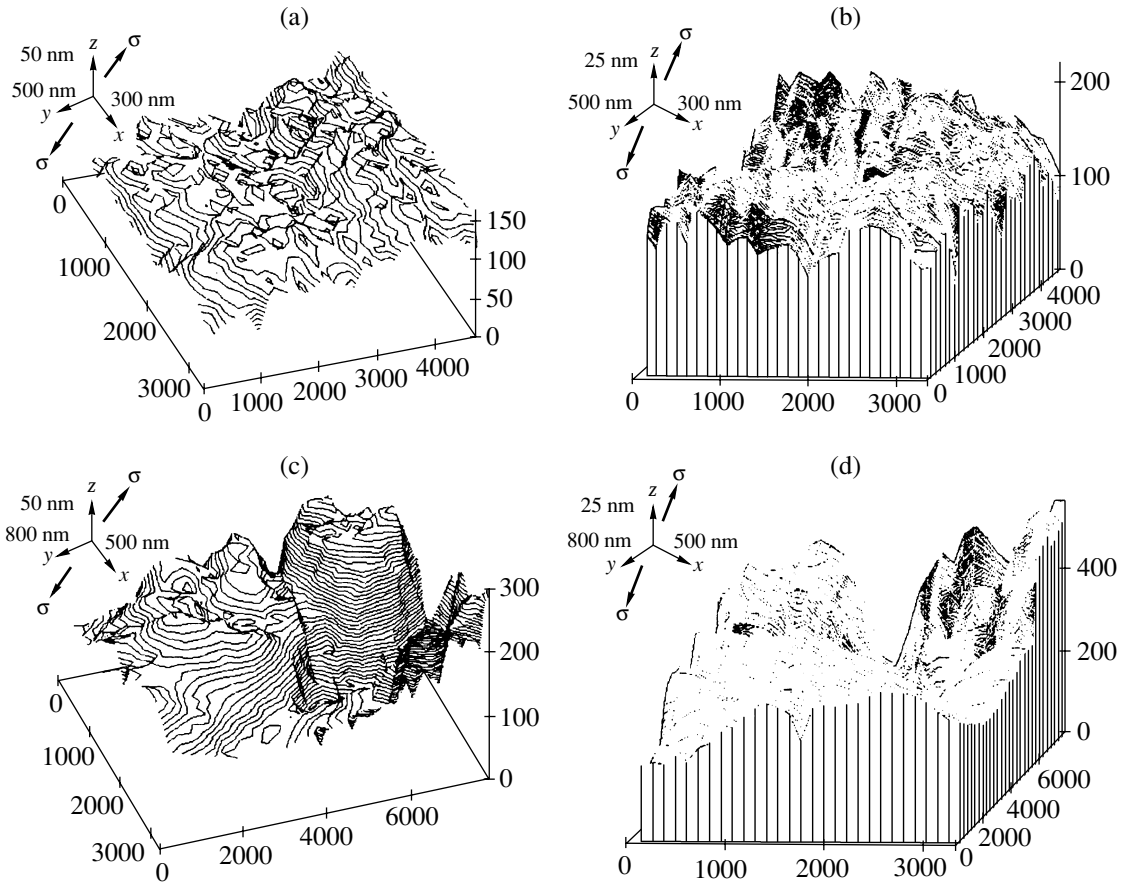

Fig. 1. STM profiles of an amorphous metal surface relief measured for various scales, directions, and loads: σ = 0.1 (a, b); 1.35 GPa (c, d).

Figure 1 shows STP topographs of the same area of an amorphous alloy sample measured under low and high loads. Although there is a striking qualitative difference, no certain conclusions can be drawn on this level except that some large-scale defects have appeared.

More definite statements can be made based on a quantitative spectral analysis of the surface relief measured during each scan of the point probe, followed by statistical data processing. In Figs. 2a–2c, the results of the profile analysis are presented in the form of distributions of the vertical and lateral hill-like defect dimensions for a sample measured under low and high load conditions. Analogous profiles were obtained for the well-like defects. An analysis of the distributions in Figs. 2a–2c allows us to draw some more profound conclusions concerning the character of changes in the sample surface relief under the action of applied stress. For example, besides an obvious increase in the proportion of large-scale defects (manifested by a peak in the right-hand wing of the solid curve in Fig. 2a), the small-scale defect fraction grows as well (see large peaks in the left-hand end of the same profile). In addition, increasing loads lead to an anisotropy in these distributions with respect to the axis of loading. On the whole, the observed changes correspond to an increase in the degree of self-similarity of the surface relief on various scale levels and to a change in the fractal dimension of the sample surface.

The fractal dimension of the surface relief was determined by the method of box accounting based on a three-dimensional lattice application. Figure 2d shows a plot of the fractal dimension versus the applied load. The fractal dimension of the initial surface ($\sigma = 0$) is $D = 2.16$, which corresponds to a fractal structure of the diffusion type. Upon loading (σ = 0.1–1 GPa), the fractal dimension drops to 2.04–2.07. Finally, prior to the sample fracture at σ = 1.35 GPa, the fractal dimension increases again to about 2.13. It must be noted that, by virtue of the STM method employed, the fractal dimensions presented here are essentially the estimates from below [4].

As noted above, the sample loading leads to an increase in the anisotropy of halfwidths of both hills and wells. This factor also qualitatively modifies the character of the fractal structure, which changes from almost symmetric in the lateral direction to quasi-one-

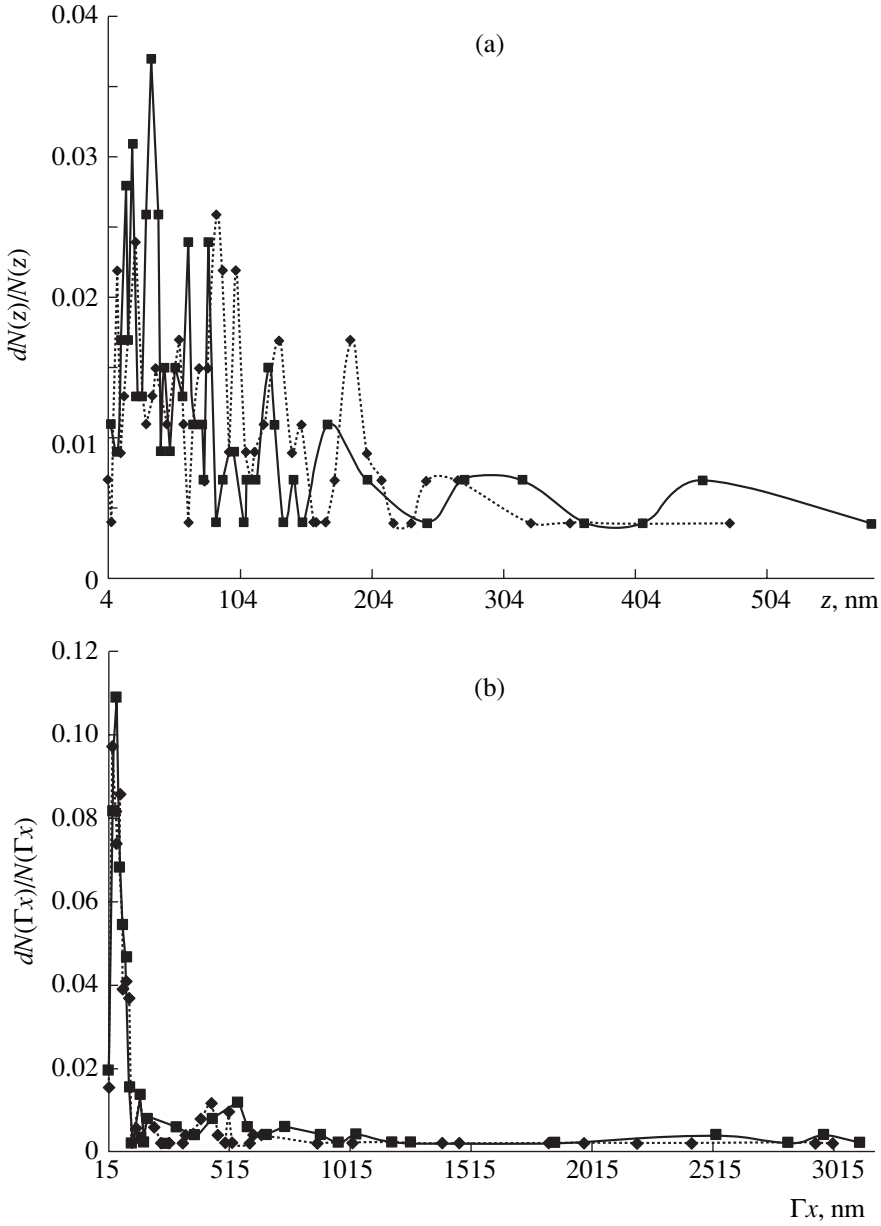

Fig. 2. (a–c) Spectral and (d) fractal characteristics of the surface relief of a sample under different loads $\sigma = 0.1$ (solid curves) and 1.35 GPa (dashed curves): (a) hill height distribution; (b) hill halfwidth distribution in the *OX* direction; (c) hill halfwidth distribution in the *OY* direction; (d) the plot of fractal dimension *D* versus applied stress.

dimensional. This pattern is characteristic of the breakage surface [5]. We believe that the formation of a new fractal structure on the sample surface favors nucleation of the primary and principal cracks in the perpendicular direction. In other words, this fractal behavior reflects a "search" for the transverse direction in which a sample exhibits the break. In this case, the fractal character of the fracture surface is a consequence of the fractal structure formed on the sample surface.

We have observed similar effects for isotropically extended surfaces of semiconductor (Ge and Si) crystals [6]. The aforementioned features of the spectral and fractal state of the surface of a material exposed to a mechanical force field allow us to suggest that one of the possible mechanisms responsible for the surface relief formation is the surface self-diffusion enhanced by the applied load. The presence of overstressed sites related to the relief features on the deformed crystal surface may lead to the athermal generation of dislocations and vacancies [7]. It is possible that these effects are even more pronounced in the case of an amorphous structure. The observed increase in the fractal dimension can be interpreted as due to a growing role of the third dimension (normal to the surface) prior to the fracture. We believe that this behavior is both a precur-

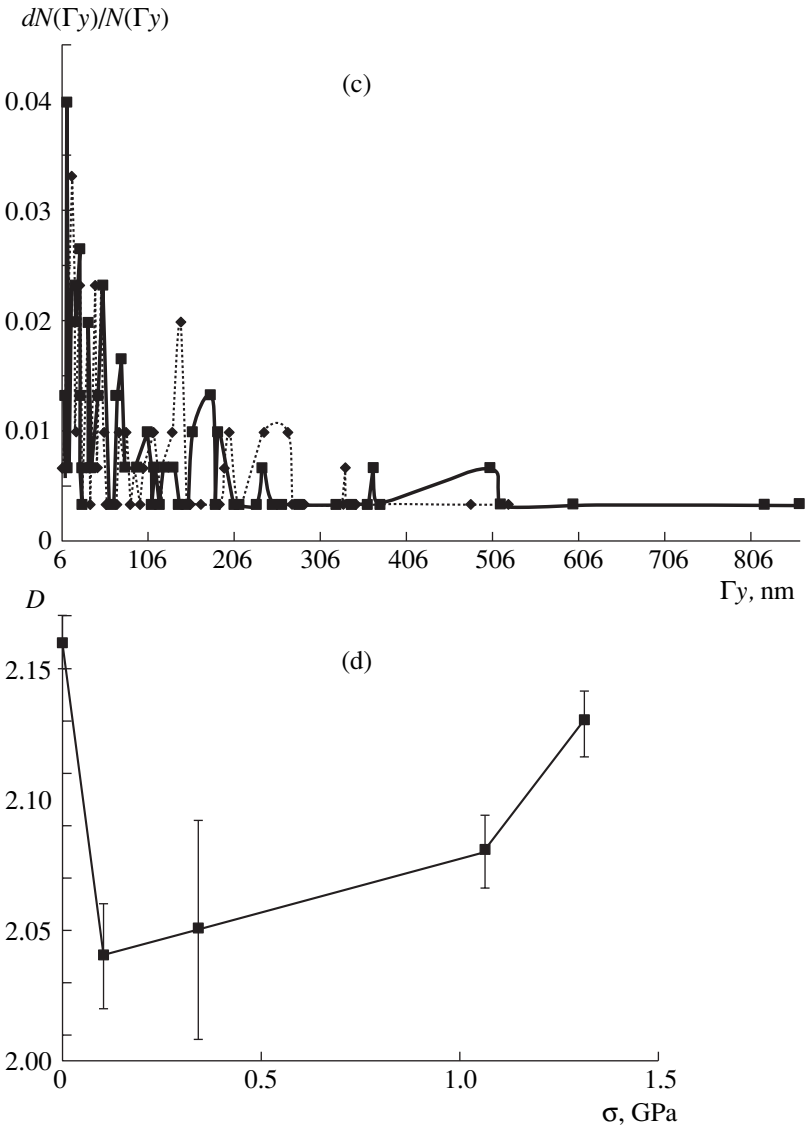

Fig. 2. (Contd.)

sor and, partly, a reason for the formation of a fracture focus on the sample surface.

Acknowledgments. This study was supported by the Russian Foundation for Basic Research (project nos. 99-02-18287 and 2000-00-00482).

REFERENCES

1. M. Filoche and B. Sapoval, Phys. Rev. Lett. **84** (25), 5776 (2000).
2. K. Suzuki, H. Fujimori, and K. Hashimoto, *Amorphous Metals* (Tokyo, 1982; Metallurgiya, Moscow, 1987), translated from Japanese.
3. V. E. Korsukov, A. S. Luk'yanenko, B. A. Obidov, *et al.*, Pis'ma Zh. Éksp. Teor. Fiz. **55** (10), 595 (1992) [JETP Lett. **55**, 621 (1992)].
4. V. I. Betekhtin, A. G. Kadomtsev, V. E. Korsukov, *et al.*, Pis'ma Zh. Tekh. Fiz. **24** (23), 58 (1998) [Tech. Phys. Lett. **24**, 932 (1998)].
5. B. B. Mandelbrot, D. E. Passoja, and A. J. Paullay, Nature **308**, 721 (1984).
6. S. N. Zhurkov, V. E. Korsukov, A. S. Luk'yanenko, *et al.*, Pis'ma Zh. Éksp. Teor. Fiz. **51** (6), 324 (1990) [JETP Lett. **51**, 370 (1990)].
7. J. Tersoff and F. K. LeGoues, Phys. Rev. Lett. **72** (22), 3570 (1994).

Translated by P. Pozdeev

Technical Physics Letters, Vol. 28, No. 1, 2002, pp. 30–32. Translated from Pis'ma v Zhurnal Tekhnicheskoĭ Fiziki, Vol. 28, No. 1, 2002, pp. 67–73.

Features of the Phase Trajectory of a Fractal Oscillator

R. P. Meĭlanov and M. S. Yanpolov

Institute for Problems of Geothermics, Dagestan Scientific Center, Russian Academy of Sciences, Makhachkala, Dagestan, Russia

e-mail: lan rus@dgu.ru

Received May 24, 2001; in final form, August 27, 2001

Abstract—Based on the solution of a system of differential equations of a fractional order α ($1 < \alpha \le 2$), a solution for the so-called fractal oscillator is obtained. It is shown that the fractal oscillator solutions provide for the parametrization of a wide class of nonlinear processes. © *2002 MAIK "Nauka/Interperiodica".*

In recent years, special attention of researchers is drawn to nonlinear dynamic systems—objects where the ideas of both deterministic chaos and fractal geometry can be implemented. These systems are especially interesting because the laws governing their behavior are of a fundamental nature, providing for a deep insight into the essence of general relationships applicable not only to physical phenomena, but to chemical, geophysical, biological, and even socioeconomic systems.

Introduction of the fractal geometry ideas [1] into natural sciences led to the formation of a new approach known as the fractal concept [2, 3]. Of special interest in the fractal concept is the development of an analytical method based on the mathematical apparatus of fractional-order integrodifferential equations [4, 5]. Using this method, it is possible to readily reproduce the known results and to establish some basically new relationships [6–10].

Below we will consider a generalized harmonic oscillator problem based on the fractional-order differential equations and show the possibility of obtaining a solution in terms of the theory of nonlinear oscillatory processes.

Mathematical methods developed for the investigation of nonlinear oscillatory processes are well known [11–15]. One can distinguish between an analytical-topological approach based on the geometric theory of differential equations [11, 12] and the approach based on an analysis of the asymptotic solutions of nonlinear differential equations containing a preset parameter [13–15]. Despite considerable effort in development of the theory of nonlinear oscillatory processes, our knowledge in this field is still far from being complete. Further development is related to basically new approaches. One of these is based on the application of the formalism of fractional-order integrodifferential equations [4, 5]. The initial equation is as follows:

$$\frac{d^\alpha}{dt^\alpha}x(t) + \omega^\alpha x(t) = 0, \qquad (1)$$

where $1 < \alpha \le 2$, ω is the frequency, and t is the time. Note that the case of $\alpha = 2$ corresponds to the classical harmonic oscillator. The system described by Eq. (1) will be referred to as the fractal oscillator.

An equation of type (1) was studied by Nigmatulin [6]. Not dwelling on the derivation of this equation, we will only study some features of the solution. It should be pointed out that one possible interpretation of the fractional derivative with respect to time is related to description of a system with partial loss of memory as a result of irreversible processes responsible for manifestations of the nonlinear properties of the system.

A solution to the differential equation (1) in the general case can be written in the following form:

$$x(t) = A(\omega t)^{\alpha-2}E_{\alpha,\alpha-1}(-(\omega t)^\alpha) + B(\omega t)^{\alpha-1}E_{\alpha,\alpha}(-(\omega t)^\alpha), \qquad (2)$$

where A and B are integration constants; $E_{\alpha,\beta}(z) = \sum_{n=0}^{\infty}\frac{z^{\alpha n}}{\Gamma(\alpha n+\beta)}$ is the Mittag–Leffler function [16]; and $\Gamma(z)$ is the Euler gamma-function.

In the case of $\alpha = 2$, the Mittag–Leffler function turns into $E_{2,1}(-z^2) = \cos(z)$, $E_{2,2}(-z^2) = \sin(z)/z$ and solution (2) acquires the well-known form $x(t) = A\cos(\omega t) + B\sin(\omega t)$. For $\alpha = 1.5$, for example, solution (2) takes the form ($z = \omega t$)

$$x(z) = A\left\{\frac{2}{3\sqrt{3}}\sin(\pi/3)[2\exp(-z/2) \times \cos(\sqrt{3}z/2 + \pi/3) + \exp(z)] + 2\sqrt{z/2}\sin(\pi/6){}_1F_3(1;\ 1/6,\ 1/2,\ 5/6;\ (z/3)^3)\right\}$$

1063-7850/02/2801-0030$22.00 © 2002 MAIK "Nauka/Interperiodica"

$$+ B\left\{\frac{2}{3\sqrt{3}}\sin(\pi/3)[2\exp(-z/2)\right.$$
$$\times\cos(\sqrt{3}z/2-\pi/3)-\exp(z)]$$
$$\left.+4\sqrt{z/\pi}\sin(\pi/6)\,{}_1F_3(1;\,1/2,\,5/6,\,7/6;\,(z/3)^3)\right\}.$$

In order to construct a phase trajectory, let us consider the parametric equations determining this trajectory:

$$x(t) = (\omega t)^{\alpha-2}E_{\alpha,\,\alpha-1}(-(\omega t)^{\alpha}),$$
$$\frac{d^{\alpha-1}x(t)}{dt^{\alpha-1}} = -\omega^{\alpha-1}(\omega t)^{\alpha-1}E_{\alpha,\,\alpha}(-(\omega t)^{\alpha}). \quad (3)$$

For $\alpha = 2$, the phase trajectory represents a circumference. In the fractional cases of $\alpha = \text{const}$ $(1 < \alpha < 2)$, the phase trajectories appear as depicted in Fig. 1a; Fig. 1b shows the corresponding curves $x(t)$. (For simplicity, the numerical calculations were performed for $\omega = 1$, $A = 1$, and $\alpha = 1.95$ (*1*), 1.5 (*2*).) As can be seen, all solutions with $1 < \alpha < 2$ correspond to decaying processes.

It should be pointed out that Eq. (1) represents essentially an infinite set of differential equations (with the power of continuum $1 < \alpha < 2$). The corresponding set of solutions is given by expression (2). Let us consider the possibility of using solutions (2), obtained for the fractal oscillator problem, as the basis set functions for a parametric representation of various nonlinear oscillations. Let $F(t)$ be a certain function of time. Consider the relationship

$$F(t) = A(\omega t)^{\alpha-2}E_{\alpha,\,\alpha-1}(-(\omega t)^{\alpha}) + B(\omega t)^{\alpha-1}E_{\alpha,\,\alpha}(-(\omega t)^{\alpha}) \quad (4)$$

as an equation with respect to α. Upon solving (4) for each set of t and ω, we determine the function $\alpha_F = \alpha_F(t, \omega, A, B)$. This function determines which solutions of set (2) existing for the given fractal oscillator will "participate" in the formation of function $F(t)$. As a result, we obtain a kind of "parametric" representation for function $F(t)$:

$$F(t) = A(\omega t)^{\alpha_F-2}E_{\alpha_F,\,\alpha_F-1}(-(\omega t)^{\alpha_F}) + B(\omega t)^{\alpha_F-1}E_{\alpha_F,\,\alpha_F}(-(\omega t)^{\alpha_F}). \quad (5)$$

It is important to note that the form of function $\alpha_F = \alpha_F(t, \omega, A, B)$ may serve as a basis for the classification of nonlinear processes. Representation (5) can be called a "multifractal" representation of function $F(t)$.

In order to demonstrate the possibilities of this representation, let us consider a reverse procedure: formally setting various $\alpha = \alpha(t)$, we will follow the formation of $F(t)$. In other words, we consider the function $\alpha_F = \alpha_F(t, \omega, A, B)$ existing for the dependences $F(t)$. The only restriction on the class of these functions $\alpha = \alpha(t)$ is that $1 < \alpha \le 2$.

For example, let α be determined as $\alpha(t) = [(1 - \delta - \varepsilon)\cos(kt) + (\varepsilon - \delta + 3)]/2$, where $\delta, \varepsilon \ge 0$, $\delta + \varepsilon < 1$, and k is an arbitrary number. The δ and ε values determine

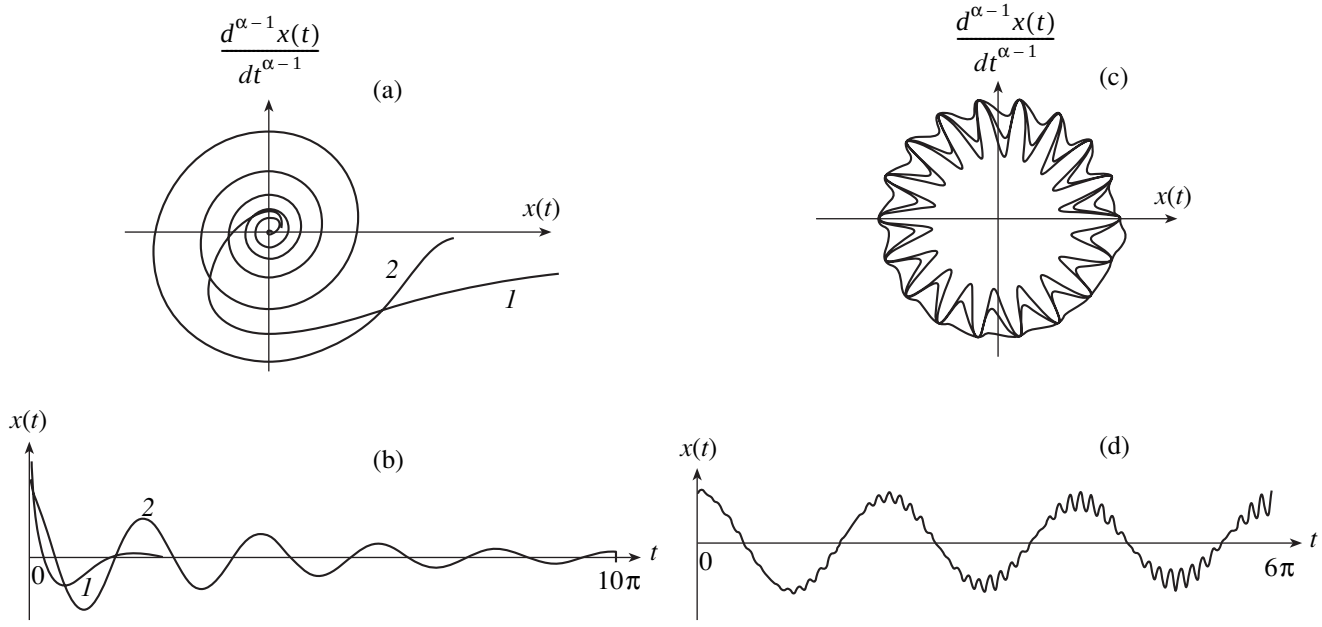

Fig. 1. The results of numerical calculation of the (a, c) phase trajectories and (b, d) $x(t)$ function for a fractal oscillator with (a, b) $\alpha = 1.5$ (*1*) and 1.95 (*2*), $t \in (0, 10\pi)$, and (c, d) $\alpha(t) = [(1 - \delta - \varepsilon)\cos(kt) + (\varepsilon - \delta + 3)]/2$, $k = 18$, $\delta = 0$, $\varepsilon = 0.95$, and $t \in (0, 6\pi)$.

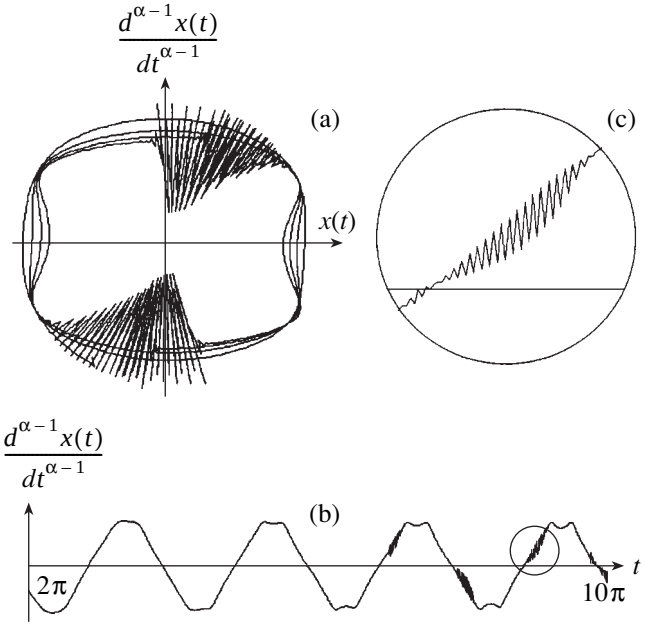

Fig. 2. The results of numerical calculation of the (a) phase trajectories and (b, c) $x(t)$ function for a fractal oscillator with $\alpha(t) = [(1 - \delta - \varepsilon)\cos(k\cos(x(t))) + (\varepsilon - \delta + 3)]/2$, $k = 7$, $\delta = 0$, $\varepsilon = 0.9$, and $t \in (2\pi, 10\pi)$.

the boundaries of variation of the $\alpha(t)$ function: $1 + \varepsilon < \alpha(t) \le 2 - \delta$. Figures 1c and 1d show the results of numerical calculations for $k = 18$, $\delta = 0$, $\varepsilon = 0.95$, and $t \in (0.6\pi)$. An analysis showed that a multiple cusp point of the phase trajectory appears at the center of the phase plane for $\delta = 0$ and $\varepsilon \longrightarrow 0.7$. In the case of $\varepsilon = 0.95$ and $0 < \delta < 0.05$, the phase trajectory is nonclosed.

Considering a different function $\alpha(t) = [(1 - \delta - \varepsilon)\cos(k\cos(x(t))) + (\varepsilon - \delta + 3)]/2$, we obtain the $F(t)$ function in the form shown in Fig. 2b; Fig. 2a shows the corresponding phase trajectory. As is seen, we have the possibility of parametrically representing a complicated nonlinear signal $F(t)$ (such as depicted in Fig. 2b) using the basis set of solutions (2). The set of solutions is selected according to the law

$$\alpha(t) = [(1 - \delta - \varepsilon)\cos(k\cos(x(t))) + (\varepsilon - \delta + 3)]/2.$$

Thus, a solution to the differential equation (1) in fractional-order derivatives contains the solution of the linear oscillator problem (as a particular case) and gives new results describing nonlinear processes. In contrast to the previously proposed methods, in which features of the phase trajectory were determined by the values of parameters entering into a given differential equation, our approach employs the fractional derivative order as an analog of such a parameter. The set of solutions (2) of the fractal oscillator problem (1) can be used as a basis set for the parametric representation of a given function $F(t)$. In this approach, the fractal parameter is considered as a parameter determining the possibility of representation of some other signal in the basis set (2).

REFERENCES

1. B. B. Mandelbrot, *The Fractal Geometry of Nature* (Freeman, New York, 1982).
2. A. I. Olemskoĭ and A. Ya. Flat, Usp. Fiz. Nauk **163** (12), 1 (1993) [Phys. Usp. **36**, 1087 (1993)].
3. V. V. Zosimov and L. M. Lyamshev, Usp. Fiz. Nauk **165** (4), 361 (1995) [Phys. Usp. **38**, 347 (1995)].
4. K. B. Oldham and J. Spanier, *The Fractional Calculus: Theory and Application of Differentiation and Integration to Arbitrary Order* (Academic, New York, 1974).
5. S. G. Samko, F. F. Kilbas, and O. I. Marichev, *Integrals and Fractional-Order Derivatives and Some Applications* (Nauka i Tekhnika, Minsk, 1987).
6. R. I. Nigmatulin, Teor. Mat. Fiz. **90** (3), 354 (1992).
7. K. V. Chukbar, Zh. Éksp. Teor. Fiz. **108** (5), 1875 (1995) [JETP **81**, 1025 (1995)].
8. R. P. Meĭlanov, Pis'ma Zh. Tekh. Fiz. **22** (23), 40 (1996) [Tech. Phys. Lett. **22**, 967 (1996)].
9. R. P. Meĭlanov and S. A. Sadykov, Zh. Tekh. Fiz. **69** (5), 128 (1999) [Tech. Phys. **44**, 595 (1999)].
10. R. P. Meĭlanov, Inzh.-Fiz. Zh. **74** (2), 34 (2001).
11. S. Lifshits, *Geometric Theory of Differential Equations* (Moscow, 1961).
12. N. V. Butenin, Yu. I. Neĭmark, and N. A. Fufaev, *An Introduction to the Theory of Nonlinear Oscillations* (Nauka, Moscow, 1976).
13. N. N. Bogolyubov and Yu. A. Mitropol'skii, *Asymptotic Methods in the Theory of Nonlinear Oscillations* (Nauka, Moscow, 1974, 4th ed.; Gordon and Breach, New York, 1962).
14. J. K. Hale, *Oscillations in Nonlinear Systems* (McGraw-Hill, New York, 1963; Mir, Moscow, 1966).
15. N. N. Moiseev, *Asymptotic Methods in Nonlinear Mechanics* (Nauka, Moscow, 1981).
16. M. M. Dzharbashyan, *Integral Transformations and Function Representations in Complex Domain* (Nauka, Moscow, 1966).

Translated by P. Pozdeev

Technical Physics Letters, Vol. 28, No. 1, 2002, pp. 33–35. Translated from Pis'ma v Zhurnal Tekhnicheskoĭ Fiziki, Vol. 28, No. 1, 2002, pp. 74–80.

An Effective High-Power KrCl Excimer Barrier-Discharge Lamp

M. I. Lomaev, V. F. Tarasenko, and D. V. Shitts

Institute of High-Current Electronics, Siberian Division, Russian Academy of Sciences, Tomsk, Russia

e-mail: VFT@loi.hcei.tsc.ru

Received August 16, 2001

Abstract—The effect of the pumping pulse power and shape on the discharge character and the efficiency of emission from KrCl* molecules ($\lambda \sim 222$ nm) is studied. In the coaxial quartz tube KrCl excimer lamps excited by a barrier discharge, the maximum emission efficiencies are observed for a discharge in the form of diffuse cones. Based on these results, an excimer lamp with an average output power of up to 100 W is created. © *2002 MAIK "Nauka/Interperiodica".*

Introduction. At present, excimer lamps excited by a barrier discharge are among the simplest and most promising sources of UV and vacuum UV radiation [1–8]. However, the efficiency of conversion of power supplied to the working medium into that of optical radiation in the cited works exhibits a considerable scatter. Moreover, only restricted and rather contradictory data are available on the optimum pumping conditions and filament shapes in the barrier discharge.

Recently [4, 5], we reported that using a sinusoidal voltage with a frequency of 22 kHz for the excitation of Xe_2, Kr_2, Ar_2, KrCl, and XeCl excimer lamps with barrier discharge is advantageous to short (50–100 ns) high-voltage pulses. The main reason for low efficiency in the latter case is that a significantly greater breakdown voltage has to be to applied to the discharge gap. As a result, the normalized electric field strength E/p (E is the field strength and p is the pressure) deviated from optimum for the formation of exciplex molecules. At the same time, an increase in the efficiency of a Xe_2 barrier-discharge lamp excited with short (250–750 ns) pulses in comparison to the case of sinusoidal excitation at the same frequency (tens of kilohertz) was demonstrated in [6, 7]. Vollkommer and Hitzschke [6] suggested that the observed increase in the emission efficiency is due to the optimum electron energy distribution function provided by the short-pulse excitation. Mildron and Carman [7] pointed out that an increase in the efficiency of the Xe_2^* lamp was achieved when a homogeneous (diffuse) discharge was formed with an electron density significantly lower as compared to that typical of the filaments. The discharge homogeneity was provided by a steep front of the excitation voltage pulse.

The purpose of our experiments was to investigate in detail how the excitation pulse power and shape, as well as some other parameters, affect the efficiency of emission from KrCl* molecules pumped by the barrier discharge. The results of this study allowed us to create an excimer lamp with an average output power of up to 100 W.

Experimental. We employed coaxial quartz excimer lamps of traditional design with two barriers and a water-cooled internal tube [1, 3]. The gap width between the quartz tubes was 6–9 mm and the excitation region length could be varied from 5 to 75 cm. The working gas mixtures were prepared immediately inside the lamp bulb. A high voltage was applied to the outer metal grid electrode.

The emission power was determined using a calibrated photodetector of the FEK-22 SPU type. The excitation power was determined by two techniques. The first method was based on the well-known voltage–charge loop patterns [9, 10] and the second, on the measurement of voltage across the discharge gap (with an allowance for the voltage drop on the lamp capacitance). In the latter case, it was also possible to determine the instantaneous power and, hence, the excitation energy deposited over a certain period of time. The pumping was provided by two generators, one of which produced a sinusoidal voltage with a frequency of 17 kHz and the other generated unipolar or bipolar voltage pulses with a base duration of ~2 μs, controlled rise- and falltime (250–1000 ns), and a repetition frequency varied from 10 to 100 kHz.

The pulses of current, voltage, and emitted radiation were measured using a current shunt, voltage divider, and a FEK-22 SPU photodetector with a TDS-220 oscillograph, respectively. In some cases, an additional capacitor was included into the lamp circuit in order to measure the voltage drop on the excimer lamp capacitance. The signal from this capacitor was also recorded with the TDS-220 oscillograph. The discharge glow was photographed using a digital camera.

Results and discussion. In the first step, we optimized the pressure and composition of the Kr–Cl_2 gas mixture. The best results were obtained for the mixture with Kr : Cl_2 = 200 : (1–0.5) at a total pressure of about

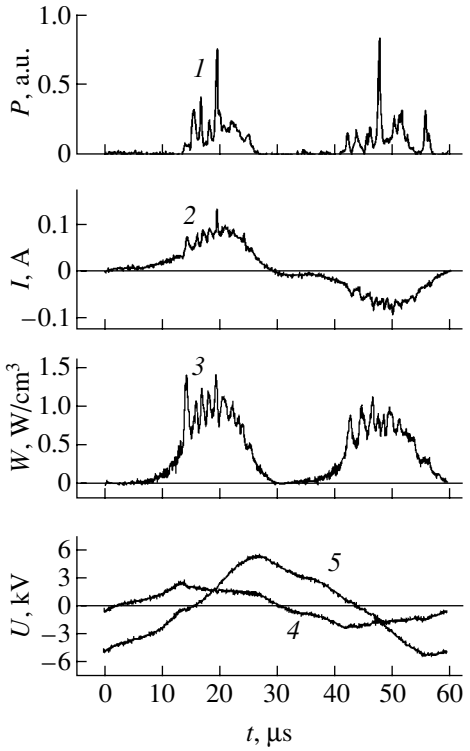

Fig. 1. Typical oscillograms of the pulses of (*1*) emission from the B–X transition in the KrCl* molecule, (*2*) current, and (*5*) interelectrode voltage measured in the excimer lamp pumped by a sinusoidal signal. Curves *3* and *4* show the calculated time variation of the specific excitation power and the voltage drop across the discharge gap, respectively.

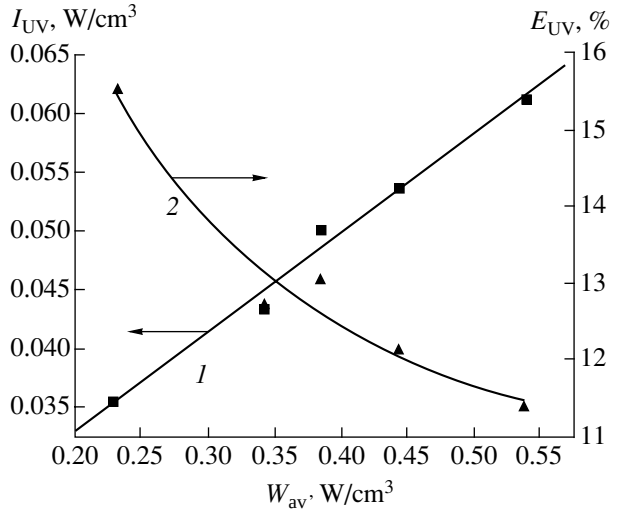

Fig. 2. Plots of the (*1*) specific average emission power and (*2*) efficiency versus the specific average excitation power for a KrCl excimer lamp pumped from a bipolar pulse generator with the leading and trailing pulse front widths of ~250 ns.

200 Torr. As the total pressure or the Cl_2 content in the mixture was decreased, the bulk discharge became more homogeneous but the emission power decreased. An increase in the total pressure or the Cl_2 content in the mixture led to a discharge contraction by means of the formation of bright channels, which was also accompanied by a decrease in the emitted power.

As mentioned above, the experiments were carried out with generators providing a pulsed excitation voltage of different shapes. Figure 1 shows typical oscillograms of the pulses of current, interelectrode voltage, and emission from the B–X transition in the KrCl* molecule together with the calculated curves of the excitation power and the voltage drop across the discharge gap for the lamp pumped by a sinusoidal signal. Analogous data were also obtained for a lamp pumped by unipolar and bipolar pulses with a base duration of ~2 μs and a front width of 250 ns or ~1 μs. Some experiments were performed at a reduced pressure of the working gas mixture.

Observations of an integral pattern of the discharge glow gave the following results. The lamp operating at a reduced pressure (about 100 Torr or below) and pumped by short bipolar or unipolar pulses features a bulk discharge without filaments. Pumped by the sinusoidal pulses at a gas pressure of 200 Torr, the excimer lamp exhibits both a bulk glow and a discharge consisting of diffuse filaments. A discharge in the lamp operating at an optimum pressure (about 200 Torr) and pumped by bipolar or unipolar pulses is entirely composed of filaments. The filaments have the shape of two diffuse cones facing one another and linked with a brighter streak, the length and visible intensity of which depend on the working gas pressure, pumping power, and the pulse shape and repetition rate. For the pumping voltage pulses with steep fronts, the streak length and brightness drop to leave a discharge in the form of two diffuse cones.

The results of measurements of the output UV radiation power and efficiency showed that the regimes of maximum efficiency (reaching 11–15% of the energy deposited into a discharge plasma) take place when the lamp is pumped by pulses possessing steep fronts, which produce a discharge in the form of diffuse cones (Fig. 2). The use of unipolar pulses instead of bipolar led to an insignificant (5–10%) decrease in the emission efficiency. An increase in the rise- and falltime of the pumping voltage pulse also somewhat reduced (by approximately 10%) the maximum efficiency. Pumped in the optimum regime, the excimer lamp with an excitation region length of 47 cm and a gap width of 9 mm between the quartz tubes was characterized by an average emission power of up to 100 W. The use of a generator producing a sinusoidal voltage instead of the short pulses further reduced the maximum efficiency (to 8–11%), but this decrease was also not very pronounced (~25% relative to maximum). A significant drop in the efficiency was observed in response to a decrease in the working gas pressure. The efficiency of the lamp operating at a pressure reduced to 100 Torr, even pumped from the pulsed source, did not exceed 4%. The main reason for this change is a significant dif-

ference in specific excitation power deposited in the discharge gap occupied by the filaments versus the homogeneous discharge. This difference may reach up to two orders of magnitude and above because the volume occupied by the filaments is smaller (by the same factor, as determined in our experiments) than the total gas discharge volume taken into account in determining the specific excitation power.

A comparative analysis of the normalized electric field strength E/p, the specific excitation power (per unit volume or per particle), and the efficiency determined for the experimental conditions studied in these experiments and for the glow discharge [11] showed the following. First, the glow and barrier (filamented) discharge conditions with comparable efficiencies of 12–14% are characterized by close values of the reduced field ($E/p \sim$ 8–10 V/(cm Torr)) and specific excitation power (about a few tens of W/cm^3 or $(10–50) \times 10^{-18}$ W/particle). Note that, for the barrier discharge, it is necessary to take into account only the volume occupied by the filaments. Second, the homogeneous barrier discharge (exhibiting no visible filaments) with a significantly lower efficiency (~4%) is characterized by a significantly lower specific excitation power of 0.3–3 W/cm^3 or $\approx(0.2–2) \times 10^{-18}$ W/particle at a higher reduced field strength of $E/p \geq$ 15 V/(cm Torr). In the lamp pumped by a sinusoidal generator, the decrease in the efficiency is also explained by the fact that part of the energy is deposited into the bulk discharge.

The values of energy deposited into the discharge plasma within one oscillation period per unit barrier discharge volume depends significantly on the specific capacitance of the quartz tube barriers, which usually amounts to 1.5 pF/cm^2. Thus, a discharge consisting of diffuse filaments is necessary for reaching a high emission efficiency in the lamps excited with the barrier discharge.

Conclusion. Thus, we have studied how the excitation pulse power and shape, as well as some other parameters, affect the efficiency of emission from KrCl* molecules in the excimer lamps pumped by the barrier discharge. It was demonstrated for the first time that the presence of filaments representing spatial zones with a high specific excitation power in the barrier discharge is a necessary condition for reaching a high operation efficiency in KrCl excimer lamps with this type of pumping. This is related to the fact that a homogeneous discharge occupying the whole barrier gap volume is characterized by a specific excitation power significantly below the optimum level. Based on the results obtained, a KrCl excimer lamp was created with an average output power of up to 100 W in the UV range with a maximum emission at 222 nm.

Acknowledgments. The authors are grateful to the International Scientific-Technological Center (project no. 1270) and LLNL (contract B5066095) for the financial support for this study.

REFERENCES

1. B. Eliasson and U. Kogelschatz, IEEE Trans. Plasma Sci. **19**, 309 (1991).
2. J.-Y. Zhang and I. W. Boyd, J. Appl. Phys. **80**, 633 (1996).
3. V. S. Skakun, V. F. Tarasenko, E. A. Fomin, and A. A. Kuznetsov, Zh. Tekh. Fiz. **64** (10), 147 (1994) [Tech. Phys. **39**, 1054 (1994)].
4. M. I. Lomaev, V. S. Skakun, É. A. Sosnin, *et al.*, Opt. Atmos. Okeana **11** (2-3), 277 (1998).
5. A. M. Boichenko, V. S. Skakun, E. A. Sosnin, *et al.*, Laser Phys. **10** (2), 540 (2000).
6. F. Vollkommer and L. Hitzschke, in *Proceedings of the 8th International Symposium LS-8, Graifswald, Germany, 1998*, p. 51.
7. R. P. Mildron and R. J. Carman, J. Phys. D **34**, L1 (2001).
8. G. V. Zvereva and G. N. Gerasimov, Opt. Spektrosk. **90** (3), 376 (2001) [Opt. Spectrosc. **90**, 321 (2001)].
9. T. C. Manley, Trans. Electrochem. Soc. **84**, 83 (1943).
10. Z. Falkenstein and J. J. Coogan, J. Phys. D **30**, 817 (1997).
11. A. N. Panchenko, E. A. Sosnin, and V. F. Tarasenko, Opt. Commun. **161**, 249 (1999).

Translated by P. Pozdeev

Technical Physics Letters, Vol. 28, No. 1, 2002, pp. 36–38. Translated from Pis'ma v Zhurnal Tekhnicheskoĭ Fiziki, Vol. 28, No. 1, 2002, pp. 81–88.

A Mechanical Model for Investigation of the Phenomenological Properties of Materials Possessing a Domain Structure

A. T. Ovakimyan

Institute of Optical and Physical Measurements, Yerevan, Armenia

Received August 13, 2001

Abstract—A model, analogous to that used in mechanics, is proposed for description of the processes of magnetization in magnetic materials and electrization in ferroelectrics. The possibility that the proposed model is realized in the nature is discussed. © *2002 MAIK "Nauka/Interperiodica".*

The possibility of using a model, analogous to that employed in mechanics (mechanical model), for description of the process of magnetization in magnetic materials is justified by the following considerations. Since the magnetic field is a vector quantity, the resulting magnetic moment **M** of a system equals a vector sum of the magnetic moments of domains $\mathbf{m}_i$; the latter are composed of the magnetic moments of the elementary sources of magnetism [1].

In a homogeneous ferromagnetic single crystal magnetized to saturation in an external magnetic field, where all magnetic moments of the domains are parallel and oriented in one direction (Fig. 1), the total magnetic moment **M** applied at the point C_m (coinciding with the geometric center of the single crystal) is also oriented in the same direction. If the crystal is remagnetized to saturation in any other direction, the direction of **M** will change, while the position of the point C_m must remain the same, as follows from the properties of parallel vectors.

In the absence of an external field (or in a weak field), the crystal will separate into domains such that the position of the point C_m in the crystal will remain unchanged, otherwise the law of energy conservation would be violated [2]. Indeed, if the crystal is suspended at the center of mass in a constant magnetic field and set to rotation, the domains will also rotate and move. If the resulting magnetic moments of the domains were reoriented so that the point C_m would shift, the crystal would experience mechanical rotating moments relative to the point of suspension and, hence, would permanently rotate in a constant magnetic field, which is impossible.

Coordinates of the point C_m are readily determined for the limiting case, whereby a homogeneous crystal is magnetized to saturation: this point must coincide with the geometric center (center of mass) of the crystal. An analogous conclusion can be derived based on the dipole considerations. Indeed, let us consider the crystal side to which the vector **M** points the north pole, and the opposite side as the south pole (*N* and *S*, respectively, in Fig. 2). According to the dipole properties, we cannot magnetize one pole stronger than the other. This must be valid for an arbitrary magnetization direction, which is only possible if **M** is a bound vector always applied at the geometric center of the crystal. This property of the resulting magnetic moment, together with a hysteresis providing for the stable magnetization direction in permanent magnets, is treated by an external observer as evidence of the dipole.

The above conclusion can be extended to arbitrary solids showing a domain structure and possessing dipole properties. This is possible provided that a solid represents a bound system in which the domain orientations are correlated so that the whole sample volume is a self-organizing system. The conclusion is valid for polycrystalline and amorphous solids as well.

Conceptually, this can be justified in two ways: (i) magnetic moments of the elementary sources of magnetism behave so that any reorientation obeys the energy conservation law; (ii) the energy conservation law requires that the elementary sources of magnetism

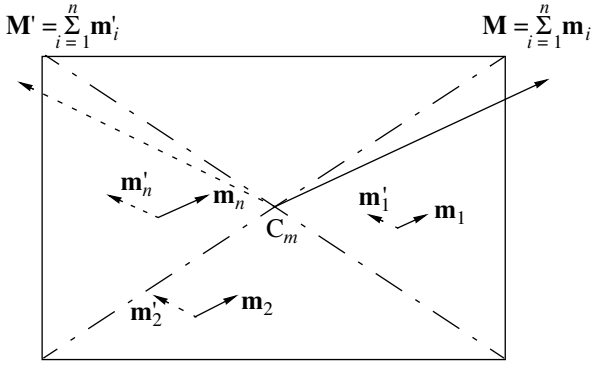

Fig. 1.

1063-7850/02/2801-0036$22.00

would behave in this very manner. For experimental verification of the fact that the point C_m is immobile, it expedient to employ the following scheme. A thin ferromagnetic film should be taken with the dimensions such that the whole sample would be observed in a device for the observation of magnetic domains (in the simplest case, the domain moments are either parallel or antiparallel). The sample is photographed in a magnetic field of variable strength and orientation. The results are conveniently processed in a graphical form by determining the geometric center (point C_m) and drawing the coordinate axes X and Y originating from C_m. The axes are oriented so that Y axis would coincide with one direction of the domain magnetization (see Fig. 2, which schematically shows a band domain structure of a crystal or a thin ferromagnetic film).

For the plane sample under consideration, we can write (by analogy with the method used for determination of the center of mass in the mechanics) the following relationships (for the general case, see [1]):

$$\sum_{j=1}^{P} \mathbf{m}_j x_j = 0, \quad \sum_{k=1}^{q} \mathbf{m}_k x_k = 0,$$
$$\sum_{j=1}^{P} \mathbf{m}_j y_j = 0, \quad \sum_{k=1}^{q} \mathbf{m}_k y_k = 0, \tag{1}$$

where $\mathbf{m}_j$ and $\mathbf{m}_k$ are the magnetic moments of the domain regions oriented upward and downward along the Y axis, respectively; x_j, y_j, x_k, y_k are the coordinates of the points of magnetic moment application (geometric centers) of the corresponding domain regions. Taking into account that the magnetic moments of the domains are proportional to their areas, relationships (1) can be rewritten as

$$\sum_{j=1}^{P} S_j x_j = 0, \quad \sum_{k=1}^{q} S_k x_k = 0,$$
$$\sum_{j=1}^{P} S_j y_j = 0, \quad \sum_{k=1}^{q} S_k y_k = 0, \tag{2}$$

where S_j and S_k are the areas of domain regions oriented upward and downward along the Y axis, respectively.

In the structure depicted in Fig. 2, conditions (2) are satisfied. In the general case, the domains can possess an arbitrary shape but conditions (2) must be always valid to within the energy conservation law for the macroscopic structures (i.e., completely). This proves that point C_m must be immobile.

If the result were negative, the possible instrumental error would have to be checked. Otherwise, not only the energy conservation law would be broken, but two other absurd conclusions could be made as well: (i) an asymmetric magnet with differently magnetized poles exists and (ii) the magnetic field is not a vector field since the vector summation rule is not valid.

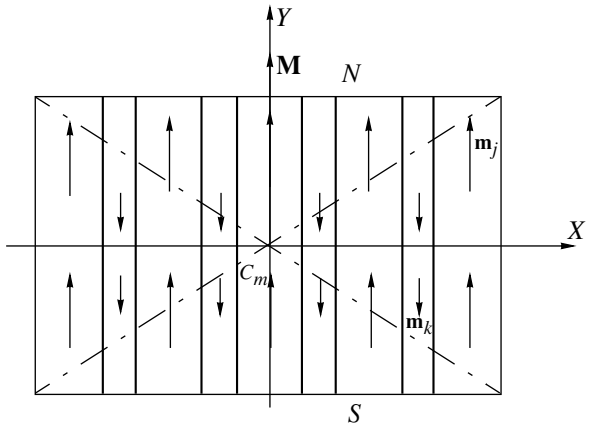

Fig. 2.

The above experiment is conveniently performed with a thin ferromagnetic film, in which the domain thickness can be assumed the same and sufficiently small (tens to hundreds of Ångströms) and the analysis performed in a plane variant. Note that the domain boundaries are magnetically neutral and can be ignored in the calculations. By homogeneous magnetic materials we imply those composed entirely of domains or containing small uniformly distributed inclusions not possessing any intrinsic domain structure. The separate coarse inclusions should excluded from considerations, after which the point C_m will certainly shift from the geometric center of the sample. In all cases, coordinates of the point C_m are conveniently determined for the limiting case of a sample magnetized to saturation.

It should be emphasized that the constant position of the point C_m, following from the energy conservation law, can be considered only with respect to an external magnetic field. If a part of the sample would be heated above the Curie point and the other part would be simultaneously cooled and/or deformed so as to change the shape, point C_m would shift. In this case, the energy conservation law is not violated because an additional energy (thermal or mechanical) is introduced into the closed system.

Let us consider the corollaries of the above law.

1. The process of magnetization of a homogeneous magnetic needle can be described as follows. In a demagnetized state, $\mathbf{M} = 0$. Under the action of an external magnetic field, the domains rotate and move so that their magnetic moments add to give rise to a total moment $\mathbf{M}$ applied at point C_m coinciding with the center of mass of the needle (or, in the general case, in the vicinity of this center). When the external field changes in magnitude or direction, the moment $\mathbf{M}$ applied at C_m also varies (which is treated by an external observer as evidence of the dipole behavior). The interaction of the magnetic needle with a loop (or a coil) carrying constant electric current can be considered as the interaction of two vectors representing magnetic moments of

the needle and the loop and applied at their geometric centers.

In this analysis, the concept of a magnetic neutral used in practical electrical engineering acquires a physical meaning. The neutral can be determined as a plane containing point C_m and perpendicular to the magnetic moment **M**. If the needle is cut into pieces, the magnetic domains will redistribute so that point C_m of each part would coincide with the corresponding geometric center. Obviously, this will lead to minimum energy losses provided that the orientation of the magnetic moment in each part will be close to or coincide with the direction of vector **M** of the initial needle.

2. If a homogeneous ferromagnetic solid is placed inside a coil carrying electric current, a pulling force arises (analogous to attraction in mechanics) that tends to bring the C_m points of the two objects together. After matching these points, the pulling force becomes zero. This is obvious for a magnetic needle and can be readily confirmed in experiment for an arbitrary solid. In the general case, this phenomenon explains the principle of action of electrical machines by the interaction of two vectors representing magnetic moments of the rotor and stator systems.

3. For a limited thickness of the domain boundary, the rigid requirement concerning absolute immobility of point C_m leads to the following effects:

(i) Under certain conditions, immobility of the point C_m during the rotation of domains can be ensured only at the expense of deformation of a magnetized solid (the Barkhausen effect);

(ii) When the rotation of domains ceases, immobility of the point C_m can be sometimes also provided only in a deformed solid (positive or negative magnetostriction effects). On the contrary, mechanical stresses changing the shape of a solid (and, hence, shifting point C_m) unavoidably lead to reorientation of the magnetic domains;

(iii) There must exist certain directions in which, keeping point C_m immobile, the domains can reorient with minimum energy losses irrespective of being amorphous or crystalline (anisotropic effects).

The above considerations entirely apply to ferroelectrics polarized in an external electric field, which reflects similarity of the phenomenological properties of ferromagnetic and ferroelectric materials.

The aforementioned processes are conveniently simulated on a computer using a program stipulating a preset initial state of the domains (magnitudes and orientations of $\mathbf{m}_i$), unchanged coordinates of point C_m coinciding with the geometric center of a homogeneous sample, and maximum possible domain wall thickness. The simulations are performed by varying the magnitude and direction of **M**, which is equivalent to changing the applied magnetic field.

In conclusion, it should be noted that the ability of the proposed mechanical model to predict the properties of magnetic materials and ferroelectrics is quite convincing enough to suggest that this very model is operative in nature. This is consistent with Newton's profound analogies between various forces known at that time, according to which the magnetic force is applied, like the force of gravity, to the center of a magnetized body.

REFERENCES

1. S. V. Vonsovskiĭ, *Magnetism* (Nauka, Moscow, 1984; Wiley, New York, 1974).
2. A. T. Ovakimyan, Pis'ma Zh. Tekh. Fiz. **24** (15), 90 (1998) [Tech. Phys. Lett. **24**, 620 (1998)].

Translated by P. Pozdeev

Technical Physics Letters, Vol. 28, No. 1, 2002, pp. 39–40. Translated from Pis'ma v Zhurnal Tekhnicheskoĭ Fiziki, Vol. 28, No. 2, 2002, pp. 1–5.

The Electron Energy Distribution in Standing Striation Bands

S. D. Wagner, S. U. Nisimov, A. A. Khitrov, and A. V. Chervyakov

Petrozavodsk State Pedagogical University, Petrozavodsk, Karelia, Russia

e-mail: andrewch@karelia.ru

Received July 24, 2001

Abstract—The electron energy distribution was measured in standing striation bands provoked by a local magnetic field applied to the positive column of a glow discharge plasma in neon. The electron energy distribution function exhibits a pronounced second maximum, the position of which varies depending on the striation region. The experimental results are interpreted in terms of the nonlocal electron kinetics. © *2002 MAIK "Nauka/Interperiodica".*

The phenomenon of ionization wave generation (striation) in the positive glow discharge column in neon has been known for a long time [1]. Moreover, the striated positive column is the most typical form of the discharge plasma in most gases and mixtures. The striation bands can be either moving or standing. The standing striations occur on the anode side of any perturbation in a homogeneous discharge plasma. For example, the perturbation may be represented by an electric probe introduced into the discharge, local magnetic field, cathode discharge region, etc. Below we report on the experimental determination of the electron energy distribution function (EEDF) in the standing striation bands provoked by a local magnetic field applied to a positive glow discharge column in neon.

The experiments were performed in a glass tube containing a hollow cold cathode, a mobile flat anode, and an immobile cylindrical 2-mm-long probe with a diameter of 0.2 mm situated at the tube axis. The tube radius (R = 16 mm) and the glow discharge conditions (current I, 5–15 mA; neon pressure P, 1 Torr) were selected so as to provide for the absence of moving striation bands. The EEDF was measured using the second derivative of the probe current with respect to the potential; the plasma potential was determined at the second derivative zero. The spatial distribution of the intensity of optical emission from the glow discharge was studied with the aid of a prism monochromator equipped with a spatial scan system.

The formation of standing striation bands was provoked by applying the magnetic field of two small permanent magnets mounted on the glass tube so that the field direction was perpendicular to the tube axis. The magnets were selected so as to produce a local perturbation in the homogeneous positive plasma column. The magnetic field strength at the tube axis was B = 100 G. The perturbation region exhibited an increase in the optical emission intensity. The regions of increased glow brightness were periodically repeated with decay on the anode side of the perturbation, thus forming a standing striation band pattern.

If the permanent magnets were moved along the tube, the related striation bands changed their positions as well. Thus, it was possible to study the characteristics of various band regions with the aid of the probe situated at the discharge tube axis. Figure 1 shows the EEDFs experimentally measured at various distances from the magnetic perturbation source.

The results of our measurements showed that the EEDF exhibits a pronounced second maximum corresponding to various kinetic energies depending on the

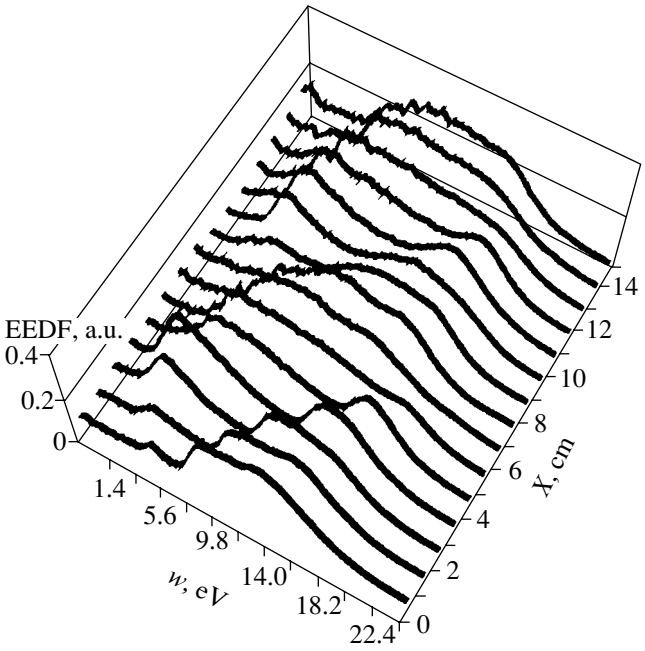

Fig. 1. Electron energy distribution function measured with a probe situated at various distances X from the magnetic perturbation source (P = 1 Torr, I = 10 mA, R = 16 mm, B = 100 G).

1063-7850/02/2801-0039$22.00 © 2002 MAIK "Nauka/Interperiodica"

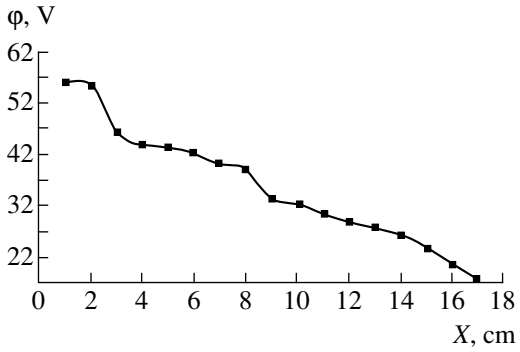

Fig. 2. The spatial profile of a plasma potential measured in standing striation bands.

striation region. The EEDF was measured over a distance including two striation bands. As can be seen, the second peak in the EEDF of the second band is less pronounced as compared to the analogous feature in the first band. This is related to a decrease in the striation amplitude with increasing distance from the perturbation source. The second EEDF maximum appears in the region of lower energies and shifts toward higher energies with increasing coordinate X. Reaching the energy corresponding to inelastic collisions, the second peak gives rise to increased glow and shifts back toward small kinetic energies, after which the process is repeated. It should be noted that the results of these EEDF measurements in the standing striation bands are very much like those obtained when the EEDF was measured in moving low-amplitude striations in a glow discharge formed under close conditions [2].

Figure 2 shows the results of measurements of the plasma potential variation along the discharge tube axis. As can be seen from these data, the potential profile exhibits a certain periodicity. A change in the potential is correlated with the second EEDF peak shift on the energy scale.

The obtained experimental results were analyzed within the framework of the nonlocal electron kinetics [3]. When the electron energy losses for inelastic collisions are small, the motion of electrons has a diffusion character with a total energy of $\varepsilon = w + e\varphi$, where w is the kinetic energy and $e\varphi$ is the potential energy. The total electron energy may change only as a result of inelastic collisions, which take place when the electron energy exceeds the excitation threshold ε_1. This character of the electron motion determines the spatial periodicity of the plasma parameters, which is characterized by the characteristic length $\lambda_\varepsilon = \varepsilon_1/eE$, where e is the electron charge and E is the longitudinal electric field strength. When a perturbation source deforming the EEDF appears in the positive plasma column, the perturbation acquires a periodic character. For neon (ε_1 = 16.6 eV) under the discharge conditions studied (E = 2 V/cm) [4], we obtain λ_ε = 8 cm, which approximately corresponds to the observed striation band length.

Acknowledgments. This study was supported by the Russian Foundation for Basic Research, project nos. 06-02-16327, 01-02-06350, and 01-02-06356.

REFERENCES

1. A. V. Nedospasov, Usp. Fiz. Nauk **94**, 439 (1968) [Sov. Phys. Usp. **11**, 174 (1968)].
2. Yu. B. Golubovskiĭ, S. U. Nisimov, and I. A. Porokhova, Zh. Tekh. Fiz. **67** (2), 24 (1997) [Tech. Phys. **42**, 145 (1997)].
3. L. D. Tsendin, Plasma Sources Sci. Technol. **4**, 200 (1995).
4. S. D. Wagner, S. U. Nisimov, V. P. Pyadin, *et al.*, Fiz. Plazmy **24** (7), 633 (1998) [Plasma Phys. Rep. **24**, 584 (1998)].

Translated by P. Pozdeev

Technical Physics Letters, Vol. 28, No. 1, 2002, pp. 4–5. Translated from Pis'ma v Zhurnal Tekhnicheskoĭ Fiziki, Vol. 28, No. 1, 2002, pp. 11–14.

Ion Deposition Modifies the Surface of Track Membranes

V. A. Pronin*, V. N. Gornov, A. V. Lipin, P. A. Loboda, B. V. Mchedlishvili, A. N. Nechaev, and A. V. Sergeev

Institute of Technical Physics, State Nuclear Research Center of the Russian Federation, Snezhinsk, Russia

** e-mail: c5@five.ch70.chel.su*

Shubnikov Institute of Crystallography, Russian Academy of Sciences, Moscow, 117333 Russia

Received August 1, 2001

Abstract—The ion deposition of thin silicon oxide films renders the surface of track membranes hydrophilic. The modified surface is characterized by a wetting angle of 20–25° remaining unchanged for a long time. © *2002 MAIK "Nauka/Interperiodica".*

Introduction. The track membranes, obtained by exposing thin polymeric films to ionizing radiation beams followed by etching, are widely used in various fields of science and technology, in particular, for the separation and purification of polymer solutions on a molecular level. The track membranes are made predominantly using poly(ethylene terephthalate) (PET) films with an initial thickness of 10–20 μm. However, the surface of such membranes is hydrophobic, which significantly limits the possible practical applications. In medicine and biotechnology, the tasks involving filtration of blood plasma or separation of viruses require hydrophilic nonadsorbing membranes [1].

For this reason, extensive research in many laboratories all over the world is aimed at finding simple technological methods for polymer surface modification, which would impart the required hydrophilic properties to PET membranes. Rendered hydrophilic, the modified track membranes possess unique technical characteristics. The investigations allowed a number of physical and chemical methods to be developed, which provide for the desired surface modification of track membranes [2]. One of the most effective and nondamaging (from the standpoint of introducing additional defects into the membrane surface) techniques is offered by the glow discharge plasma treatment [3]. However, a significant disadvantage of this method is the small lifetime of the hydrophilic state of the membrane: the plasma-treated surface is subject to rapid contamination when exposed to the environment. As a result, the hydrophobic properties are usually restored already after 1–2 days [3].

Below we describe a new method, based on the ion deposition of thin silicon oxide films, which provides for the obtaining of track membranes with a sufficiently long lifetime of the hydrophilic surface state.

Experimental procedure and results. Thin silicon oxide films were deposited onto the surface of track membrane microfilters by method of electron beam evaporation of a silicon oxide target in vacuum. The membrane samples were mounted in a sample holder to which a negative voltage of 300 V was applied relative to the vacuum chamber walls. The process of ion deposition under these conditions ensured the best adhesion of the silicon oxide film to the PET surface. This provided for the most compact film structure approaching that of a continuous material [4]. Inhomogeneity of the silicon oxide film thickness over the surface of a microfilter with a diameter of 200 mm did not exceed 2%, which was achieved with the aid of a planetar sample rotation system. The silicon oxide film thickness was determined in the course of deposition with the aid of an AOS-3S acoustooptical spectrophotometer. The measurement error was ~5%.

The silicon oxide coatings were deposited onto 160×160 mm PET microfilters. Prior to being placed in a vacuum chamber, the samples were washed in hot distilled water and dried. Then the microfilters were mounted in special sample holders and four such holders with samples were arranged in the planetar rotation system. A residual air pressure in the working chamber was $\sim 5 \times 10^{-6}$ Torr. Prior to the film deposition, the surface of samples was cleaned by a 10–15-min treatment in a glow discharge plasma. Then the silicon oxide film was deposited at a residual pressure of $\sim 10^{-5}$ Torr. Samples of 10-μm-thick PET microfilters with pore diameters of 0.05 and 0.2 μm were coated with 0.02-, 0.04-, or 0.08-μm-thick films.

The hydrophilic properties of the samples were characterized by determining the wetting angle for water. The error of these measurements was ±5%. For the comparison, the wetting angles were determined both on the membrane side with deposited silicon oxide and on the uncoated rear side. Each sample had a diameter of 60 mm and was characterized by an average of the results of three measurements at various points uniformly scattered over the surface. The wetting angle measurements were performed first 1 h after the silicon

1063-7850/02/2801-0004$22.00 © 2002 MAIK "Nauka/Interperiodica"

The results of experimental determination of the wetting angle on track membranes

N	*l*	*d*	θ	$\theta_1(t)$ (*t* in days)					θ_2
				t = 1	*t* = 5	*t* = 10	*t* = 15	*t* = 30	
1	0.02	0.05	76	20	23	18	21	22	
2	0.02	0.2	72	16	22	16	20	21	
3	0.04	0.05	73	17	18	20	16	22	15–20
4	0.04	0.2	70	21	16	18	20	18	
5	0.08	0.05	75	19	21	15	17	21	
6	0.08	0.2	74	15	22	20	15	19	

Note: *N* is the number of experiment; *l* is the deposited silicon oxide layer thickness (in μm); *d* is the membrane pose diameter (in μm); and θ, θ_1, and θ_2 are the wetting angles of the uncoated PET membrane side, silicon oxide coated membrane side, and KU-1 quarts plate, respectively (in deg).

oxide film deposition and then repeated after storage for 1, 5, 10, 15, and 30 days. For the reference, analogous measurements were performed on the polished surface of a KU-1 quartz plate.

The results of determination of the wetting angle for the surface of track membranes stored for 1–30 days are summarized in the table.

Conclusion. As can be seen from the experimental data presented in the table, the hydrophilic state of the surface of PET track membranes with deposited silicon oxide films is retained for 30 days, with a wetting angle of 20–25°. The wetting angles of the silicon oxide coated microfilters are close to the value for a massive quartz plate. We believe that the proposed method of membrane surface hydrophilization provides for a real possibility of expanding the range of practical applications of the PET-based track membranes in science and technology.

Acknowledgments. This study was supported by the International Scientific-Technological Center, project no. 918.

REFERENCES

1. A. M. Cherkasov and V. A. Pasechnik, *Membranes and Sorbents in Biotechnology* (Khimiya, Leningrad, 1991).
2. *Proceedings of the All-Russia Conference on Membranes and Membrane Technology "Membranes-95," Moscow, 1995.*
3. A. Mass, H. Jaaba, F. Shue, *et al.*, J. Macromol. Sci., Pure Appl. Chem. **A34** (1), 67 (1997).
4. G. F. Ivanovskiĭ and V. I. Petrov, *Ion-Plasma Material Treatment* (Radio i Svyaz', Moscow, 1986).

Translated by P. Pozdeev

Technical Physics Letters, Vol. 28, No. 1, 2002, pp. 41–43. Translated from Pis'ma v Zhurnal Tekhnicheskoĭ Fiziki, Vol. 28, No. 2, 2002, pp. 6–11.

The Effect of Charge Relaxation on the Electromagnetic Radiation of an Oscillating Charged Viscous Drop

S. O. Shiryaeva, A. I. Grigor'ev, V. A. Koromyslov, and A. S. Golovanov

Yaroslavl State University, Yaroslavl, Russia

e-mail: shir@uniyar.ac.ru

Received July 16, 2001

Abstract—A dispersion equation for the capillary oscillations of a charged drop of incompressible liquid possessing a finite electric conductivity is derived with an allowance for the energy lost as a result of the electromagnetic wave emission. The magnitude of the electromagnetic radiation losses of the oscillating drop linearly increases with the electric conductivity and the surface mobility of charge carriers. © *2002 MAIK "Nauka/Interperiodica".*

Introduction. Investigations of the electromagnetic radiation of oscillating charged liquid drops (e.g., in clouds, fogs, and rains) are of interest from the standpoint of problems encountered in the remote sounding of such objects [1–3] and in the development of instrumentation for a broad spectrum of applications involving the electric dispersion of liquids [4–6]. The problem of calculating the intensity of electromagnetic radiation of an oscillating charged drop was originally formulated [1] for a nonviscous ideally conducting drop oscillating in vacuum.

In view of the importance of the problem, it is also interesting to answer the question as to how will the radiation intensity be affected by nonideality of the physical properties of the oscillating drop such as the viscosity and finite charge transfer velocity.

Problem formulation. Consider a drop of ideal incompressible perfectly conducting liquid with the radius R, density ρ, permittivity ε_1, conductivity σ, surface tension γ, kinematic viscosity ν, and charge Q in vacuum ($\varepsilon_2 = 1$). Let us study the capillary oscillations of such a system in a spherical coordinate system with the origin at the drop center. The description will assume that the oscillations may decay both due to viscosity and as a result of emitting electromagnetic waves generated by a moving charge redistributed in the course of oscillations. The calculations below will be performed in terms of the dimensionless variables for which $R = 1$, $\rho = 1$, and $\gamma = 1$. In these variables, the system of electrohydrodynamic equations describing the liquid motion in the electric field created by the charge Q is as follows:

$$\frac{\partial \mathbf{u}}{\partial t} + (\mathbf{u}\cdot\nabla)\mathbf{u} = -\nabla P_1 + \nu\Delta\mathbf{u}; \quad \mathrm{div}\mathbf{u} = 0;$$

$$\mathrm{div}\mathbf{D}_j = 0; \quad \mathbf{D}_j = \varepsilon_j\mathbf{E}_j;$$

$$\Delta\mathbf{E}_j + \frac{1}{c^2}\frac{\partial \mathbf{E}_j}{\partial t^2} = 0; \quad j = 1, 2,$$

where the subscripts 1 and 2 refer to the liquid and medium, respectively; $\varepsilon_1 \equiv \varepsilon$; $\mathbf{u}(\mathbf{r}, t)$ is the liquid velocity field in the drop; $P_1(\mathbf{r}, t)$ is the pressure inside the drop with an allowance for the external electric field; and c is the electromagnetic wave propagation velocity.

The free liquid surface is described by the equation

$$F(\mathbf{r}, t) \equiv r - 1 - \xi(\theta, t) = 0$$

and must obey a set of boundary conditions. These include the kinematic condition

$$\frac{dF}{dt} \equiv \frac{\partial F}{\partial t} + \mathbf{u}\cdot\nabla F = 0;$$

the dynamic condition for the tangential components of the stress tensor

$$(\Pi_{2\tau} - \Pi_{1\tau}) - \nu\cdot[\boldsymbol{\tau}\cdot(\mathbf{n}\cdot\nabla)\mathbf{u} + \mathbf{n}\cdot(\boldsymbol{\tau}\cdot\nabla)\mathbf{u}] = 0;$$

$$\Pi_\tau = \frac{\varepsilon}{4\pi}E_n E_\tau;$$

(E_n and E_τ are the normal and tangential components of the electric field vector, respectively; $\mathbf{n}$ and $\boldsymbol{\tau}$ are the unit vectors in the normal and tangential directions to the drop surface, respectively); and the dynamic condition for the normal component of the stress tensor

$$-(P_1 - P_2) + 2\nu\mathbf{n}\cdot(\mathbf{n}\cdot\nabla)\mathbf{u} - P_E + P_\gamma = 0$$

(P_2 is the external medium pressure, P_E and P_γ are the pressures produced by the electric forces and surface tension, respectively).

1063-7850/02/2801-0041$22.00

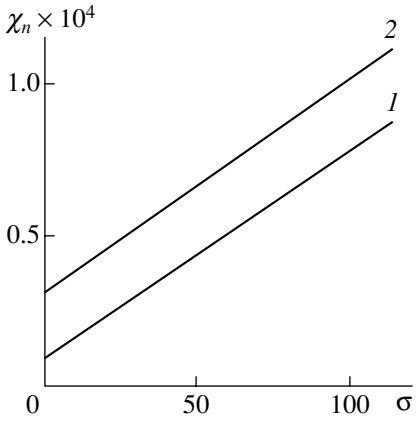

Fig. 1. The plots of dimensionless damping χ_n versus dimensionless conductivity σ for the capillary oscillations (n = 100) of a liquid drop with Q = 1, b = 0.5, ε = 80, and ν = 0 (*1*) or 10^{-9} (*2*).

The boundary conditions for the electric induction $\mathbf{D}_j(\mathbf{r}, t)$ and the surface charge density $\kappa(\theta, t)$ are as follows:

$$r = 1 + \xi;\ D_{2n} - D_{1n} = 4\pi\kappa;\quad E_{2\tau} = E_{1\tau};$$

$$\frac{\partial\kappa}{\partial t} - \sigma(\mathbf{n}\cdot\mathbf{E}_1) + \mathrm{div}_\Sigma(\kappa\mathbf{u}_\tau + \kappa b\mathbf{E}_\tau) = 0;$$

$$-\frac{1}{4\pi}\oint_S \kappa ds = Q,\quad S = [r = 1 + \xi(\theta, t),\ 0 \le \theta \le \pi],$$

$$r \longrightarrow \infty;\ D_2 \longrightarrow 0,$$
$$r \longrightarrow 0;\ D_1 \longrightarrow 0,$$

where b is the surface charge carrier mobility, $\mathbf{u}_\tau$ and $\mathbf{E}_\tau$ are the velocity and field vector components in the tangential plane, and $\mathrm{div}_\Sigma\mathbf{a}$ is the surface divergence.

In addition, the drop is assumed to obey conditions of the volume constancy

$$\int_V dV = \frac{4}{3}\pi$$

and the center-of-mass immobility

$$\int_V \mathbf{r}dV = 0.$$

Problem solution and discussion. The above set of equations is a mathematical formulation of the problem that can be solved by standard techniques (see, e.g., [1, 7, 8]). The solution leads to a dispersion equation describing the spectrum of periodic and aperiodic motions in the liquid:

$$\begin{aligned}
&(S - 2g_n\nu)\Big[S^2 + n(n-1)(n+2)\\
&+ \frac{Q^2}{2\pi}n - \frac{Q}{4\pi}B_nG_nn^2(n+1)\Big]\\
&+ 2S^2\nu(n-1)(2n+1)\\
&- S^2\frac{Q}{4\pi}G_n\Big[H_ng_n - \frac{S}{c}(n+1)(2n+1)\Big]\\
&+ S\nu\frac{Q}{4\pi}G_n[2g_nn^2(n+1)\\
&- n(n-1)(n+1)^2 + 4H_ng_nn + H_nn(n^2-1)(n-2)]\\
&- 4S\nu^2g_nn(n-1)(n+2) + \frac{Q}{4\pi}G_ng_nn\\
&\times\left\{H_n\Big[\frac{Q^2}{2\pi} - (n-1)(n+2)\Big] - \frac{Q^2}{4\pi}n(n+1)\right\} = 0;
\end{aligned} \tag{1}$$

$$H_n \equiv -n - (2n+1)\frac{S}{c};\quad g_n(x) \equiv x\frac{i_{n+1}(x)}{i_n(x)};\quad x \equiv \sqrt{\frac{\nu}{S}};$$

$$B_n \equiv \frac{2S + n\lambda_n}{n(n+1)};\quad G_n \equiv \frac{Q}{S - f_n\lambda_n};$$

$$\lambda_n \equiv \varepsilon S + 4\pi\sigma + bQ(n+1);\quad f_n \equiv \frac{H_n}{(n+1)},$$

where S and n are the frequency and number of the capillary oscillation mode, respectively, and $i_n(x)$ is the modified spherical Bessel function.

A numerical analysis of the dispersion equation (1) showed that the capillary oscillation damping χ_n related to the electromagnetic wave emission grows by a linear law in proportion to the electric conductivity σ and the surface carrier mobility b. This is illustrated in Figs. 1 and 2, showing the plots of χ_n versus σ and b for the mode with n = 100 and the dimensionless frequency $\mathrm{Im}S \approx 1500$ (for a drop with R = 1 mm, this corresponds to ≈200 kHz). The electromagnetic radiation frequency increases in proportion to $\sim\chi_n\exp(2\chi_nt)$. As can be seen in Fig. 1, the presence of a small viscosity does not influence dependence of the radiative oscillation damping on the electric conductivity σ, producing only a parallel shift of the plot. The results of numerical calculations using solution (1) showed that the dependence $\chi_n = \chi_n(\sigma, b)$ remains linear even for greater viscosities. An increase in the charge Q (i.e., in the surface charge density κ) and the capillary oscillation mode number n at a finite conductivity σ and finite charge mobility b leads to a quadratic growth of χ_n with respect to both Q and n, which agrees with the data [1] for nonviscous perfectly conducting liquid drops.

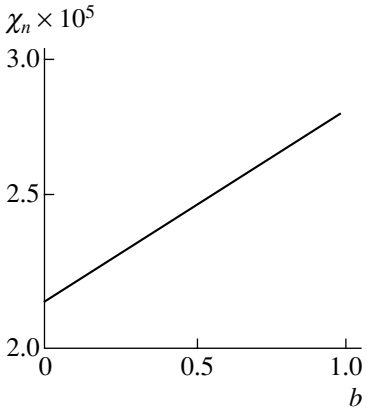

Fig. 2. The plot of dimensionless damping χ_n versus dimensionless surface charge carrier mobility b for the capillary oscillations ($n = 100$) of a liquid drop with $\sigma = 25$, $\varepsilon = 80$, and $\nu = 0$.

The viscosity, while not modifying the functional dependence of the radiative oscillation damping $\chi_n = \chi_n(\sigma, b)$, affects the capillary oscillation frequency. As the ν value increases, the frequency decreases until the oscillations cease completely, after which the drop will no longer radiate at this mode. For example, the numerical calculation showed that the oscillations with $n = 100$ cease at $\nu \approx 0.05$, while the fundamental mode with $n = 2$ ceases at $\nu \approx 0.75$. It is important to note that the electromagnetic radiation intensity at a fixed frequency is proportional to the square of this frequency [1].

In real systems of charged natural liquid drops, the main contributions to the integral electromagnetic radiation (e.g., of a cloud) in the region of frequencies on the order of 10^2 kHz are from the oscillations with $n = 2$ in very small drops ($R \sim 10$ μm) possessing a maximum concentration, as well as the high-mode ($n \sim 100$) oscillations with large amplitudes related to hydrometeors with dimensions $R \sim 100$–1000 μm.

Conclusion. The intensity of electromagnetic radiation from an oscillating charged drop possessing a finite electric conductivity σ and surface charge carrier mobility b linearly increases in proportion to the σ and b values. Dependence of the radiation intensity on the drop charge Q and the oscillation mode number n is the same as that for the perfectly conducting drop. The effect of the liquid viscosity ν on the electromagnetic radiation reduces to influencing the drop oscillation frequency $\mathrm{Im}S = \mathrm{Im}S(\nu)$.

Acknowledgments. This study was supported by Presidential Grant no. 00-15-9925.

REFERENCES

1. V. I. Kalechits, I. E. Nakhutin, and P. P. Poluéktov, Dokl. Akad. Nauk SSSR **262** (6), 1344 (1982).
2. L. G. Kachurin, *Physical Principles for Influencing Atmospheric Processes* (Gidrometeoizdat, Leningrad, 1990).
3. K. V. Beard and Ali Tokay, Geophys. Res. Lett. **18** (12), 2257 (1991).
4. A. I. Grigor'ev and S. O. Shiryaeva, Izv. Akad. Nauk, Mekh. Zhidk. Gaza, No. 3, 3 (1994).
5. A. I. Grigor'ev, Zh. Tekh. Fiz. **70** (5), 22 (2000) [Tech. Phys. **45**, 543 (2000)].
6. D. F. Belonozhko and A. I. Grigor'ev, Élektrokhim. Obrab. Met., No. 4, 17 (2000).
7. A. I. Grigor'ev and S. O. Shiryaeva, Izv. Akad. Nauk, Mekh. Zhidk. Gaza, No. 5, 107 (1997).
8. S. O. Shiryaeva, Zh. Tekh. Fiz. **69** (8), 28 (1999) [Tech. Phys. **44**, 894 (1999)].

Translated by P. Pozdeev

Technical Physics Letters, Vol. 28, No. 1, 2002, pp. 44–47. Translated from Pis'ma v Zhurnal Tekhnicheskoĭ Fiziki, Vol. 28, No. 2, 2002, pp. 12–20.

Quantum Dots in $YBa_2Cu_3O_{6+x}$ Films with a Tetragonal Structure

V. D. Okunev[a,*], Z. A. Samoĭlenko[a], V. A. Isaev[a], A. Klimov[b], and S. J. Lewandowski[b]

[a] *Donetsk Physicotechnical Institute, National Academy of Sciences of Ukraine, Donetsk, Ukraine*

[b] *Institute of Physics, Polish Academy of Sciences, Warsaw, Poland*

* *e-mail: okunev@host.dipt.donetsk.ua*

Received June 4, 2001

Abstract—Experimental evidence is presented for the existence of clusters possessing metallic conductivity in epitaxial $YBa_2Cu_3O_{6+x}$ ($x < 0.4$) films with a tetragonal structure. Despite the overall dielectric state, the optical transmission spectra reveal the regions of absorption due to free charge carriers. The presence of metallic clusters is also confirmed by the X-ray diffraction data. At low temperatures, these metallic clusters are capable of converting into quantum dots responsible for the $\rho(T)$ = const regions in the temperature dependence of the electric resistance. The process of cluster formation can be enhanced by high-power laser (KrF) radiation.

Recently [1–3], it was reported that the temperature dependences of resistance measured for the dielectric films of YBaCuO, PrCaMnO, and LaSrMnO systems exhibit regions of $\rho \cong \rho(T)$ = const at $T < T_{crit}$ = 130–240 K. The films, obtained by a pulsed laser deposition technique, contained small-size clusters with metallic conductivity. It was concluded [3] that the observed phenomena are explained by the quantum confinement effects [4, 5], whereby very small clusters (with dimensions on the order of a few nanometers) transform into quantum dots with an atomic-like spectrum; a system of such tunneling-coupled quantum dots can be responsible for the $\rho(T)$ = const behavior observed at low temperatures.

For the YBaCuO system, the $\rho(T)$ = const effect was observed in amorphous films. Below we present the results of the first experiments on creating such clusters in crystalline YBaCuO films. For this purpose, we selected $YBa_2Cu_3O_{6+x}$ layers possessing a tetragonal structure for $x > 0$. In contrast to amorphous YBaCuO films, where the metallic clusters are formed in a disordered (dielectric) medium [1, 6], the formation of such clusters in the crystalline matrix involves local rearrangement of the crystal structure with variation of the oxygen content. Apparently, the process of cluster formation can be stimulated by external factors, for example, by shortwave high-power laser radiation capable of influencing the atomic order in the irradiated material [7]. Since the most stable $YBa_2Cu_3O_{6+x}$ compositions are obtained for x = 0 and 7.0 [8], the laser action upon the samples can be expected to induce a phase separation in the system with the formation of dielectric (matrix) and metallic (cluster) components: $YBa_2Cu_3O_{6+x} \Rightarrow (1 - C_m)YBa_2Cu_3O_{6.0} + C_mYBa_2Cu_3O_{7-\delta}$, were C_m is the metallic phase concentration.

The samples were prepared by a pulsed laser deposition technique [9] using an excimer laser (KrF, τ = 25 ns, 1.5–2.5 J/cm^2) and $YBa_2Cu_3O_{7-\delta}$ targets. The films were deposited onto $LaAlO_3$ substrates heated to T_s = 780°C at an oxygen pressure of ~280 mTorr. After deposition, the films were annealed in vacuum (0.1–1 mTorr) for 15–30 min at 500°C. Then the samples were irradiated using the same excimer laser operating at an energy density of Φ = 0.1 J/cm^2, which is 3.5–4 times lower as compared to the YBaCuO sputtering threshold [10].

Figure 1 (curve *1*) shows a typical optical transmission spectrum of an as-deposited film. Not discussing spectral features observed in the shortwave region, we note the absence of absorption related to the presence of free charge carriers (at $\hbar\omega < 1.2$ eV), which is always found in the spectra of superconducting YBaCuO layers (see Fig. 1, curve *2*) [9]. This feature appears only after laser irradiation (Fig. 1, curve *3*), favoring the phase separation and the development of inhomogeneities [7]. At the same time, the laser processing leads to an increase in the overall transparency in the spectral range studied and to a growth in the sample resistance (by a factor of 10–20 at T = 300 K).

Development of a system of clusters possessing metallic conductivity as a result of laser irradiation was confirmed by X-ray diffraction measurements. In the initial film, the main reflections in the X-ray diffraction patterns (Fig. 2a) correspond to planes of the (11*l*) family characteristic of the dielectric state of YBaCuO [9]. The diffraction pattern observed after laser irradiation shows evidence of the development of a system of clus-

ters possessing metallic conductivity: this system predominantly involves a family of planes of the (00*l*) type (Fig. 2b). The laser-irradiated sample exhibits eight refections instead of three (manifested by diffuse maxima above the background), corresponding to the (001) planes responsible for the conductivity and high-temperature superconductivity. Judging by the (005) and (006) reflections, the volume fraction of the clusters possessing metallic conductivity increases from 1.6 to 2.4%; the average size (R_{av}) of the clusters of this type increases from 8 to 12 nm.

The development of the system of metallic clusters leads to a disorder in the sample structure. This is accompanied by smearing of the density of states (DOS), which is clearly pronounced in the behavior of the $(1/t)\partial t/\partial(\hbar\omega)$ function. By definition, the optical transmission coefficient $t = I/I_0 = f(R)\exp(-\alpha d)$, where I_0 and I are the incident and transmitted radiation intensities, respectively, $f(R)$ is a function depending on the reflection coefficient R (in the simplest case, $f(R) = 1 - R$), α is the absorption coefficient, and d is the sample film thickness. Assuming that $f(R)$ is a slowly varying function as compared to α, the $(1/t)\partial t/\partial(\hbar\omega)$ function can be expressed as

$$(1/t)\partial t/\partial(\hbar\omega) \cong -d\partial\alpha/\partial(\hbar\omega), \qquad (1)$$

where the absorption coefficient α is directly related to the density of states involved in the optical transitions [11]. As can be seen from Fig. 1, the amplitude of variation of the $(1/t)\partial t/\partial(\hbar\omega)$ function, which characterizes gradients in the DOS variation, significantly decreases as a result of the laser irradiation. As can be readily shown in the classical approximation using the well-known relationships [1, 7, 9, 11], the region of absorption due to the free charge carriers obeys the relationship

$$(1/t)\partial t/\partial(\hbar\omega) \sim K_1 + K_2 dpC_m(\hbar\omega)^{-3}, \qquad (2)$$

where K_1 and K_2 are constants and p is the hole concentration. Using this approximation, we established that the metal phase concentration C_m in the initial film was below 0.5%; after the irradiation, this value increased to C_m = 1.1%. Considering the clusters as three-dimensional formations, the distance between quantum dots can be estimated by the formula [12, 13]

$$l = R_{av}(C_m^{-1/3} - 1). \qquad (3)$$

For C_m = 0.011 and an average cluster size of R_{av} = 8–12 nm, the spacing between these dots is l = 28–42 nm. The probability of tunneling between clusters in this case is insignificant [14–16]. The low-temperature resistances of these samples were too large for the measurements aimed at observing the $\rho(T)$ = const behavior (the measurements could be only performed for $T > 50$ K).

In samples with a greater oxygen content, the average conductivity increases (in our case, approximately

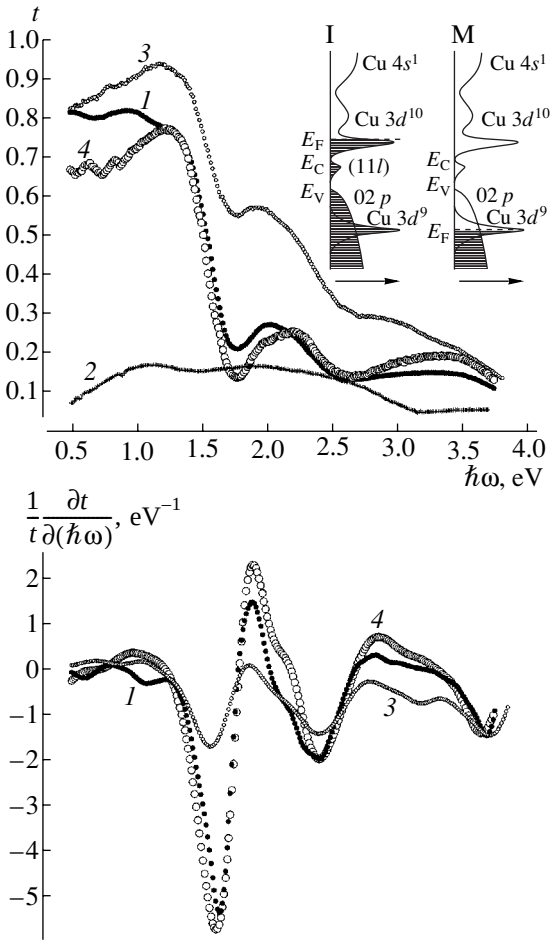

Fig. 1. Optical transmission spectra $t = t(\hbar\omega)$ and the derivative functions $(1/t)\partial t/\partial(\hbar\omega)$ of YBaCuO films with various structures: (*1*) tetragonal film with a low oxygen content; (*2*) epitaxial orthorhombic film with an with T_{co} = 90.6 K; (*3*) tetragonal film after laser irradiation (20 pulses, 0.1 J/cm^2); (*4*) tetragonal film with increased oxygen content. The inset shows DOS model for (I) dielectric matrix and (M) metal clusters in the films studied.

ten times at T = 300 K) and the spectral features related to the absorption due to free charge carriers can be observed even in the initial films (Fig. 1, curve *4*). Here, the metallic phase content is estimated at C_m = 3.9% (by the X-ray data, 3.1%), which corresponds to an almost fourfold growth, while the optical transmission t is lower than that of the less doped material almost in the entire spectral interval studied. At the same time, the amplitudes of variation of the $(1/t)\partial t/\partial(\hbar\omega)$ function are virtually the same (see Fig. 1). The spectral features are indicative of the presence of an edge maximum of states in the conduction band (see the DOS models in the inset to Fig. 1). A minimum observed for the energy of ~3.4 eV corresponds to a pseudogap between Cu3d^{10} and Cu4s^1. Further increase in the DOS level and a decrease in the optical transmission with increasing $\hbar\omega$

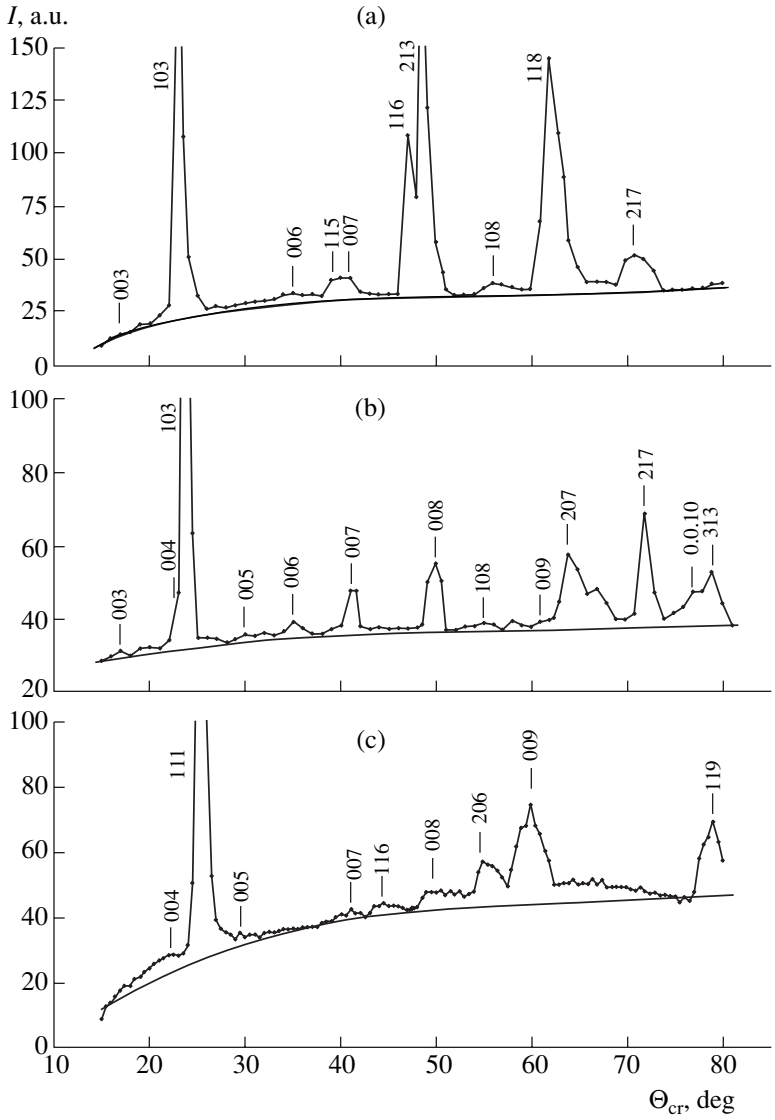

Fig. 2. X-ray diffraction patterns for the YBaCuO films studied.

(for $\hbar\omega > 3.4$ eV) are probably related to a contribution of the Cu4s^1 states to the optical absorption.

According to the X-ray diffraction data, the average size of the (00l) clusters decreases as compared to that in the previous case and amounts to about 6 nm, while the number of clusters grows several fold. The number of types of the planes belonging to the (00l) family increases to five (Fig. 2c) instead of three. Estimates of the cluster spacing yield l = 11–12 nm for C_m = 3.9% and R_{av} = 6 nm. The exponential growth in the probability of tunneling with decreasing l leads to a decrease in the low-temperature resistance, which allows the $\rho(T) \cong$ const behavior to be observed at $T < 20$ K (Fig. 3).

Although a theory of this effect has still not been developed, we may suggest (judging by the data presented in Fig. 3) that T_{crit} is related to a transition from the clusters with a quasi-continuous spectrum to quantum dots. At $T < T_{crit}$ (in Fig. 3, T_{crit} = 20 K), the resistance of a sample is determined by tunneling of the charge carriers over the system of quantum dots, so that $\rho(T) \cong$ const. Using the value $T_{crit} = 1.7 \times 10^{-3}$ eV and taking into account the separation of the quantum confinement levels Δ, we can estimate the cluster size R_{av} from the relationship

$$KT_{crit} \cong \Delta = [R_{av}^3 N(E_F)]^{-1} \cong [R_{av}^3 p/E_F]^{-1}, \qquad (4)$$

where E_F is the Fermi energy and p is the hole concentration. For $p = 1 \times 10^{22}$ cm^{-3}, this formula yields R_{av} = 4 nm; this is somewhat greater than the average cluster size in the amorphous YBaCuO films with T_{crit} = 160–240 K [1]. However, since the space-charge layer thickness at the cluster surface (i.e., the layer depleted of holes) $w \sim (1/p)^{1/2}$ is on the order of 1 nm [1], the

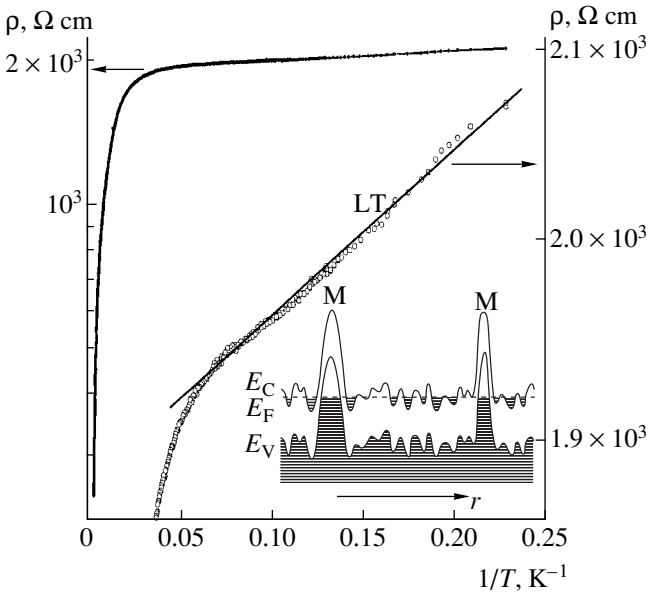

Fig. 3. The temperature dependence of resistance of an YBaCuO film with increased oxygen content. The inset shows an energy band diagram of a dielectric $YBa_2Cu_3O_{6+x}$ film with metallic clusters: E_C, conduction band edge; E_V, valence band edge; *M*, clusters possessing metallic (hole-type) conductivity.

obtained R_{av} value should be increased to 6 nm in agreement with the X-ray diffraction data. Among the total of two dozen free holes, about two-thirds fall within the depleted layer. In connection with this, a decrease in the cluster size to 3–4 nm (a value characteristic of the amorphous films [1, 7]) can lead to catastrophic consequences for the free hole concentration in the clusters, which explains the large difference in T_{crit} between the samples of two types. A small cluster size (comparable to a doubled *w* value) in the amorphous films leads to a considerable decrease in the concentration of holes in the near-surface layers of clusters, so that the quantum-confinement effects in the optical spectra are manifested even at room temperature [1].

Despite the approximate relationship $\rho(T) \cong$ const, the data in Fig. 3 indicate that in contrast to the amorphous films, a weak temperature dependence of ρ is retained even at low temperatures. This is clearly manifested in the LT curve showing the ρ versus *T* plot at $T < 30$ K on a greater scale. In the temperature range from 300 to 20 K, the local activation energies conventionally determined as $\delta\varepsilon = \partial \ln n\rho / \partial(kT^{-1})$ [17] vary from 0.35 to 4×10^{-4} eV. In the interval 4.2 K < *T* < 13 K, this quantity acquires an extremely low and very strange value of $\delta\varepsilon = 9.6 \times 10^{-5}$ eV, which is four times smaller than the value of *kT* at 4.2 K and 12 times smaller than *kT* at 13 K. We believe that the most probable reason for this behavior is the presence of "tails" of the electric conductivity mechanisms related to the thermal activation, the operation of which at low temperatures is shunted by conductivity over a system of tunneling-connected quantum dots. It should be noted that the value $\delta\varepsilon = 9.6 \times 10^{-5}$ eV corresponds to an electromagnetic quantum energy $\hbar\omega$ belonging to the microwave region (centimeter wavelength band, λ = 1.3 cm), which opens new possibilities for the investigation of this phenomenon.

Acknowledgments. This study was partly supported by a grant from the Government of Poland (PBZ-KBN-0.13/T08.19).

REFERENCES

1. V. D. Okunev, Z. A. Samoilenko, V. M. Svistunov, *et al.*, J. Appl. Phys. **85** (10), 7282 (1999).
2. V. G. Prokhorov, G. G. Kaminskiĭ, V. S. Flis, and Young Pak Lee, Fiz. Nizk. Temp. **25** (10), 1060 (1999) [Low Temp. Phys. **25**, 792 (1999)].
3. V. D. Okunev, N. N. Pafomov, A. Abaleshev, *et al.*, Pis'ma Zh. Tekh. Fiz. **26** (20), 20 (2000) [Tech. Phys. Lett. **26**, 903 (2000)].
4. Zh. I. Alferov, Fiz. Tekh. Poluprovodn. (St. Petersburg) **32** (1), 3 (1998) [Semiconductors **32**, 1 (1998)].
5. N. N. Ledentsov, V. M. Ustinov, V. A. Shchukin, *et al.*, Fiz. Tekh. Poluprovodn. (St. Petersburg) **32** (4), 385 (1998) [Semiconductors **32**, 343 (1998)].
6. B. M. Smirnov, Usp. Fiz. Nauk **170** (5), 495 (2000).
7. V. D. Okunev, Z. A. Samoilenko, A. Abal'oshev, *et al.*, Phys. Rev. B **62**, 696 (2000).
8. G. P. Shveĭkin, V. A. Gubanov, A. A. Fotiev, G. V. Bazuev, and A. A. Evdokimov, *Electronic Structure and Physicochemical Properties of High Temperature Superconductors* (Nauka, Moscow, 1990).
9. V. D. Okunev, Z. A. Samoilenko, A. Abal'oshev, *et al.*, Appl. Phys. Lett. **75** (13), 1949 (1999).
10. R. K. Singh and J. Narayan, Phys. Rev. B **41** (13), 8843 (1990).
11. R. A. Smith, *Semiconductors* (Cambridge Univ. Press, Cambridge, 1978; Mir, Moscow, 1982).
12. V. D. Okunev, N. N. Pafomov, V. M. Svistunov, *et al.*, Physica C (Amsterdam) **262** (1/2), 75 (1996).
13. V. D. Okunev and T. A. D'yachenko, Fiz. Nizk. Temp. **22** (11), 1252 (1996) [Low Temp. Phys. **22**, 953 (1996)].
14. Y. Xu, A. Matsuda, and M. R. Beasley, Phys. Rev. B **42** (2), 1492 (1990).
15. Y. Xu, D. Ephron, and M. R. Beasley, Phys. Rev. B **52** (4), 2843 (1995).
16. J. Yoshida, T. Nagano, and T. Hashimoto, J. Low Temp. Phys. **106** (3/4), 327 (1997).
17. V. D. Okunev and N. N. Pafomov, Zh. Éksp. Teor. Fiz. **116** (1), 276 (1999) [JETP **89**, 151 (1999)].

Translated by P. Pozdeev

Technical Physics Letters, Vol. 28, No. 1, 2002, pp. 48–49. Translated from Pis'ma v Zhurnal Tekhnicheskoĭ Fiziki, Vol. 28, No. 2, 2002, pp. 21–24.

Special Features of the Periodic-Pulse-Train Laser Radiation Confinement in Doped Gallium Arsenide and Zinc Selenide

O. P. Mikheeva, A. I. Sidorov, A. S. Khaĭkina, and E. V. Chuguevets

Institute of Laser Physics, St. Petersburg, Russia

Received August 7, 2001

Abstract—Experimental data on the pulsed laser radiation confinement in compensated GaAs and ZnSe with deep impurity levels are reported for the laser wavelength $\lambda = 1.55$ μm and a pulse repetition frequency of up to 100 kHz. It is demonstrated that an increase in the pulse repetition rate is accompanied by a decrease in the energy confinement threshold and by an increase in the radiation attenuation coefficient. These effects are explained by the accumulation of nonequilibrium charge carriers related to a dependence of the recombination time constant on the concentration of free impurity centers. © *2002 MAIK "Nauka/Interperiodica".*

The phenomenon of laser radiation confinement due to self-defocusing under the conditions of two-photon [1–3] and one-photon [4] absorption by impurity centers in semiconductors is of interest for creating laser radiation attenuators protecting photodetectors against overloading and radiation damage. Using the phenomenon of optical absorption by deep impurity levels, it is possible to significantly reduce the energy confinement threshold as compared to analogous devices employing the two-photon absorption.

The purpose of this study was to determine the effects of the pulse repetition rate on the energy confinement threshold and the attenuation coefficient, which are the main characteristics of attenuators based on doped semiconductors.

The experiments were performed on 5-mm-thick samples of compensated GaAs with a resistivity of 1 MΩ cm and 7-mm-thick samples of ZnSe containing oxygen impurity. The optical confinement scheme (see the inset in Fig. 1) comprised two confocal glass lenses with the focal lengths $F = 8.5$ and 1.5 cm and a diaphragm (transmitting 95% of the incident radiation) situated at a distance of 7 cm from the second lens. The sample semiconductor plate was placed at a distance of 1.5 mm from the common focal plane of both lenses. The source of radiation was a single-mode (TEM_{00}) pulsed erbium laser with $\lambda = 1.55$ μm and a laser pulse width of 5.5 ns. The laser beam diameter at the attenuator input was 7 mm.

Figure 1 shows initial portions of the plots of radiation energy at the confinement system output versus input energy for (a) GaAs and (b) ZnSe measured in a single-pulse ($f = 0$) and periodic-pulse-train ($f = 20$ and 100 kHz) laser operation regime. As can be seen, the transition from single-pulse to periodic-pulsed-train regime and the increase in the pulse repetition rate lead to a decrease in the energy confinement threshold and an increase in the attenuation coefficient in the confinement range. In particular, the energy confinement

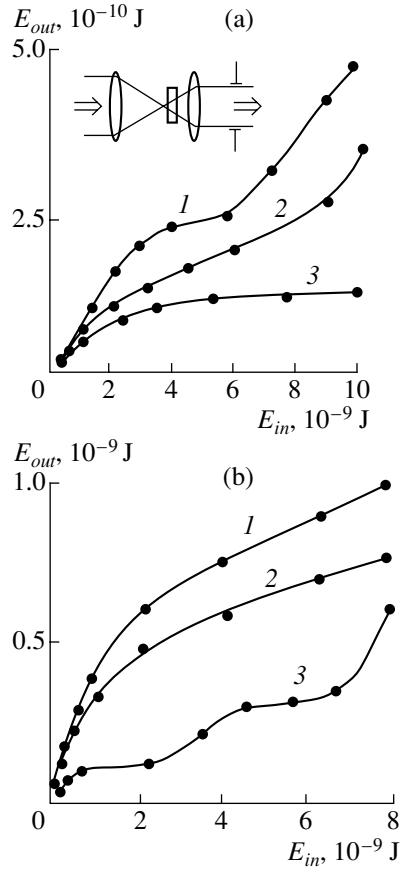

Fig. 1. The plots of energy output versus input illustrating the pulsed laser radiation confinement in (a) GaAs and (b) ZnSe for a pulse repetition rate of $f = 0$ (*1*), 20 (*2*), and 100 kHz (*3*). The inset shows the optical confinement scheme.

1063-7850/02/2801-0048$22.00

threshold for GaAs drops from $E_{thr} \approx 300$ pJ at $f = 0$ to $E_{thr} \approx 120$ pJ at $f = 100$ kHz. The attenuation coefficient for $E_{in} = 5$ nJ shows an approximately twofold increase. For ZnSe under the same conditions, the E_{thr} value decreases from 1000 to ~500pJ and the attenuation coefficient increases by a factor of three.

The reason for these effects is the dependence of the recombination time constant τ on the concentration of free impurity centers (see, e.,g., [5]): $\tau = (VSN^*)^{-1}$, where V is the nonequilibrium carrier velocity, S is the cross section of recombination on the impurity center, and N^* is the concentration of free impurity centers. If a semiconductor features only the impurity recombination, the N^* value equals the concentration of nonequilibrium charge carriers $N^* = N$. Then the equation of continuity in the interaction region after termination of the radiation pulse takes the following form (with neglect of the carrier diffusion):

$$\frac{dN}{dt} + N^2VS = 0.$$

A solution to this equation is as follows:

$$\frac{N(t)}{N_0} = (1 + N_0VSt)^{-1},$$

where N_0 is the nonequilibrium carrier concentration immediately upon termination of the laser action.

Figure 2 shows the time variation of the relative concentration of nonequilibrium charge carriers in GaAs upon termination of the laser action for $N_0 = 10^{12}$ and 10^{14} cm^{-3}. As can be seen, there is a sharp initial drop followed by a rather long sloped region. For this reason, the periodic-pulse-train regime is accompanied by pulse to pulse accumulation of the nonequilibrium carrier concentration in the region of laser action. This results in the formation of a dynamic negative lens related to a gradient of the nonequilibrium carrier concentration, which accounts for the radiation self-defocusing. For $f > 0$, this lens is formed at a lower laser pulse energy as compared to that in the single-pulse mode. This is manifested by a decrease in the energy confinement threshold. For $E > E_{thr}$, the charge carrier accumulation in the periodic-pulse-train mode ($f > 0$) leads to an increase in the nonequilibrium carrier concentration as compared to that in the single-pulse mode. This results in an increase of the degree of radiation self-defocusing and, hence, of the radiation attenuation coefficient.

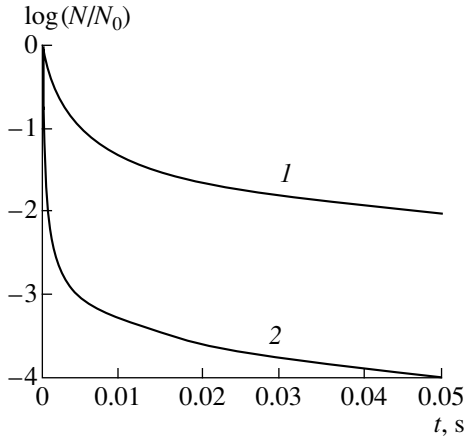

Fig. 2. Time variation of the relative concentration of nonequilibrium carriers in the region of laser action after termination of the laser pulse action for $N_0 = 10^{12}$ (*1*) and 10^{14} cm^{-3} (*2*).

Acknowledgments. This study was supported by the International Scientific-Technological Center, grant no. 1454.

REFERENCES

1. T. F. Bogges, A. I. Smirl, S. Moss, *et al.*, IEEE J. Quantum Electron. **QE-21** (5), 488 (1985).
2. D. J. Hogan, E. W. Van Stryland, M. J. Soileau, *et al.*, J. Opt. Soc. Am. A **3** (13), 105 (1986).
3. E. W. Van Stryland, Y. Y. Wu, D. J. Hagan, *et al.*, J. Opt. Soc. Am. B **5** (9), 1980 (1988).
4. I. V. Bagrov, A. P. Zhevlakov, and A. I. Sidorov, Pis'ma Zh. Tekh. Fiz. **27** (10), 26 (2001) [Tech. Phys. Lett. **27**, 406 (2001)].
5. V. S. Vavilov, *Effects of Radiation on Semiconductors* (Fizmatgiz, Moscow, 1963; Consultants Bureau, New York, 1965).

Translated by P. Pozdeev

Technical Physics Letters, Vol. 28, No. 1, 2002, pp. 50–51. Translated from Pis'ma v Zhurnal Tekhnicheskoĭ Fiziki, Vol. 28, No. 2, 2002, pp. 25–29.

Surface Acoustic Wave Gas Sensor of the Sorption Type Sensitive to the Thermal Properties of Gases

R. G. Kryshtal, A. P. Kundin, A. V. Medved, and V. V. Shemet

Fryazino Branch, Institute of Radio Engineering and Electronics, Russian Academy of Sciences, Fryazino, Moscow oblast, Russia

e-mail: avm@ms.ire.rssi.ru

Received September 3, 2001

Abstract—The basic principles of a new surface acoustic wave (SAW) gas sensor are described. Being essentially a sensor of the sorption type, the proposed device possesses certain features of the thermometric SAW sensors and is not only sensitive to the vapors of volatile substances, but capable of detecting gases by their thermal properties as well. In contrast to the known thermometric SAW sensors, the proposed sensor is characterized by high temperature stability and fast response. A variant of the sensor based on a $LiNbO_3$ SAW delay line is described and some results of the test for detecting propane-butane mixtures are presented. *© 2002 MAIK "Nauka/Interperiodica".*

As is known, devices implementing surface acoustic waves (SAWs) are sensitive to the state of a SAW substrate surface along which the waves are propagating. The adsorption of molecules from the gas phase on the waveguide surface modifies the SAW propagation parameters, which is reflected by changes in the output signal. This principle is employed in SAW gas sensors of the sorption type. In order to provide for a selectivity with respect to the adsorbate, the SAW-guiding surface is coated with a special material exhibiting increased absorption capacity with respect to compounds of one or another class. These gas sensors find increasing application, for example, in the sensor arrays of modern gas analyzers of the "electronic nose" type [1].

However, the SAW sensors free of the selective sensitivity coatings offer better reproducibility and stability characteristics [2]. Usually not possessing selectivity, these devices are capable of detecting only the vapors of volatile substances adsorbed on the working surface. Nevertheless, such sensors are widely used in instruments based on portable chromatographs for the detection and recognition of volatile compounds [3]. Modern chromatographs have become universal devices, which requires that the SAW sensors would detect not only the vapors of volatile substances, but the stable and burning gases as well.

Below we describe the basic principles of a new SAW gas sensor of the sorption type, which also possesses certain features of thermometric SAW sensors [4]. As a result, the proposed device is capable of detecting both the vapors of volatile substances and gases by their thermal properties. In contrast to the known thermometric SAW sensors, the new sensor is characterized by high thermal stability and fast response. A variant of the sensor based on a 128° *Y–X* $LiNbO_3$ SAW delay line is described and some results of the test for detecting propane-butane gas mixtures for household purposes are presented.

The temperature stabilization of modern SAW sensors of the sorption type is provided by using Peltier's thermoelectric elements (TEEs) [3, 5]. In these devices, the sensitive element (SAW delay line or resonator) is mounted immediately on the TEE working surface. Figure 1 shows the results of measurements of the output signal phase in a sensor based on a 128° *Y–X* $LiNbO_3$ SAW delay line operating at the central frequency of 486 MHz [5]. The measurements were performed for a preset TEE working surface temperature change of 1 K at a maximum rate possible with the temperature stabilization system employed. As can be seen, the SAW substrate temperature is fully established during a time period of ~5 s, the most rapid variation taking place within the first second after the TEE temperature

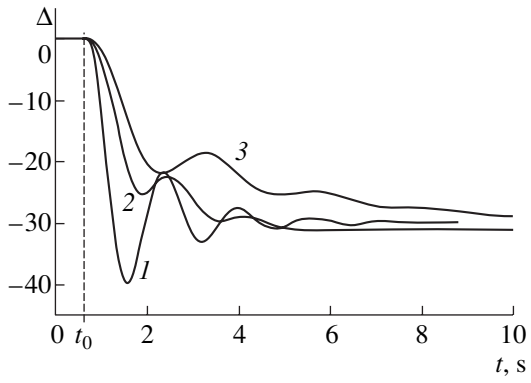

Fig. 1. Time variation of the output signal phase in response to a 1 K change in the TEE working surface temperature (from 57.3 to 58.3°C, t_0 is the onset moment of the temperature change) for a SAW sensor with different numbers of glass spacers between the TEE surface and SAW substrate: (*1*) no spacers; (*2*) one spacer; (*3*) two spacers.

1063-7850/02/2801-0050$22.00 © 2002 MAIK "Nauka/Interperiodica"

switching. We may suggest that the sensor temperature would return at approximately the same rate to the initial level upon any external thermal action. This action can be produced by the analyzed gas portion injected to the working chamber, the thermal properties of which (thermal conductivity and heat capacity) may differ from those of the previously flowing gas (gas-carrier).

At a reasonable velocity of the gas flow through the working chamber and a reasonable temperature difference between the SAW substrate and a gas sample, the external action virtually does not affect the SAW substrate temperature because the thermal stabilization system rapidly compensates for these changes. Indeed, the experiments on detecting a propane–butane mixture showed that a change in the sensor response (output signal phase) did not exceed 0.5 deg.

The detection of gases by their thermal properties requires a certain delay in operation of the temperature stabilization system. Such a delay can be realized, in particular, by retarding the heat flux between the TEE working surface and SAW substrate. For this purpose, we used thin (0.25 mm) glass plates glued to the TEE surface, SAW substrate, and to each other by a heat-conducting paste. The results of measurements presented in Fig. 1 showed that a 1 K change in the TEE working surface temperature is followed by a slower process of attaining the new equilibrium SAW substrate temperature. The greater the number of glass spacers between the TEE working surface and the SAW substrate, the slower the temperature relaxation. The SAW sensor with glass spacers was tested for detecting a propane–butane mixture. In these experiments, the working chamber (with a volume of ~2 cm^3) accommodating the SAW sensor and TEE element, as well as a metal capillary supplying the gas, were placed in a thermostat at a constant temperature of 30 ± 1°C maintained with a precision of not less than ±0.1°C. The chamber was purged with a gas-carrier (nitrogen) at a constant rate of 70 cm^3/min (±1%). A gas sample with a volume of 4 cm^3 was introduced into the gas-carrier by a conventional method (using a six-thread control dosage valve) employed in the gas chromatography.

Figure 2 illustrates the response of a SAW sensor with glass plates to the injection of a propane-butane mixture to the working chamber at two temperatures of the SAW substrate. The output signal phase change was positive (SAW substrate cooling) when the initial SAW substrate temperature was higher than that of the gas sample (i.e., of the chamber walls) and the change was negative (SAW substrate heating) in the opposite case. An analysis showed that the main contribution to the sensor response is probably related to a difference between the heat capacities of nitrogen (1.46 kJ/(kg K)) and the propane–butane mixture (1.04 kJ/(kg K)), rather than the difference between thermal conductivities (2.4×10^{-4} W/(m K) for nitrogen versus 1.43×10^{-4} W/(m K) for the gas mixture). The response of a SAW sensor (with a single glass spacer) to a mixture of 5 vol % of propane–butane and 95 vol % of nitrogen at a flow rate of 70 cm^3/min, a SAW substrate temperature of 58°C, and a gas temperature of 30°C was 2.5 deg, which falls within a reliably measurable range (in our experiments, a minimum reliably measured phase change was 0.2 deg).

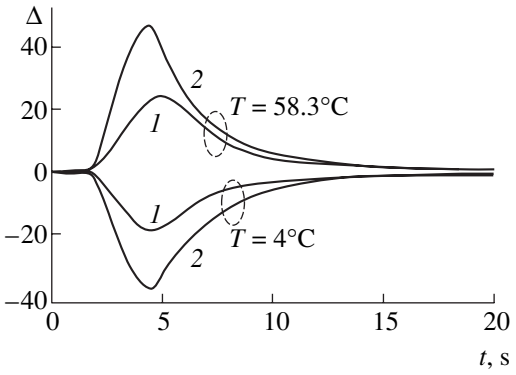

Fig. 2. The output signal phase variation in a SAW sensor with (*1*) one and (*2*) two glass spacers between TEE surface and SAW substrate in response to injection of a propane-butane mixture into the working chamber at a SAW substrate temperature of 58.3°C and 4°C (maintained to within ±0.003°C for 10 min). The gas (and chamber wall) temperature was 30°C.

When a SAW sensor with glass spacers between the TEE working surface and SAW substrate was tested for detecting the vapors of a series of alcohols and water at a SAW substrate temperature below the gas sample temperature, the response level was virtually the same as that reported previously [5], where an analogous device was employed with a "usual" temperature stabilization system.

Thus, we have described for the first time the basic principles of a SAW gas sensor capable of detecting both the vapors of volatile substances and the stable and burning gases. The sensor offers high temperature stability and fast response inherent in the SAW sensors of the sorption type. Further investigations aimed at the optimization of some design parameters and operation modes would provide for good prospects in the practical use of the new gas sensors.

REFERENCES

1. H. T. Nagle, S. S. Schiffman, and R. Gutiérrez-Osuna, IEEE Spectr. **35** (9), 22 (1998).
2. G. W. Watson, W. Horton, and E. J. Staples, in *Proceedings of the Ultrasonic Symposium, 1991*, p. 305.
3. E. J. Staples, in *Proceedings of the IEEE Ultrasonic Symposium, 1999*, p. 417.
4. V. I. Anisimkin, S. A. Maksimov, M. Penza, and L. Vasanelli, Zh. Tekh. Fiz. **67** (5), 119 (1997) [Tech. Phys. **42**, 564 (1997)].
5. Yu. V. Gulyaev, V. E. Zemlyakov, R. G. Kryshtal', *et al.*, Akust. Zh. **47** (1), 52 (2001) [Acoust. Phys. **47**, 42 (2001)].

Translated by P. Pozdeev

Technical Physics Letters, Vol. 28, No. 1, 2002, pp. 52–54. Translated from Pis'ma v Zhurnal Tekhnicheskoĭ Fiziki, Vol. 28, No. 2, 2002, pp. 30–36.

A Nonlinear Mechanism of the Energy Transfer by a Perturbation Front in the Course of Local High-Energy Loading

S. G. Psakh'e, K. P. Zol'nikov, and I. A. Kostin

Institute of Strength Physics and Materials Science, Siberian Division, Russian Academy of Sciences, Tomsk, 634055 Russia

e-mail: psakhie@yahoo.com

Received August 28, 2001

Abstract—The features of perturbation propagation in a copper crystal grain under local high-energy loading conditions were studied. The process was studied by method of molecular dynamics using multiparticle model potentials calculated within the framework of the embedded atom approximation. It is shown that a nonlinear solitary pulse is formed in the crystal, which is capable (in contrast to the case of a linear perturbation) of transferring the energy at a high density over relatively large distances. The energy transfer range depends both on the area and on the rate of local loading. *© 2002 MAIK "Nauka/Interperiodica".*

A high-energy action upon a material may give rise to the formation of waves of various nature. In particular, the presence of nonlinear interatomic interactions can result in the generation and propagation of nonlinear (soliton-like) waves. Special features of the propagation of such waves were originally studied in application to one-dimensional (1D) chains and then in systems of higher dimensionality [1–5]. The calculations showed that materials possessing ideal structure may feature propagation of nonlinear waves practically without energy dissipation. It should be noted that the 2D and 3D systems were modeled using periodic boundary conditions; that is, the edge effects were ignored. For this reason, questions concerning the effect of a local character of loading on the features of generation and propagation of nonlinear pulses still remain unanswered.

In this context, we have studied the propagation of perturbations generated in a crystal grain as a result of a local high-energy action upon the free sample surface.

The problem was solved by method of molecular dynamics using multiparticle model potentials calculated within the framework of the embedded atom approximation [6, 7]. The local high-energy action was modeled by applying a directed pulse to a certain near-surface region by analogy with a method described elsewhere [8, 9]. The calculations were performed for the copper crystals containing 16000, 32000, 50000, or 75000 atoms in the form of a parallelepiped with the mutually perpendicular edges parallel to the crystallographic directions [100], [010], and [001] (Fig. 1a). The periodic boundary conditions were modeled in the [001] and [010] directions, while the free crystal surfaces had the [100] orientation. The loaded area had a rectangular shape (see the scheme in Fig. 1a). Atoms occurring within this region of the free surface were imparted the initial velocities varied from 3000 to 4000 m/s.

The results of the model calculations showed that the local loading of the free sample surface leads to the formation of a solitary compression pulse propagating in the crystal. The distribution of atomic velocities in such a pulse at two different time instants is illustrated in Figs. 1b and 1c for a crystal loaded at 3000 m/s. As can be seen, the solitary pulse propagation upon a local sample loading exhibits a pronounced nonlinear character, with a high energy density retained inside the pulse over a sufficiently long period of time (sometimes up to the moment of reaching a rear open surface of the modeled crystal grain).

Using the results, we have compared a change in the energy density on the perturbation front within the framework of a linear approximation (spherical front) and in the model (nonlinear solitary wave) employed in this study. The loading amplitude was 3000 m/s. The results of the comparative analysis are presented in Fig. 2, showing the energy density profiles in relative units (with a maximum virtually equal to the initial energy density on the perturbation front). As can be seen from these data, a high energy density in the pulse front may be retained up to sufficiently large penetration depths, although the size of the region featuring the high energy density decreases in the course of the pulse propagation (cf. Figs. 1b and 1c).

An analysis of the results showed that the penetration depth of a pulse retaining the high initial energy density level depends on the size of the loaded region. The data presented in Fig. 3a indicate that an increase in the area of loading results in the high initial energy

1063-7850/02/2801-0052$22.00

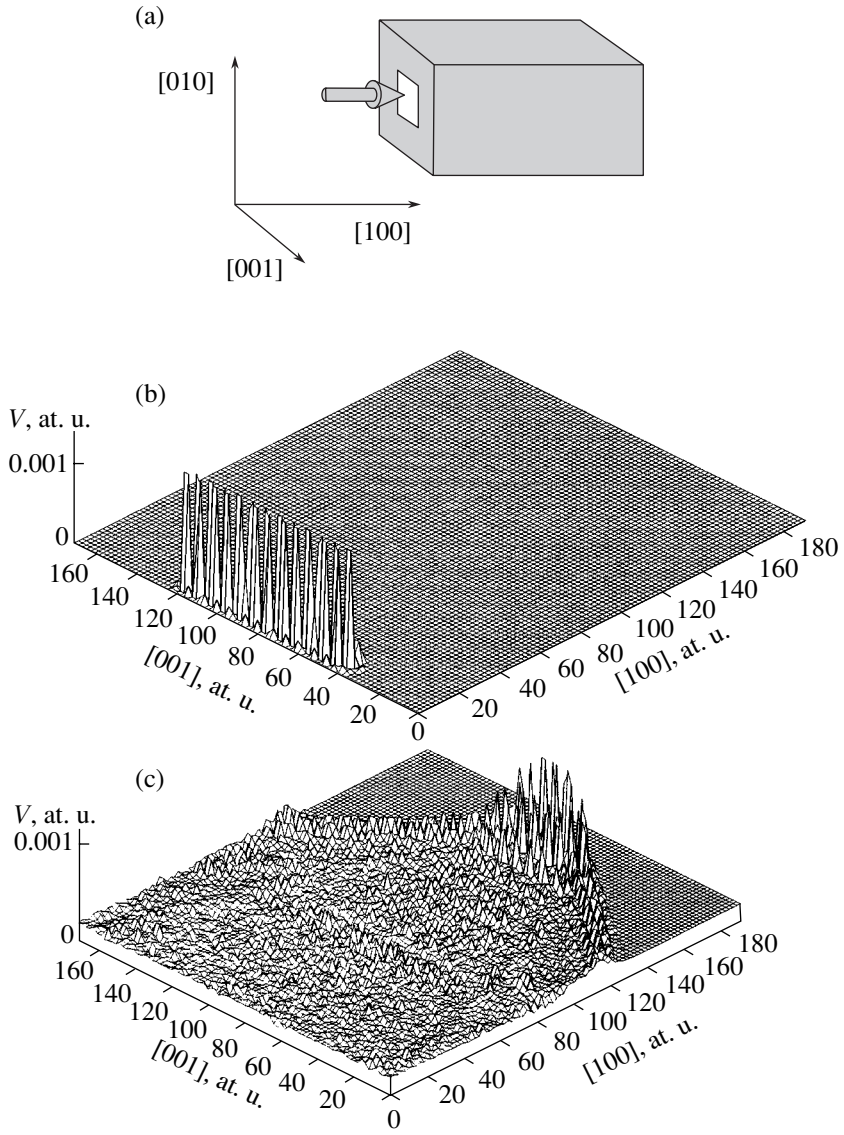

Fig. 1. Schematic diagrams showing (a) the scheme of loading and (b, c) the distributions of atomic velocities in a solitary pulse on the 10th and 450th time step, respectively.

density being retained in the pulse propagating to greater depths. It was also naturally expected that stability of the nonlinear pulse and the depth to which the high initial energy density is transferred must be determined by the intensity of the local loading. In order to study this relationship, we applied various loads (from 3000 to 4000 m/s) to the same area. The results of these model experiments are presented in Fig. 3b.

Thus, a nonlinear pulse propagating in a crystal grain loses energy through a boundary with the unperturbed part of the grain. As the nonlinear perturbation propagates in the crystal, the size of this interaction area decreases together with the size of the region of high energy density.

Finite dimensions of a nonlinear pulse and the features of energy dissipation from this pulse produce a certain effect on the character of the soliton-like wave interaction with extended structural defects, in particular, with the free surface. It was recently demonstrated [10–12] that the escape of an infinite (in the case of periodic boundary conditions) soliton-like wave on the free surface may result in detachment of the surface atomic planes, provided that the kinetic energy at the wave front exceeds a certain critical level E_c. In copper, the critical energy per atom is about 2.2 eV. For a nonlinear pulse of finite dimensions, the threshold energy level per atom on the wave propagation front, which is necessary for the detachment of atomic planes, will be greater as compared to a value for the infinite wave. This is related to the fact that a greater number of interatomic bonds have to be broken by the surface atoms in the case of a finite pulse. Therefore, the smaller the area of loading, the greater the fraction of boundary atoms

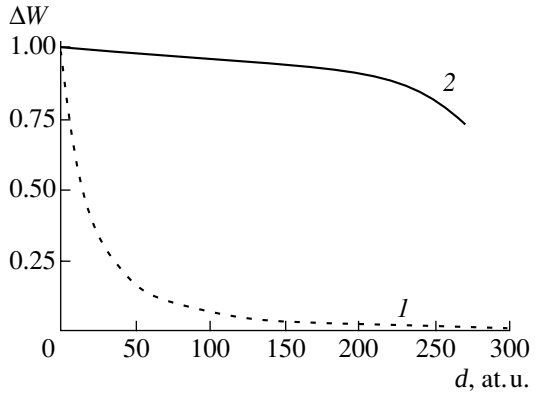

Fig. 2. Energy density (ΔW) versus penetration depth (d) profiles for the pulse propagation studied in the (*1*) linear and (*2*) nonlinear approximations.

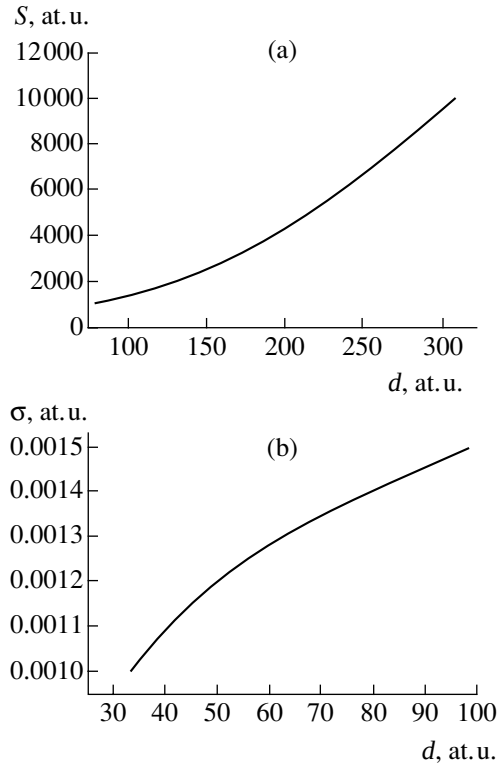

Fig. 3. Plots of the penetration depth d versus (a) loading area S and (b) loading rate σ for a nonlinear pulse propagation.

and the higher the critical energy level. In the computer simulations described above, the ratio of atoms located on the boundary of the loaded area to the total number of atoms in this area changed from 10 to 50%. In the limiting case, when all atoms in the nonlinear pulse emerging at the rear crystal surface will be boundary (i.e., 15 atoms or less), the critical energy will increase by almost 30%.

Thus, we have demonstrated for the first time that a local high-energy loading of a crystal gives rise to nonlinear solitary pulses of finite size. A high energy density is retained at the front of such pulses and can be transferred over sufficiently large distances.

REFERENCES

1. B. L. Holian and G. K. Straub, Phys. Rev. B **18** (4), 1593 (1978).
2. E. A. Dynin, Fiz. Goreniya Vzryva **19** (1), 111 (1983).
3. G. K. Straub, B. L. Holian, and R. G. Petsheck, Phys. Rev. B **19** (8), 4049 (1979).
4. M. Toda, *Theory of Non-Linear Lattices* (Springer-Verlag, Heidelberg, 1981; Mir, Moscow, 1984).
5. S. G. Psakh'e, K. P. Zol'nikov, and S. Yu. Korostelev, Pis'ma Zh. Tekh. Fiz. **21** (13), 1 (1995) [Tech. Phys. Lett. **21**, 489 (1995)].
6. A. V. Berch, A. G. Lipnitskiĭ, and E. V. Chulkov, Poverkhnost, No. 6, 23 (1994).
7. S. V. Ereneev, A. G. Lipnitskii, A. I. Potekaev, and E. V. Chulkov, Phys. Low-Dimens. Struct., No. 3/4, 127 (1997).
8. S. G. Psakh'e, K. P. Zol'nikov, and D. Yu. Saraev, Fiz. Goreniya Vzryva **33** (2), 143 (1997).
9. S. G. Psakh'e, D. Yu. Saraev, and K. P. Zol'nikov, Pis'ma Zh. Tekh. Fiz. **22** (10), 6 (1996) [Tech. Phys. Lett. **22**, 389 (1996)].
10. K. P. Zol'nikov, T. Yu. Uvarov, V. A. Skripnyak, *et al.*, Pis'ma Zh. Tekh. Fiz. **26** (8), 18 (2000) [Tech. Phys. Lett. **26**, 323 (2000)].
11. K. P. Zol'nikov, T. Yu. Uvarov, A. G. Lipnitskiĭ, *et al.*, Fiz. Goreniya Vzryva, No. 5, 126 (2000).
12. S. G. Psakh'e, K. P. Zol'nikov, and T. Yu. Uvarov, Pis'ma Zh. Tekh. Fiz. **26** (19), 6 (2000) [Tech. Phys. Lett. **26**, 851 (2000)].

Translated by P. Pozdeev

Technical Physics Letters, Vol. 28, No. 1, 2002, pp. 55–58. Translated from Pis'ma v Zhurnal Tekhnicheskoĭ Fiziki, Vol. 28, No. 2, 2002, pp. 37–44.

Alternation of the Right- and Left-Handed Helical Vortices Caused by Increased Flow Swirling in a Cylindrical Cavity with Rotating Lids

V. L. Okulov[a,*], J. N. Sørensen[b,], and L. K. Voigt[b]**

[a] *Institute of Thermal Physics, Siberian Division, Russian Academy of Sciences, Novosibirsk, Russia*
** e-mail: okulov@itp.nsc.ru*

[b] *Department of Mechanical Engineering, Technical University of Denmark, DK-2800, Kongens Lyngby, Denmark*
*** e-mail: jns@mek.dtu.dk*

Received August 7, 2001

Abstract—The process of symmetry variation in the helical vortices formed in a flow induced by rotating lids of a cylindrical cavity was studied. The phenomenon of alternation of the right- and left-handed vortices caused by increased flow swirling was observed for the first time and a relationship was established between the formation of a recirculation zone and the appearance of a left-handed vortex structure in the flow. The results are important both for the explanation of the vortex breakdown phenomenon and for the further development of the vortex concept in the theory of turbulence and of the mechanical analogies used for the description of physical fields and particles. © *2002 MAIK "Nauka/Interperiodica".*

Attempts at providing an adequate description of the swirl flows frequently observed in practice encounter numerous difficulties. One of these is the possibility of a spontaneous change in the flow regime, which was reported in many investigations and commonly referred to as the vortex breakdown phenomenon (see, e.g., [1, 2]). An explanation of this phenomenon is based on the possibility that large-scale helical vortices with different symmetries (for the classification see [3]) are formed in the flow. This fact was confirmed by a theoretical analysis of the vortex breakdown phenomenon [4], where it was shown that the swirl flows possessing helical symmetry of the vorticity field may feature both right- and left-handed vortices for the same integral parameters of the main flow.

A difference between the vortex structures with left- and right-handed helical symmetry is characterized in terms of the sign of the twist κ or the pitch l for the component vortex lies: the positive and negative signs correspond to the right- and left-handed vortices, respectively. However, the theory developed in [4, 5] only describes the flows before and after the vortex breakdown rather than show how the helical symmetry of the vorticity field changes in the course of this process. As can be seen from the diagrams in Fig. 1, the continuous transformation from right- to left-handed vortex may proceed in two different ways: the vortex line pitch may vary from positive to negative either via infinity (Fig. 1a) or via zero (Fig. 1b). The first variant will be referred to as the *L*-transition and the second, as the *R*-transition. Note that the vorticity ring formation upon the vortex breakdown via the *R*-transition was repeatedly suggested as a model adequately describing the phenomenon. However, experiments [3] showed evidence only of the *L*-transition for a helical vortex filament generated in a square vortex burner model.

An additional stimulus for this investigation of the character of symmetry variation in the helical vortex structures was provided by development of the vortex concept in the theory of turbulence. The possibility of sudden transitions between mirror-symmetric coherent structures with different twist signs of the vortex lines can provide for an adequate description of a source of chaotic oscillations in open turbulent flows. Another (and rather unexpected) application of the results of such investigations is the development of mechanical

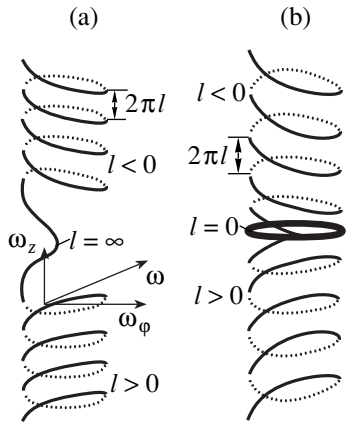

Fig. 1. Possible types of the transition from right- to left-handed vortex structure: (a) via infinite pitch; (b) via zero pitch.

1063-7850/02/2801-0055$22.00 © 2002 MAIK "Nauka/Interperiodica"

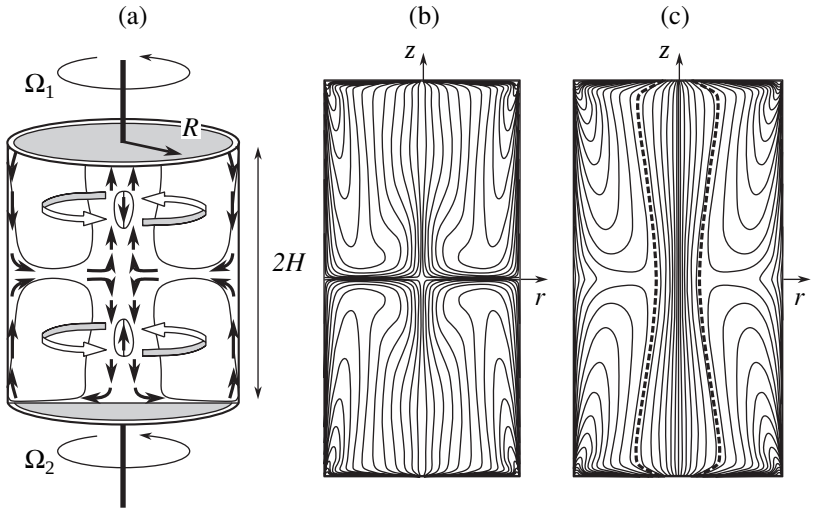

Fig. 2. Schematic diagrams of (a) an axisymmetric flow structure and (b, c) the vortex cross sections for Re = 2000 and $\gamma = 2$ in a cylinder with the lids rotating in (b) the opposite and (c) the same directions.

analogies employed in the description of physical fields and particles [6]. At present, we can only mention the attempts at using the Schrödinger equation for description of the helical perturbations of vortex lines (Hosimoto solitons). The lack of any progress in this direction, neither confirming nor rejecting the proposed analogy, is related primarily to the insufficiently developed theory of helical vortices in application to fluid mechanics. In particular, an important question concerning the character of changes in the symmetry of such vortices is considered below for the first time.

To study this aspect, let us consider an axisymmetric flow of a viscous incompressible fluid in a cylinder with a height of $2H$ and a radius R (Fig. 2a). The cylinder top and bottom lids can be rotated at the constant angular velocities Ω_1 and Ω_2, respectively. The system is characterized by three dimensionless parameters: $\mathrm{Re} = \Omega_1 R^2/\nu$, $h = H/R$, and $\gamma = \Omega_2/\Omega_1$, where ν is the kinematic viscosity of the fluid. The flow will be studied in the cylindrical coordinates to determine the unknown quantities including the tangential velocity component u_φ, the axial vorticity component ω_z, and the current function ψ; the current function isolines determine a cross section of the physical current surfaces in the meridional section [7]. In these terms, the problem reduces to solving the Poisson equation for ψ and two transfer equations for u_φ and ω_z. A solution to this system was obtained by the finite difference method [8].

The transfer equations were approximated by the central difference schemes of the second order of accuracy. The Poisson equation was approximated using a three-point Hermitean representation of derivatives of the current function to within the fourth order of accuracy. This method was previously verified by application to the well-known case of an analogous system with an immobile bottom ($\gamma = 0$) and reproduced well the flow regimes observed in experiment. As for the case of nonzero γ values, some investigations (see [7] and references therein) devoted to the flow topology showed the formation of closed recirculation zones–bubbles featuring opposite directions of motion, the number, size, and position of which can vary.

In the particular case of the top and bottom lids rotating with equal angular velocities ($\gamma = \pm 1$), the system features symmetric flows in the upper and lower parts of the cylinder with a symmetry plane in the central axial cross section ($z = 0$). A physical mechanism responsible for the motion of fluid in such systems was repeatedly considered (Fig. 2a). The driving force is twofold: first, the rotational motion is transferred from the lids to the fluid by the friction forces; second, a rarefaction taking place at the rotation axis gives rise to the axial motion of fluid toward the centers of lids along the cylinder axis and outward from the lids at the periphery. However, this simple scheme is violated as a result of the development of recirculation zones, the appearance of which still remains unexplained. It was only established that the appearance of these zones is not related to the flow instability [9]. In order to explain the formation of the recirculation zones, let us consider the structure of vortices formed in the flow. It should be noted that no analysis of the problem from this standpoint was undertaken previously.

For the lids rotating in the opposite directions ($\gamma = -1$), two mirror symmetric systems of vortex tubes appear in the fluid to form a system of embedded toroids closed on the surface of rotating lids (Fig. 2b). Such a toroidal distribution of vorticity, which is well known in fluid mechanics (vortex ring), induces a purely translational motion at the axis. In this case, the motion is directed from the center of the cylinder toward the rotating lids. Of course, a deviation of the vortex tubes from the purely toroidal shape and a helical character of the

Re	Vortex tube cross section	Vortex line swirling	Axial velocity profile	Current tube cross section
150	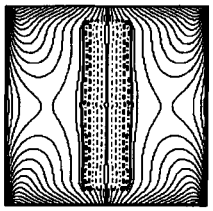	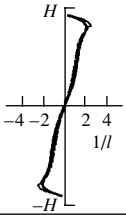	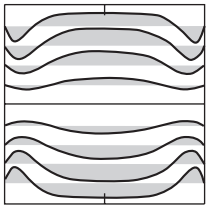	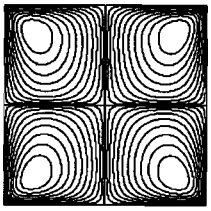
400	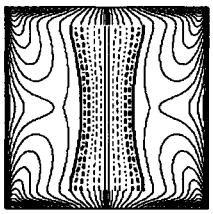	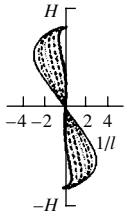	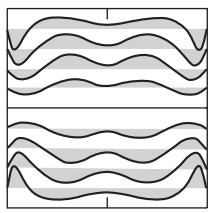	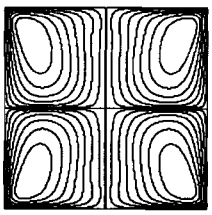
500	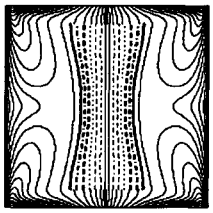	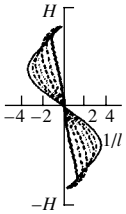	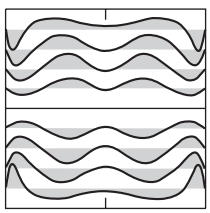	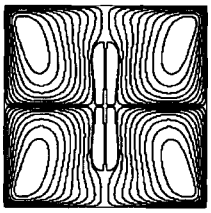
1300	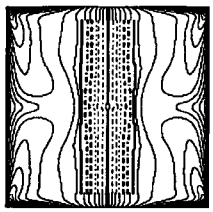	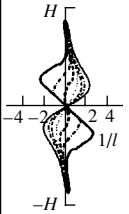	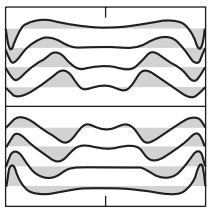	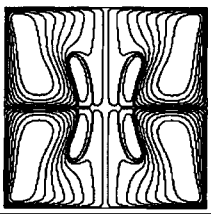
2400	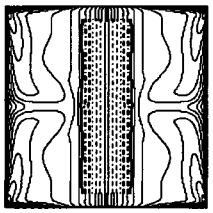	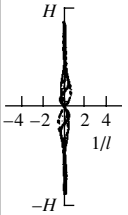	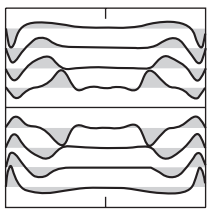	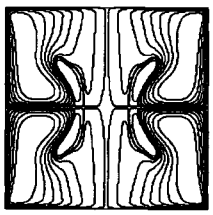

Table

component vortex filaments distort the flow pattern as compared to that induced by a hypothetical vortex ring, but the distortion is not so strong as to modify the translational character of the axial flow toward the lids. Probably, this explains why no recirculation zones were observed in the system [7].

A significantly different pattern of the vorticity distribution is observed when the lids are rotating in the same direction (Fig. 2c). In this case, a system of almost cylindrical vortex tubes closed on the rotating lids is formed in the middle region of the flow. The symmetric toroidal families of the vortex tubes are displaced toward the periphery of the cylinder (the boundary is indicated by the dashed line). The velocity field in this system is determined by three vortex structures. The influence of the two toroidal vortices seems to be analogous to that described above, inducing an axial velocity component directed toward the rotating lids. The effect of the central vortex structure upon the velocity field can be ambiguous: this vortex can induce various types (convex versus concave) of axial velocity profiles depending on the twist sign in the vortex filaments of which the columnlike vortex tubes are composed [3–5].

Let us consider this situation in the case when $\gamma = 1$ and $h = 1$. The influence of a small radial vorticity component will be ignored. The intensity of swirling of the vortex lines "wound" onto the almost cylindrical surfaces of the central vortex tubes will be expressed by the inverse local pitch of the helical vortex line: $1/l = r\tan\beta = r\omega_\varphi/\omega_z$, where β is the angle between the vor-

ticity vector and the vertical direction (Fig. 1). The calculated variation of the flow pattern depending on the increasing Reynolds number is illustrated in the table. The first column indicates the vortex tubes along which the $1/l$ value was calculated. The results of these calculations are presented in the second column by lines of the same kind.

For a small Reynolds number (Re = 150), the upper part of the flow features a vortex structure with a right-handed helical symmetry ($l > 0$), while the lower part features an analogous structure with the left-handed helical symmetry ($l < 0$). These vortices induce either convex and concave profiles, respectively (axial velocity profiles are concave toward the rotating lids as well as those for the peripheral toroidal vortices shown in the third column of the table).

As the speed of the lid rotation increases (Re = 400), the helical vortex symmetry exhibits a spontaneous change, so that the upper and lower vortices become left- and right-handed, respectively. These vortex structures induce the axial flow in the opposite direction: from rotating disks toward the center [3–5]. In a superposition with the flow induced by the toroidal vortices, this yields an axial velocity profile with a minimum at the axis. Further increase in the rotation speed (Re = 500) still increases the degree of vortex filament swirling (decreases the pitch), enhances the induced counterflow, and leads to the formation of bubbles, representing the zones with the fluid moving in the reverse direction (see the fourth column in the table).

Another change in the vortex symmetry is observed for Re = 1300. This effect involves the inner vortex tubes of the structure under consideration. In contrast, the outer tubes of the columnlike structure show an increase in the degree of swirling for the vortex lines in the left- and right-hand directions in the upper and lower cylinder parts, respectively. As a result, the counterflow zone shifts away from the axis toward this region and the recirculation zone transforms into a ring (rather than into a bubble).

On further increasing the rotation speed (Re = 2400), the recirculation ring shifts farther to the periphery and occurs outside the central vortex structure; as a result, the central structure exhibits virtually no swirling of the vortex lines. Now, similar to the Rankin vortex [3], this structure comprises almost straight vortex lines and does not induce any axial velocity component, which is virtually zero in the whole paraxial region. It should be noted that the middle horizontal cross section is a boundary of changes in the helical vortex line symmetry and only the L-transition was observed in all cases (Fig. 1a), in agreement with the experiment [3].

Thus, we have studied the swirl flows in a cylindrical cavity and established a relationship between the formation of recirculation zones and the appearance of a left-handed vortex structure in the flow. This pattern corresponds to the same scenario of the vortex breakdown as that obtained previously for the swirl flows in the tubes [4, 5]. The alternation of the right- and left-handed vortices with increasing Reynolds number suggests that a spontaneous change in the degree of swirling in coherent vortex structures may be a reason for oscillations in the free turbulent flows. Finally, it should be noted that the results concerning the possible formation of closed zones of recirculation motion and the existence of a limiting swirling (twist) of the vortex filaments, after which the helical vortex symmetry exhibits a change, are evidence for (rather than against) further development of the aforementioned mechanical analogies [6].

Acknowledgments. This study was supported by the Russian Foundation for Basic Research (project no. 01-01-00899) and by the INTAS Foundation (grant no. 00-00232).

REFERENCES

1. S. Leibovich, Annu. Rev. Fluid Mech. **10**, 221 (1978).
2. O. Lucca-Negro and T. O'Doherty, Prog. Energy Combust. Sci. **27** (4), 431 (2001).
3. S. V. Alekseenko *et al.*, J. Fluid Mech. **382**, 195 (1999).
4. V. L. Okulov, Pis'ma Zh. Tekh. Fiz. **22** (19), 47 (1996) [Tech. Phys. Lett. **22**, 798 (1996)].
5. T. O. Murakhtina and V. L. Okulov, Pis'ma Zh. Tekh. Fiz. **26** (10), 66 (2000) [Tech. Phys. Lett. **26**, 432 (2000)].
6. V. P. Dmitriyev, Nuovo Cimento A **111** (5), 501 (1998).
7. M. Brons, L. K. Voigt, and J. N. Sorensen, J. Fluid Mech. **401**, 275 (1999).
8. J. N. Sorensen and T. P. Loc, Int. J. Numer. Methods Fluids **9**, 1517 (1989).
9. A. Y. Gelfgt, P. Z. Bar-Yoseph, and A. Solan, J. Fluid Mech. **311**, 1 (1996).

Translated by P. Pozdeev

Technical Physics Letters, Vol. 28, No. 1, 2002, pp. 59–60. Translated from Pis'ma v Zhurnal Tekhnicheskoĭ Fiziki, Vol. 28, No. 2, 2002, pp. 45–49.

Radiation-Induced Optical Emission Quenching in Light-Probed Silica Core Fibers

P. V. Demenkov, O. A. Plaksin, V. A. Stepanov, and P. A. Stepanov

Leipunskii Institute of Physics and Power Engineering, State Scientific Center of the Russian Federation, Obninsk, Russia

e-mail: stepanov@ippe.rssi.ru

Received July 5, 2001

Abstract—The radiation-induced visible emission (400–750 nm) intensity in an optical fiber with a KU-1 silica glass core (OH group content, 1000 ppm) was measured in the fiber irradiated in a pulse mode [BARS-6 reactor; pulse duration, 80 μs; dose per pulse, $< 5.5 \times 10^{12}$ cm^{-2} (9 Gy); dose rate, $<7 \times 10^{16}$ cm^{-2} s^{-1} (1.1×10^5 Gy/s)]. The fiber probed by laser pulses (at 532 and 632 nm) with increasing intensity showed a decrease in the radiation-induced emission intensity in the regions of wavelength both greater and lower than and equal to the probing light wavelength. © *2002 MAIK "Nauka/Interperiodica".*

The radiation-induced emission and transient optical absorption in optical fibers subject to radiation affect the optical signal transmission. However, it is usually assumed that neither the radiation-induced emission nor the transient optical absorption levels depend on the light intensity in the fiber. This is a base assumption in the radiation testing of optical fibers, whereby the emission efficiency (i.e., the fraction of the ionizing radiation energy converted into the optical emission energy) and the transient optical absorption are calculated using the results of two measurements: (i) radiation-induced emission intensity and (ii) total intensity of the radiation-induced emission and the probing light transmitted through the fiber [1, 2].

Below we will demonstrate that the intensity of radiation-induced visible emission in KU-1 silica core optical fibers depends on the probing light intensity. Moreover, the probing light affects the radiation-induced emission level irrespective of whether the two wavelengths coincide or not.

A 60-m-long optical fiber with KU-1 silica core (diameter, 100 μm), a fluorine-doped cladding, and acrylate polymer coating was prepared from a material fabricated using a fluorosilicate glass RF discharge deposition technology at the Vacuum Research Center (Institute of General Physics, Russian Academy of Sciences) [3]. The fiber was characterized by measuring the radiation-induced visible (400–750 nm) emission intensity and the total intensity of the radiation-induced emission and a probing laser light transmitted through the fiber. The experiments were carried out according to the standard scheme described elsewhere [2]. The measurements were performed on the fiber irradiated in a pulse mode on the BARS-6 reactor [pulse duration, 80 μs; dose per pulse, $< 5.5 \times 10^{12}$ cm^{-2} (9 Gy); dose rate, $<7 \times 10^{16}$ cm^{-2} s^{-1} (1.1×10^5 Gy/s)]; the time resolution was below 100 ns. The fiber was probed by the light of continuous lasers: a He-Ne laser (radiation power, 1 mW; light wavelength, 632 nm) and an YAG:Nd^{3+} laser (radiation power, 8 mW; second harmonic wavelength, 532 nm). The probing light intensity at the fiber input was less than 0.1 W/cm^2. The middle 20-m-long part of the fiber wound in a coil on a reel was placed in the vicinity of an active reactor zone. The other fiber end was coupled to an MDR-4 monochromator with a photomultiplier tube of the FEU-100 type as the detector.

Figure 1 shows a change in the optical signal intensity at the fiber output in response to the reactor pulse, which was observed when the detector was tuned to a light wavelength (632 or 532 nm) coinciding with that of the probing light. When the probing light intensity is zero, only the radiation-induced emission is detected, the maximum of which always coincides with the neutron pulse peak (Fig. 1, curves *1*). The irradiation process is accompanied by the transient optical absorption, which influences the shape of the transmitted optical signal both in the presence and in the absence of the probing light [2]. When the fiber is laser-probed, the output light intensity at the first instant is proportional to the probing light intensity; the transient optical absorption is manifested by a decrease in the output light intensity observed in the course of irradiation (Fig. 1, curves *2* and *3*).

As can be seen in Fig. 1, the intensity of the radiation-induced emission peak observed in the absence of the probing laser light (curves *1*) is higher than the sum of intensities of the radiation-induced emission and the probing light in the laser probed fiber (curves *2* and *3*). This effect indicates that the radiation-induced emission intensity and/or the optical losses depend on the light intensity in the fiber. If these values are calculated

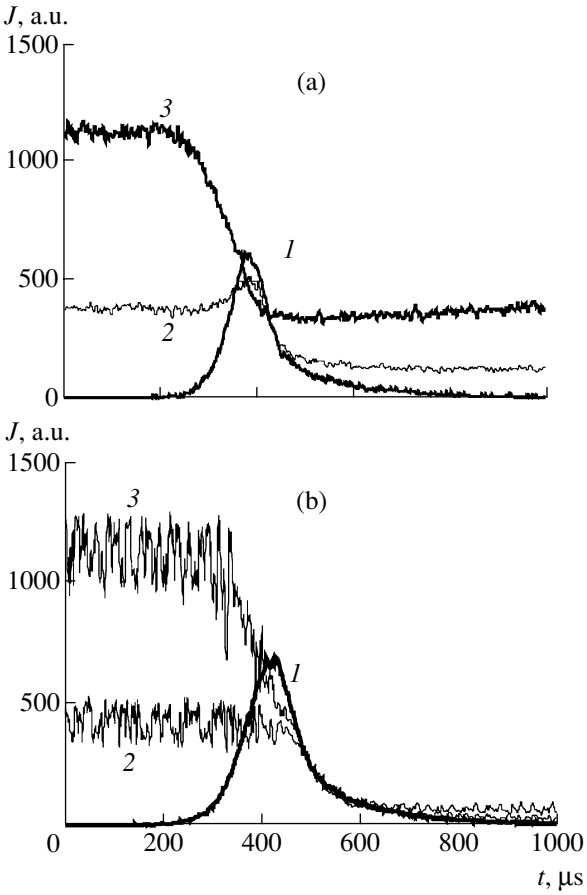

Fig. 1. Time variation of the signal intensity at the optical fiber output measured at (a) 632 nm and (b) 532 nm: (*1*) radiation-induced emission intensity; (*2*, *3*) total intensity of a signal due to the radiation-induced emission and probing laser light transmitted through the fiber.

using the procedure [2] assuming that the contributions of the radiation-induced emission and probing laser light are additive and the optical losses obey the Bouguer law, the optical absorption coefficient turns out to be negative. This result reflects the fact that, when the additional light is introduced into the fiber (by switching on a laser) during the irradiation pulse action, the total output light intensity decreases instead of increasing (as might have been expected in the case of additive contributions).

When the detected wavelength differs from that of the probing laser radiation, the probing light is cut by the monochromator and the only the signal induced by the reactor irradiation pulse is measured by the detector. In this regime, it was found that the probing light switched on during the fiber irradiation suppressed the

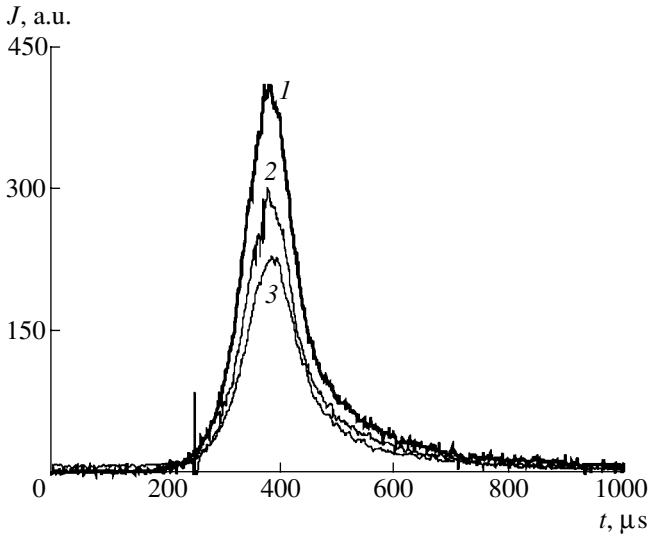

Fig. 2. Time variation of the signal intensity at the optical fiber output measured at 450 nm during the radiation-induced emission pulse (*1*) without laser probing and (*2*, *3*) with laser probing at 532 and 632 nm, respectively.

output signal intensity in the entire visible wavelength range. As can be seen in Fig. 2, the intensity of emission detected at 450 nm decreases upon switching on the probing light (at both 532 and 632 nm). For a maximum probing light intensity ($\approx$0.1 W/cm^2), the output signal intensity dropped 1.5 times.

Thus, the results of our experiments showed that the radiation-induced emission intensity and/or the transient optical absorption in the silica core optical fibers depend on the total light intensity in the fiber. Note that the observed dependence of the radiation-induced optical properties of such fibers irradiated in a reactor is not related to an increase in the absorbed radiation dose due to the laser action. Indeed, the additional dose rate related to the laser radiation in our experiments was below 4×10^{-2} Gy/s against a reactor dose rate of 1.1×10^5 Gy/s.

REFERENCES

1. J. E. Golob, P. B. Lyons, and L. D. Looney, IEEE Trans. Nucl. Sci. **24**, 2154 (1977).
2. P. V. Demenkov, O. A. Plaksin, V. A. Stepanov, *et al.*, Preprint FÉI-2758 (1999).
3. A. S. Biriukov, E. M. Dianov, K. M. Golant, *et al.*, Sov. Lightwave Commun. **3**, 1 (1993).

Translated by P. Pozdeev

Technical Physics Letters, Vol. 28, No. 1, 2002, pp. 6–9. Translated from Pis'ma v Zhurnal Tekhnicheskoĭ Fiziki, Vol. 28, No. 1, 2002, pp. 15–22.

The Role of Nanoclusters of a Crystallizing Component in the Bulk Crystallization Process

F. Kh. Mirzoev[a,*] and L. A. Shelepin[b]

[a] *Institute for Problems of Laser and Information Technologies, Russian Academy of Sciences, Shatura, Moscow oblast, Russia*

** e-mail: mirzo@lazer.nictl.msk.su*

[b] *Lebedev Institute of Physics, Russian Academy of Sciences, Moscow, 117924 Russia*

Received June 9, 2001; in final form, August 2, 2001

Abstract—An analytical model describing the crystallization of substances is proposed, which takes into account the formation of nanoclusters in a supersaturated phase and the appearance and growth of nuclei by means of attachment of the nanoclusters. It is shown that a system in which such a mechanism is operative may feature self-sustained bound oscillations of the supersaturation of crystallizing substances, the density of nanoclusters, and solid phase particle size distribution. Conditions for the appearance and the characteristics of autooscillating structures are determined. *© 2002 MAIK "Nauka/Interperiodica".*

The phase transformations in metastable (supercooled or supersaturated) media and the accompanying autooscillatory instabilities are usually modeled in the approximation of a monomer growth of new phase particles [1–4]. In these models, the structure of the initial metastable phase is not taken into account. However, in view of the development of significant concentration gradients under the action of various factors (in particular, gravity), the stable nucleation and growth of a new phase in strongly oversaturated systems may be preceded by intensive generation and accumulation of clusters of the crystallizing substance [5].

The presence of atomic (or molecular) clusters of a dissolved substance immediately before the onset of a bulk crystallization process is evidenced by numerous data of the electron microscopy and by the IR absorption spectra of supersaturated melts and solutions. Leading to the excitation of autooscillatory structures, these clusters must significantly affect the course of the crystallization process. The typical size of such clusters is about $\bar{r}_c$ = 2–8 nm.

The formation of stable nanoclusters is mediated by bimolecular reactions involving monomers (i.e., molecules or atoms) of the dissolved substance. The clusters are sufficiently mobile and can diffuse in the matrix and combine with one another to form the nuclei of a new crystalline phase. The crystal is a spherical particle composed of nanoclusters. Since the supersaturated phase is composed of monomers and nanoclusters, crystal growth proceeds in the general case by means of attachment of both nanoclusters and monomers by the growing particles [6]. However, in systems with a high initial level of metastability, the elementary events of variation of the crystal nucleus size are primarily the absorption or ejection of nanoclusters.

The scheme of bicluster reactions during crystallization is as follows:

$$K \longrightarrow \alpha_m; \quad \alpha_m + \alpha_m \longrightarrow 2\alpha_m;$$
$$\alpha_m + 2\alpha_m \longrightarrow 3\alpha_m \ldots i\alpha_m + \alpha_m \longrightarrow (i+1)\alpha_m, \qquad (1)$$

where K is the source of clusters, α_m is a single cluster, $2\alpha_m$ is an elementary crystal formed upon merging of two clusters, and $i\alpha_m$ is a crystal assembled from i clusters. Under the conditions of high supersaturation and in the presence of a cluster concentration greater than that in an equilibrium solution, the reverse reactions of decay in scheme (1) are relatively slow and can be omitted.

The cluster growth mechanism according to scheme (1) is characteristic of a rapid crystal growth from solution (for example, at a high initial supercooling or supersaturation), or, on the contrary, this mechanism is operative in the case of a very slow growth under the conditions of a high temperature gradient in the melt at the crystallization front [7].

Consider an open system to which monomers are continuously supplied from an external source, and let the clusters appear in the system as a result of fluctuations of the concentration of the dissolved substance. In turn, the clusters may coalesce under certain conditions to form nuclei of a crystalline phase. The new phase particles are continuously carried away from the nucleation zone under the action of gravity or diffusion. By the nucleation zone, we imply a vicinity of the region of maximum supersaturation (in the general case, inhomogeneously distributed). Particles leaving the nucleation zone tend to decay, thus decreasing the flux of

solid (crystal) phase nuclei capable of further growth. Below we will demonstrate that, under certain conditions, a stationary crystallization regime in such systems becomes unstable with respect to the oscillations in supersaturation, cluster density, and the crystal particle size distribution.

Let us introduce a nonstationary function $f(R, x, t)$ describing the size distribution of the new phase particles, so that $f(R, x, t)dR$ is the number of particles with the radii belonging to the interval $(R, R + dR)$. Let n_1 and n be the concentrations of the dissolved component and nanoclusters, respectively. Behavior of this system can be described within the framework of a model taking into account the rates of variation of the crystallizing substance concentration, nanocluster density, and the particle size distribution function:

$$\frac{\partial n_1}{\partial t} = G(n_1) - 4\pi\bar{r}D_1 n_1 n + D_1\Delta n_1, \quad (2)$$

$$\frac{\partial n}{\partial t} = K(u) - \alpha D_n n^2 - 4\pi\rho_c\int_{R_0}^{\infty} R^2 v f\, dR + D_n\Delta n, \quad (3)$$

$$\frac{\partial f}{\partial t} = -\frac{\partial}{\partial R}(vf) - f\tau_R^{-1} + D_R\Delta f. \quad (4)$$

For the kinetic growth mechanism, whereby the particle size is limited by the kinetic process at the phase interface, the crystal growth rate $v(R)$ is

$$v(R) = dR/dt = \beta D_n n,$$

and the boundary condition for Eq. (4) can be formulated as

$$v(R) f(x, R, t)|_{R = R_0} = \alpha D_n n^2. \quad (5)$$

In Eqs. (2)–(5), β is the growth rate constant; R_0 is the minimum radius of the crystal nucleus; $K(u) = K_0 u^\delta$ is the rate of nanocluster formation (K_0 and δ are constants); $u = (n_1 - n_0)/n_0$ is the supersaturation of the crystallizing solution (n_0 is the equilibrium solution concentration); $G(n_1)$ is the monomer source; $\bar{r}$ is the recombination radius of monomers on clusters; α is the nucleation rate constant; ρ_c is the crystal density; D_1, D_n, and D_R are the diffusion coefficients of the dissolved substance, nanoclusters, and new phase particles; and τ_R is the characteristic time of the new phase particle removal from the nucleation zone.

The first term in the right-hand part of Eq. (2) describes the time variation of the monomer concentration due to the external source action, while the second and third terms reflect the nanocluster formation and the monomer diffusion, respectively. Equation (3) describes the rate of the nanocluster density variation. Here, the first term in the right-hand part takes into account the nanocluster generation as a result of supersaturation, the second and third terms describe the consumption of clusters for the new phase particle formation and growth, and the fourth term reflects the diffusion mobility of nanoclusters. Equation (4) describes the dynamics of variation of the particle size distribution function. In this equation, the first term in the right-hand part takes into account a change in the distribution function due to the crystal phase growth, the second term reflects the flux of particles carried away from the nucleation zone, and the third term allows for the particle diffusion in the coordinate space.

For simplicity, we will assume below that $R_0 \approx 0$ in Eq. (3) and in the boundary condition (5). This is possible because only particles with dimensions markedly exceeding R_0 are responsible for the appearance of the autooscillatory instability development. For the same reason, we ignore the dependence of the growth rate on the particle surface curvature and, hence, neglect the "recondensation" process.

The set of Eqs. (2)–(5) is closed; this system completely describes the appearance of oscillations in the course of a bulk crystallization in the presence of cluster generation in a strongly supersaturated solution or melt. Nonlinearities necessary for positive feedback in such systems are contained in Eq. (2) for the monomer concentration (in the term describing the consumption of monomers for the formation of nanoclusters) and in boundary condition (5) (in the term reflecting the loss of clusters spent for the formation of solid phase nuclei; this term also depends on the cluster concentration via the continuity equation (4) describing the crystal size distribution function).

In the stationary and spatially homogeneous case, system (2)–(5) has a solution (f^s, n_1^s, n^s) determined by the following equations:

$$G(n_1^s) = 4\pi r_0 D_1 n_1^s n^s,$$
$$K(u_s) = \alpha D_n (n^s)^2 + 4\pi\Gamma(3)(n^s)^2\alpha\rho_c D_n (v_s\tau_R)^3, \quad (6)$$
$$f^s = \alpha n^s \beta^{-1}\exp(-\gamma_0 R),$$

where $v_s = \beta D_n n^s$ and $\gamma_0 = (v_s\tau_R)^{-1}$ (the index "s" refers to the stationary values).

Let us consider stability of this solution with respect to small perturbations of the type $(\delta f, \delta n_1, \delta n) = (a_q(w, r), b_q(w), h_q(w))\exp(wt + iqx)$, where q is the wavenumber of these perturbations; a_q, b_q, and h_q are the perturbation amplitudes; and w is the complex increment of the instability.

After linearization with respect to δf, δn_1, and δn, the system of equations (2)–(5) acquires the following form:

$$(w + 4\pi\bar{r}D_1 n^s + D_1 q^2 - G_{n_1})b_q = -4\pi D_1 n_1^s \bar{r} h_q, \quad (7)$$

$$(w + (q^2 + q_c^2)D_n + 2\alpha D_n n^s)h_q = K_{n_1} b_q - 4\pi\rho_c \int_0^\infty R^2 v_S a_q dR, \quad (8)$$

$$(w + q^2 D_R + \tau_R^{-1})a_q + \frac{\partial}{\partial R}(v_s a_q) = h_q \alpha\gamma_0 n^s D_n \exp(-\gamma_0 R), \quad (9)$$

$$a_q|_{R=0} = \alpha\beta^{-1} h_q, \quad (10)$$

where

$$q_c^2 = 4\pi\beta\rho_c \int_0^\infty R^2 f^s dR,$$

$$K_{n_1} = \partial K/\partial n_1^s, \quad G_{n_1} = \partial G/\partial n_1^s.$$

Using Eq. (9) and taking into account the boundary condition (10), we obtain a relationship

$$a_q(w, R) = h_q \frac{\alpha}{\beta}\left(\frac{\gamma - 2\gamma_0}{\gamma - \gamma_0}\exp(-\gamma R) + \frac{\gamma_0}{\gamma - \gamma_0}\exp(-\gamma_0 R)\right), \quad (11)$$

$$\gamma = (w + D_R q^2 + \tau_R^{-1})/v_s.$$

Substituting this expression into (7) and (8) and equating to zero the determinant of the resulting system of homogeneous equations, we arrive at the dispersion equation

$$w + \Omega_0 + \frac{g_1}{w + \Omega_1} + g_2\left[\frac{1}{w\tau_R + D_R\tau_R q^2} + \frac{1}{(1 + w\tau_R + D_R\tau_R q^2)^3}\right] = 0, \quad (12)$$

where

$$\Omega_0 = 2\alpha D_n n^s + D_n(q^2 + q_c^2),$$

$$\Omega_1 = 4\pi\bar{r}D_1 n^s + D_1 q^2 - G_{n_1},$$

$$g_1 = K_{n_1} 4\pi\bar{r}D_1 n_1^s, \quad g_2 = 4\pi\Gamma(3)\alpha D_n \rho_c n^s (v_s\tau_R)^3$$

and $\Gamma(3)$ is the gamma function.

Let us consider the solution of Eq. (12) in two limiting cases. For $g_1\tau_R \gg g_2$, this equation yields the instability increment

$$w_{1,2} = -\delta_1/2 \mp \sqrt{\delta_1^2/4 - \delta_2}, \quad \delta_1 = \Omega_0 + \Omega_1, \quad \delta_2 = \Omega_0\Omega_1 + g_1. \quad (13)$$

Since δ_1 can change sign, while δ_2 is positive for sufficiently large values of g_1 (or K_{n_1}), a transition from the region of stable stationary solutions to the region of instability proceeds as a transition via stable to unstable focus. The system possesses a cycle enclosing the stationary point that does not intersect with the entering phase curves. In this case, we may expect the appearance of an autooscillatory instability for which the decaying oscillations of the supersaturation and nanocluster density fluctuations change to increasing ones. The domain of the oscillatory instability is determined by the inequalities

$$\tau_c^{-1} + \tau^{-1} < G_{n_1} < n_1^s \tau_c (n^s\tau)^{-1} K_{n_1} + \tau^{-1}, \quad q_1^2 < q^2 < q_2^2, \quad (14)$$

where $\tau_c^{-1} = (q_c^2 + 2\alpha n^s)D_n$, $\tau^{-1} = 4\pi\bar{r}D_1 n^s$, and $q_{1,2}^2$ are the roots of the equation $\delta_1^2(q) = 4\delta_2(q)$.

As follows from Eq. (14), the appearance of oscillations in the supersaturation and nanocluster density is favored by an increase in the derivative of the rate of nanocluster formation (K_{n_1}) and by large values of the nanocluster lifetime (τ_c) as compared to the characteristic supersaturation sink time (τ). The oscillation period amounts to $T = 2\pi/\sqrt{|\delta_1^2 + 4\delta_2|}$.

In the other limiting case of $g_1\tau_R \ll g_2$, we can ignore the third term in Eq. (12) in comparison with the terms in square brackets. Then we obtain

$$\Omega_0 - \Lambda(w) = 0, \quad \Lambda(w) = -w - g_2\left[\frac{1}{w\tau_R + D_R\tau_R q^2} + \frac{1}{(1 + w\tau_R + D_R\tau_R q^2)^3}\right].$$

At the boundary of the instability domain, the real part of the increment w is zero and $w = i\Omega$ (Ω is the oscillation frequency). This corresponds to nondecaying oscillations in the particle size distribution function and the nanocluster density. The oscillation frequency can be determined from the condition $\mathrm{Im}(\Lambda(i\Omega)) = 0$, which yields the relationship

$$\frac{1}{(\Omega\tau_R)^2 + (D_R\tau_R q^2)^2} + \frac{3(1 + D_R\tau_R q^2) - (\Omega\tau_R)^2}{((\Omega\tau_R)^2 + (1 + D_R q^2\tau_R)^2)^3} = \frac{1}{g_2\tau_R}. \quad (15)$$

The autooscillatory instability arises when the nanocluster concentration exceeds a critical level:

$$n^s > n^s_* = \left[\frac{\Omega_0[(1 + D_R\tau_R q^2)^2 + (\Omega\tau_R)^2]^3}{4\pi\alpha D_n^4 \rho_c (\beta\tau_R)^3 [3(1 + D_R\tau q^2)(\Omega\tau_R)^2 - (1 + D_R\tau_R q^2)^3]}\right]^{1/4}.$$

If this condition is satisfied, the oscillatory instability arises with respect to perturbations with the frequency Ω and wavenumbers q. Apparently, the appearance of this instability is favored by an increase in the rates of nanocluster formation and crystal growth and in the nanocluster diffusion coefficient, as well as by a decrease in the rate of particle removal (τ_R^{-1}) from the nucleation zone. According to Eq. (15), the oscillation period is determined by the characteristic time of particle removal from the nucleation zone, by the particle growth kinetics, and by the nanocluster concentration and diffusion coefficient.

Thus, we have demonstrated that, under certain conditions, the stationary crystallization regime loses stability and passes to an oscillatory regime, whereby the system features bound oscillations of the crystallizing substance concentration, the density of nanoclusters, and the solid phase particle size distribution. Qualitatively, the nature of these oscillations is related to a competition between the rates of nanocluster formation (in the source) and loss (for the crystal growth), and the rate of removal of the growing crystals from the nucleation zone under the action of external factors (e.g., diffusion). Apparently, these oscillations are responsible for the formation of layered periodic structures in the course of the rapid crystallization of melts after the action of laser radiation upon condensed media [7].

Acknowledgments. One of the authors (F.Kh.M.) gratefully acknowledges the support from the Russian Foundation for Basic Research (project no. 00-02-17664).

REFERENCES

1. Yu. A. Buevich and V. V. Mansurov, Dokl. Akad. Nauk SSSR **319** (4), 862 (1991) [Sov. Phys. Dokl. **36**, 582 (1991)].
2. Yu. A. Buevich, V. V. Mansurov, and I. A. Natalukha, Inzh.-Fiz. Zh. **49** (2), 233 (1985).
3. B. Ya. Lyubov, *Theory of Crystallization in Large Volumes* (Nauka, Moscow, 1975).
4. F. Mirzoev and L. A. Shelepin, Kratk. Soobshch. Fiz., No. 10, 25 (2000); No. 2, 35 (2001).
5. V. V. Regel', A. I. Slutsker, and É. I. Tomashevskiĭ, *Kinetic Nature of Solid Strength* (Nauka, Moscow, 1974).
6. Yu. M. Petrov, *Clusters and Small Particles* (Nauka, Moscow, 1986).
7. *Laser and Electron-beam Processing of Materials*, Ed. by C. W. White and P. S. Peercy (Academic, New York, 1980).

Translated by P. Pozdeev

Technical Physics Letters, Vol. 28, No. 1, 2002, pp. 61–63. Translated from Pis'ma v Zhurnal Tekhnicheskoĭ Fiziki, Vol. 28, No. 2, 2002, pp. 50–55.

The Dynamics of a Quantum Harmonic Oscillator in a Dissipative Environment

V. Yu. Golyshev

Fryazino Branch, Institute of Radio Engineering and Electronics, Russian Academy of Sciences, Fryazino, Moscow oblast, Russia

e-mail: vyug@mail.ru

Received August 24, 2001

Abstract—The time evolution of the full density matrix was studied for a quantum system comprising a quantum harmonic oscillator in a dissipative environment described by a system of oscillators. The problem was solved in the case of a frequency-independent ohmic dissipation for the oscillator in the ground state at the initial time instant. © *2002 MAIK "Nauka/Interperiodica".*

The most important aspect in the dynamics of a quantum macroscopic system is the interaction with a dissipative environment. An example of such a quantum system is offered by the total spin of a mesoscopic magnetic particle interacting with magnetic phonons [1]. The interaction of a macroscopic variable with the environment and the influence of this factor on the quantum properties of the system were studied using various models. The most complete description of such effects can be obtained in terms of the density matrix, the dynamics of which is calculated in a functional-integral approximation employing the Feynman–Vernon influence functionals [2].

Previously, Caldeira and Leggett [3] studied in detail the case of a quantum harmonic oscillator and a free particle with frequency-independent ohmic dissipation. Grabert *et al.* [4] generalized and developed these results for various initial conditions and dissipation types. However, the dynamics of the system density matrix was not studied completely, in particular, for the case of an oscillator not coupled to a thermostat.

Problem formulation. The Hamiltonian of the total system comprising a quantum harmonic oscillator in a dissipative environment can be written as

$$H = H_0 + H_R + H_{0R}, \quad (1)$$

where $H_0 = p^2/2M + M\omega_0^2 q^2/2$ is the Hamiltonian of the unperturbed harmonic oscillator, $H_R = \sum_{n=1}^{N} \frac{1}{2}(p_n^2/m_n + m_n\omega_n^2 x_n^2)$ represents a reservoir containing N harmonic oscillators (with a subsequent transition to the limit $N \longrightarrow \infty$) and $H_{0R} = -q\sum_{n=1}^{N} c_n x_n + q^2\sum_{n=1}^{N} c_n^2/2m_n\omega_n^2$ introduces the dissipative interaction. The last term in H_{0R} corresponds to a change in the unperturbed harmonic oscillator potential caused by the interaction with oscillators in the dissipative environment.

It is assumed that the harmonic oscillator and the reservoir do not interact at the initial moment ($t = 0$), the interaction starting at a time instant $t > 0$. The environment reservoir is coupled to the thermostat setting the temperature T, while the harmonic oscillator does not interact with this thermostat. In this case, it is interesting to follow the dynamics of a truncated density matrix of the oscillator, $\rho(t) = tr_R W(t)$, where $W(t)$ is the density matrix of the total system (comprising the oscillator and the reservoir) and tr_R is the trace of the reservoir coordinates. The initial density matrix W_0 of the total system can be written as a product of the density matrices of independent subsystems: $W_0 = \rho_0 W_R$, where ρ_0 is the oscillator density matrix and $W_R = Z_R^{-1}\exp(-\beta H_R)$ is the canonical density matrix of the unperturbed environment reservoir at a reciprocal temperature $\beta = 1/k_B T$.

The time evolution of the density matrix is described by the following equation:

$$\rho(t) = tr_R \exp\left[-\frac{iHt}{\hbar}\right]\rho_0 W_R \exp\left[\frac{iHt}{\hbar}\right]. \quad (2)$$

Let us assume that the oscillator occurs at the initial time moment in the ground state with the density matrix

$$\rho_0(q, q') = \left(\frac{M\omega_0}{\pi\hbar}\right)^{1/2}\exp\left[-\frac{M\omega_0}{2\hbar}(q^2 + q'^2)\right]. \quad (3)$$

The equilibrium truncated density matrix of the oscillator in thermal equilibrium with the thermostat is [2]

$$\rho_\beta(x, r) = \left(\frac{M}{2\pi\hbar\Lambda}\right)^{1/2}\exp\left[-\frac{M}{\hbar}\left(\frac{1}{2\Lambda}r^2 + \frac{\Omega}{2}x^2\right)\right], \quad (4)$$

where

$$\Lambda = \gamma\pi^{-1}\int_0^{\omega_c} d\omega\omega[(\omega_0^2-\omega^2)^2-(\gamma\omega)^2]^{-1}\coth\left(\frac{1}{2}\omega\hbar\beta\right),$$

$$\Omega = \gamma\pi^{-1}\int_0^{\omega_c} d\omega\omega^3[(\omega_0^2-\omega^2)^2-(\gamma\omega)^2]^{-1}\coth\left(\frac{1}{2}\omega\hbar\beta\right);$$

ω_c is the cutoff frequency of the spectral function of the dissipative environment; $x = q - q'$ is the difference and $r = (q + q')/2$ is the sum of the harmonic oscillator coordinates, respectively; and γ is the ohmic dissipation parameter for which the classical equation of motion of the oscillator acquires the simplest form $\ddot{q} + \gamma\dot{q} + \omega_0^2 q = 0$.

In the weak interaction approximation ($\gamma \ll \omega_0$), expression (4) can be transformed to

$$\rho_\beta(x, r) = \left(\frac{M\omega_0 th\left(\frac{1}{2}\omega_0\hbar\beta\right)}{\pi\hbar}\right)^{1/2} \times \exp\left[-\frac{M\omega_0}{2\hbar}\left(2th\left(\frac{1}{2}\omega_0\hbar\beta\right)r^2+\frac{1}{2}\coth\left(\frac{1}{2}\omega_0\hbar\beta\right)x^2\right)\right]. \quad (5)$$

As is known from the statistical thermodynamics [5], the environment reservoir of oscillators with $N \longrightarrow \infty$ appears as a thermostat for an interacting subsystem and imparts the Gibbs energy distribution to this subsystem. This statement can be proved irrespective of the particular thermostat model by considering a given system as a subsystem of a greater system of the same nature. This was done by Krutkov in the classical case and then generalized to the quantum case [6]. It should be noted that all the aforementioned statements imply neither any particular character of the system coupling to the thermostat nor a special spectral function of the environment reservoir of oscillators. Taking into account that the density matrix most completely describes the dynamics of interaction between the subsystem and the reservoir of oscillators, it is of interest to study the asymptotic behavior of $\rho(t)$ for $t \longrightarrow \infty$ in the case of a reservoir exhibiting ohmic dissipation and to compare the limiting expression to the density matrix (5).

Time evolution of the density matrix. A solution to Eq. (2) at an arbitrary time instant can be written in the following form [4]:

$$\rho(x_f, r_f, t) = \frac{1}{N}\int dx_i dr_i \rho_0(x_i, r_i)\exp\left(\frac{i}{\hbar}\sum(x_f, r_f, t, x_i, r_i)\right), \quad (6)$$

where

$$\sum(x_f, r_f, t, x_i, r_i) = M(x_f r_f + x_i r_i)\frac{\dot{G}_+(t)}{G_+(t)} - M\left(x_i r_f\frac{1}{G_+(t)} + x_f r_i\frac{1}{G_+(t)}\right) + \frac{i}{2}x_i^2\int_0^t ds\int_0^t du K(s-u)\frac{G_+(t-s)}{G_+(t)}\frac{G_+(t-u)}{G_+(t)} + ix_i x_f\int_0^r ds\int_0^t du K(s-u)\frac{G_+(t-s)}{G_+(t)}\frac{G_-(u)}{G_-(t)} + \frac{i}{2}x_f^2\int_0^t ds\int_0^t du K(s-u)\frac{G_-(s)}{G_-(t)}\frac{G_-(u)}{G_-(t)}. \quad (7)$$

In the case of the ohmic dissipation, $K(s) = M\gamma\pi^{-1}\int_0^{\omega_c} d\,\omega\omega\coth\left(\frac{1}{2}\,\omega\hbar\beta\right)\cos(\omega s)$, $G_+(t) = \zeta^{-1}\sin(\zeta t)\exp\left(-\frac{1}{2}\gamma t\right)$, $G_-(t) = \zeta^{-1}\sin(\zeta t)\exp\left(\frac{1}{2}\gamma t\right)$, and $\zeta = \left(\omega_0^2 - \frac{1}{4}\gamma^2\right)^{1/2}$. Substituting expression (7) into (6) and integrating with respect to x_i and r_i, we obtain $\rho(x_f, r_f, t)$.

Since the final expression for the density matrix is rather cumbersome, the result is presented here for the asymptotic limit of $t \longrightarrow \infty$ in a weak interaction approximation ($\gamma \ll \omega_0$):

$$\rho(x_f, r_f, t) = \frac{1}{N}\exp\left[-\frac{M}{2\hbar}\left(\frac{1}{\Lambda_t}r^2 + \Omega_t x^2\right)\right], \quad (8)$$

where

$$\Lambda_t = \frac{\coth(\omega_0\hbar\beta/2)}{2\omega_0} - \frac{\exp(-\gamma t)}{2\omega_0}[\coth(\omega_0\hbar\beta/2) - 1], \quad (9)$$

$$\Omega_t = \Lambda_{eff}\omega_0^2. \quad (10)$$

Here, the quantity Λ_t reflects the mean square deviation of the oscillator coordinate from the equilibrium position and describes behavior of the wavefunction $|\psi(q)|^2$. The time variation of Λ_t calculated for $T = 10\hbar\omega_0/k_B$ and $\gamma = 0.1\omega_0$ is illustrated in the figure, where the solid curve obtained by computer simulation corresponds to the exact expression (6) for the density matrix, while the dashed curve is constructed using the asymptotic formula (9). As can be seen, the two curves coincide with a good accuracy, except for the rapidly decaying

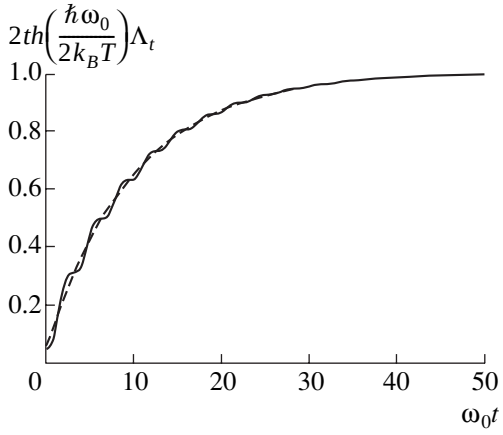

The plots of Λ_t versus time.

oscillations with the frequency of ω_0 missing in the approximation.

Conclusion. Thus, it was demonstrated that the truncated density matrix of the system tends to equilibrium described by solution (5). From this it follows that the dissipative reservoir, which serves as a mediator between the quantum oscillator and the thermostat, does not change the character and temperature of the equilibrium distribution. The dynamics of attaining the equilibrium is exponential, with a characteristic time of γ^{-1}.

REFERENCES

1. V. Yu. Golyshev and A. F. Popkov, Phys. Rev. B **56** (5), 2712 (1997).
2. R. P. Feynman and A. R. Hibbs, *Quantum Mechanics and Path Integrals* (McGraw-Hill, New York, 1965; Mir, Moscow, 1968).
3. A. O. Caldeira and A. J. Leggett, Physica A (Amsterdam) **121**, 587 (1983).
4. H. Grabert, P. Schramm, and G.-L. Ingold, Phys. Rep. **168** (3), 115 (1988).
5. R. P. Feynman, *Statistical Mechanics: a Set of Lectures* (Benjamin, Reading, 1972; Mir, Moscow, 1978, 2nd ed.).
6. D. N. Zubarev, *Nonequilibrium Statistical Thermodynamics* (Nauka, Moscow, 1971; Consultants Bureau, New York, 1974).

Translated by P. Pozdeev

Technical Physics Letters, Vol. 28, No. 1, 2002, pp. 64–65. Translated from Pis'ma v Zhurnal Tekhnicheskoĭ Fiziki, Vol. 28, No. 2, 2002, pp. 56–59.

The Interaction of a Relativistic Dipole Particle with a Flat Surface

A. A. Kyasov

Kabardino-Balkarian State University, Nal'chik, Kabardino-Balkaria, Russia

e-mail: gv_dedkov@kbsu.ru

Received August 23, 2001

Abstract—The electromagnetic interaction of a flat solid surface with a relativistic dipole molecule moving parallel to the surface is studied for the first time. It is demonstrated that the first nonvanishing correction to the stopping force acting upon the particle is proportional to V^2/c^2. In the nonrelativistic limit, the proposed formula coincides with the known result. © *2002 MAIK "Nauka/Interperiodica".*

Recently [1–3], a nonrelativistic theory was developed for the fluctuation-relativistic interactions between moving particles (charges, dipoles, and spherical neutral atoms) and solid surfaces. The purpose of this study was to derive relativistic formulas for the lateral interaction of such a flat surface with a dipole molecule or a charged particle. This is considered as the first step in solving a more complicated problem about the interaction of a neutral relativistic particle with a solid surface.

Let us consider a particle possessing a constant dipole moment (i.e., a polar molecule) and moving along a flat solid surface at a relativistic velocity $\mathbf{V}(V, 0, 0)$. Relativistic formulas describing the transformation of the polarization $\mathbf{P}$ and magnetization $\mathbf{M}$ vectors are as follows [4]:

$$\mathbf{P}_\parallel = \mathbf{P}'_\parallel, \quad \mathbf{P}_\perp = \frac{\mathbf{P}'_\perp + \frac{1}{c}\mathbf{V}\times\mathbf{M}'}{\sqrt{1-V^2/c^2}},$$

$$\mathbf{M}_\parallel = \mathbf{M}'_\parallel, \quad \mathbf{M}_\perp = \frac{\mathbf{M}'_\perp - \frac{1}{c}\mathbf{V}\times\mathbf{P}'}{\sqrt{1-V^2/c^2}}.$$

In a laboratory frame of reference related to the mobile surface, the dipole particle possesses a magnetic moment

$$\boldsymbol{\mu} = \left(0, \frac{V}{c}d'_z, -\frac{V}{c}d'_y\right) \tag{1}$$

and a dipole moment

$$\mathbf{d} = (d'_x\sqrt{1-V^2/c^2}, d'_y, d'_z), \tag{2}$$

where $\mathbf{d} = (d'_x, d'_y, d'_z)$ are the dipole moment components in the particle rest system.

In the laboratory frame of reference, the polarization and magnetization vectors can be expressed as follows:

$$\mathbf{P}(x, y, z, t) = \delta(x - Vt)\delta(y)\delta(z - z_0)\mathbf{d}, \tag{3}$$

$$\mathbf{M}(x, y, z, t) = \delta(x - vt)\delta(y)\delta(z - z_0)\boldsymbol{\mu}, \tag{4}$$

where $\boldsymbol{\mu}$ and $\mathbf{d}$ are the quantities given by formulas (1) and (2), respectively. Thus, in the laboratory frame of reference, the total current related to the dipole particle motion is a sum of the polarization and magnetization currents:

$$\mathbf{j} = \frac{\partial\mathbf{P}}{\partial t} + c\,\mathrm{rot}\mathbf{M}. \tag{5}$$

The work per unit time performed by the induced surface electric field $\mathbf{E}^{in}$ on the current (5) can be determined using the identity [1–3]

$$F_x V = \int \mathbf{j}\mathbf{E}^{in} d^3 r. \tag{6}$$

This expression leads to the following formula for the friction force (the integration in Eq. (6) is performed for the positive components of the wavevectors):

$$\begin{aligned} F_x &= -\frac{2}{\pi}\iint dk_x dk_y \frac{k_x}{q_0}\exp(-2q_0 z_0) \\ &\times [k_x^2 d_x'^2(1 - V^2/c^2) + k_y^2 d_y'^2 + q_0^2 d_z'^2] \\ &\times [\Delta_2(k_x V) - \Delta_1(k_x V)(1 - V^2/c^2)], \end{aligned} \tag{7}$$

where

$$q_0 = q_0(\omega)|_{\omega = k_x V} = \sqrt{k_x^2(1 - V^2/c^2) + k_y^2}, \tag{8}$$

$$q = q(\omega) = \sqrt{k_x^2 + k_y^2 - \frac{\omega^2}{c^2}\varepsilon(\omega)}. \tag{9}$$

1063-7850/02/2801-0064$22.00

It is convenient to introduce the quantity

$$\Delta_R(\omega) \equiv \Delta_2(\omega) - \Delta_1(\omega)(1 - V^2/c^2)$$
$$\equiv \frac{2q_0^2(\varepsilon(\omega) - 1)}{(q_0 + q)(q_0\varepsilon(\omega) + q)} - \frac{q_0 - q}{q_0 + q}(1 - V^2/c^2), \quad (10)$$

which plays the role of a "relativistic" dielectric function.

It is suggested that the velocity of the molecule obeys the inequality (ε' is a real component of the dielectric permittivity)

$$1 - \frac{V^2}{c^2}\varepsilon'(k_x V) > 0. \quad (11)$$

An analogous problem for a relativistic charged particle was previously considered by Garcia-Molina *et al.* [5]. In our notation and the integration variables k_x, k_y (in the paper cited [5], this procedure is performed with respect to k_x and $\omega = k_x V$), the corresponding formula for the friction force F_x is as follows:

$$F_x(z_0, V) = -\frac{2e^2}{\pi}\int_0^\infty\int dk_x dk_y k_x$$
$$\times \frac{e^{-2q_0 z_0}}{q_0}\{\Delta_2''(k_x V) - \Delta_1''(k_x V)(1 - V^2/c^2)\}. \quad (12)$$

A comparison of expressions (7) and (12) shows that (as it might be expected) dependence on the permittivity in both cases is the same.

In the nonrelativistic case ($c \longrightarrow \infty$), expression (7) yields the formula

$$F_x(z_0, V) = -\frac{2}{\pi}\int_0^\infty\int dk_x dk_y k_x \frac{e^{-2kz_0}}{k}$$
$$\times \{k_x^2 d_x^2 + k_y^2 d_y^2 + k^2 d_z^2\}\Delta''(k_x V), \quad (13)$$
$$\Delta(\omega) = \left(\frac{\varepsilon(\omega) - 1}{\varepsilon(\omega) + 1}\right),$$

coinciding with the formula obtained previously [1–3] for a nonrelativistic dipole molecule.

The structure of formula (7) indicates that the significance of the relativistic effects in the friction force is determined only by the parameter V/c while being independent (in contrast to the statement made in [6]) of the distance z_0 from the particle to the surface; the first nonvanishing relativistic correction is proportional to V^2/c^2. In the author's opinion, it is quite evident that the same dependence of the first nonvanishing relativistic correction (V^2/c^2) to the lateral force must take place for a neutral particle (an atom in the *S*-state, spherical particle, etc.)

Recently, Dorofeev *et al.* [7] derived expressions for the force of friction in the case of a neutral spherical particle; these expressions are linear with respect to velocity but contain c^2 in denominator. In the limit of infinite light speed (see formulas (46), (49), (51), and (53) in [7]), these expressions yield zero. This is evidence of the incorrect results reported in [6], since the force of friction in the nonrelativistic approximation is by no means zero [1–3]. Probably, only a relativistic correction to the friction force was calculated in [7] while the main (nonrelativistic term) was missing.

For obtaining a completely clear result, it is necessary to consider the interaction between a flat surface and a neutral particle (fluctuating dipole) and to derive a general expression for the friction force (similar to that derived above for the polar molecule with a constant dipole moment).

REFERENCES

1. G. V. Dedkov and A. A. Kyasov, Phys. Lett. A **259**, 38 (1999).
2. A. A. Kyasov and G. V. Dedkov, Surf. Sci. **463**, 11 (2000).
3. G. V. Dedkov and A. A. Kyasov, Fiz. Tverd. Tela (St. Petersburg) **43** (1), 169 (2001) [Phys. Solid State **43**, 176 (2001)].
4. W. Pauli, *The Theory of Relativity* (Dover, New York, 1981; Nauka, Moscow, 1983).
5. R. García-Molina, A. Gras-Marti, A. Howie, and R. Ritchie, J. Phys. C **18**, 5335 (1985).
6. A. I. Volokitin and B. N. J. Persson, J. Phys.: Condens. Matter **14**, 859 (2001).
7. I. Dorofeyev, H. Fuchs, B. Gotsmann, and J. Jersch, Phys. Rev. B **64**, 035403 (2001).

Translated by P. Pozdeev

Technical Physics Letters, Vol. 28, No. 1, 2002, pp. 66–69. Translated from Pis'ma v Zhurnal Tekhnicheskoĭ Fiziki, Vol. 28, No. 2, 2002, pp. 60–66.

A Relationship between Diffusion and Charge Transfer Parameters in a Binary Melt Formed during Contact Melting

A. A. Akhkubekov and B. S. Karamurzov

Kabardino-Balkarian State University, Nal'chik, Kabardino-Balkaria, Russia

e-mail: rusten@kbsu.ru

Received August 13, 2001

Abstract—Theoretical and experimental data on the mass and charge transfer, charge transfer during contact melting, and hydrodynamic mixing of inert labels introduced into a contact between two dissimilar metals are analyzed and an integral criterion for the charge and mass transfer direction in this system is formulated. According to this criterion, which is valid in all the known binary systems of this type, $\mathrm{sgn}[(\Omega_1 - \Omega_2)(D_1 - D_2)] = -\mathrm{sgn}(z_1^* - z_2^*)$, where Ω_i, D_i, and z_i^* are the atomic volumes, partial diffusion coefficients, and effective charges of light ($i = 1$) and heavy ($i = 2$) components. © *2002 MAIK "Nauka/Interperiodica".*

The process of contact melting [1] in a nonstationary diffusion regime, whereby vertically arranged cylindrical samples are brought into contact in a thermostat and annealed at a certain temperature (with the system component of smaller density placed above the heavier component in order to avoid convection), is successfully used to study the mutual diffusion in melted metals [2], in contact reactive soldering technology, and in some other fields of science and technology.

The mutual diffusion of components in melted metal mixtures is accompanied by the redistribution of mass and charge in the system [3]. A constant electric current passing through a liquid diffusion zone formed as a result of the mass and charge transfer in the course of the contact melting modifies the structure and phase composition of the system and influences the contact melting rate. Using these effects and controlling the contact time and annealing temperature, it is possible to provide for the formation of zones where the material possesses required physicochemical properties [4, 5]. The charge transfer in such systems is also used for the deep purification and enrichment of melts, isotope separation, epitaxial layer growth, and investigation of the charged state of substances.

For successful employment of the charge transfer phenomenon in the aforementioned applications and deeper understanding the relationship between the diffusion of ions and charge transfer in the melt, it is necessary to know the direction of this process. Using the existing criteria (see. e.g., reviews and monographs [6–10]), it is possible neither to predict the effective ion charges in many of the studied systems nor to adequately describe a rather large volume of experimental data available (e.g., those for the systems involving transition metals).

Below we propose a general criterion capable of indicating the direction of charge transfer in binary metal systems, based on a relationship between the charge transfer parameters and other measurable characteristics.

Let us briefly consider the possible factors influencing the separation of ions in the course of the charge transfer in a binary melt.

1. The separation of ions involved in the charge transfer depends on a combination of interrelated factors, including (i) a mismatch of the atomic volumes Ω_i of components involved in the mutual diffusion process, (ii) a difference in the partial diffusion coefficients D_i (or mobilities) of the components leading to the hydrodynamic flow development, and (iii) a possible difference in the effective ion charges z_i^* of the system components.

Apparently, different factors can be operative in various situations. However, it is evident that, on the one hand, a change in any one of these factors leads to alteration of the other two. On the other hand, a change in either one or all three parameters leads to modification of the electron–ion system in the binary melt. However, the contributions to this modification in the electron–ion system related to the change in various parameters can be different. Thus, we may suggest that the quantities Ω_i, D_i, and z_i^* are interrelated.

Investigations of the mutual diffusion accompanying the contact melting, performed by monitoring the motion of inert labels placed in the region of contact between dissimilar metals [11, 12], revealed a phenomenon analogous to the Kirkendall effect for the mutual diffusion between solids. The reason for the displace-

1063-7850/02/2801-0066$22.00

Directions of the charge transfer in binary systems: empirical criterion versus published data

System (1–2)	Differential parameters			Experiment (calculation)				Criterion predicts	
				CNV + CT		CT			
	$\Delta\Omega_{1-2}$	ΔD_{1-2}	Δz^*_{1-2}	Δz^*_1	Δz^*_2	Δz^*_1	Δz^*_2	Δz^*_1	Δz^*_2
Cd–Bi	<0	>0	<0	+	–	+	–	+	–
In–Bi	<0	>0	<0	+	–	+	–	+	–
Sn–Bi	<0	>0	<0	+	–	+	–	+	–
Bi–Pb	>0	>0	<0	–	+	–	+	–	+
In–Cd	>0	>0	<0	–	+	–	+	–	+
Zn–Bi	<0	>0	<0	+	–	+	–	+	–
Zn–In	<0	>0	<0	+	–	+	–	+	–
Zn–Sn	<0	>0	<0	+	–	+	–	+	–
Ga–Sn	<0	>0	<0	+	–	+	–	+	–
In–Sn	<0	>0	<0	+	–	+	–	+	–
Sn–Pb	<0	>0	<0			+	–	+	–
Sn–Cd	>0	>0	<0			–	+	–	+
Sb–Sn	>0	>0	<0			–	+	–	+
*Na–Hg	>0	>0	<0			+	–	–	+
Cd–Hg	>0	>0	<0			+	–	+	–
Sb–Cd	>0	>0	<0			–	+	–	+
Ge–Ag	>0	>0	<0			–	+	–	+
Sb–Zn	>0	>0	<0	Experimental data not available		–	+	–	+
*Al–Zn	>0	>0	<0			–	+	–	+
Cd–Tl	<0	>0	<0			+	–	+	–
In–Tl	<0	>0	<0			+	–	+	–
Zn–Ag	<0	>0	<0			+	–	+	–
Fe–Ni	>0	<0	>0			+	–	+	–
Al–Fe	>0	<0	>0			+	–	+	–
Sb–Bi	<0	0	0			0	0	0	0
Tl–Hg	>0	0	0			0	0	0	0

Note: CNV, convection; CT, charge transfer.

ment of labels in the melt, as well as in the solid phase, is a difference in the partial diffusion coefficients: $D_1 \neq D_2$. This inequality may imply, in particular, different mechanisms of diffusion for various components in the melt [6].

An analysis of the data available in the literature on the charge transfer and mutual diffusion, with an allowance for the hydrodynamic mixing of inert labels during the contact melting, showed that the diffusion of a component with greater atomic volume into that with a smaller atomic volume in the presence of charge transfer in the systems of various types is characterized by the following relationships:

$$\left.\begin{aligned} D_1 - D_2 &> 0 \\ z_1^* - z_2^* &< 0 \end{aligned}\right\} \quad \text{(first group of melts)}, \qquad (1)$$

$$\left.\begin{aligned} D_1 - D_2 &< 0 \\ z_1^* - z_2^* &> 0 \end{aligned}\right\} \quad \text{(second group of melts)}, \qquad (2)$$

$$\left.\begin{aligned} D_1 - D_2 &= 0 \\ z_1^* - z_2^* &= 0 \end{aligned}\right\} \quad \text{(third group of melts)}. \qquad (3)$$

Validity of the inequality $D_1 - D_2 > 0$ (or $D_1 - D_2 < 0$) indicates that the light component is characterized by a higher mobility than the heavy component (or vice versa).

2. Should the mutual diffusion take place in a system with different partial diffusion coefficients, the atomic volumes of the components will change. As a result, the total volume of the liquid will also either decrease (compression) or increase (expansion), since the diffusion is a collective process. This change in the atomic volume gives rise to a nonzero pressure gradient [13] and, hence, to a hydrodynamic flow of the inert labels (tending to reduce the pressure gradient). The direction of motion of the labels depends on the pressure gradient, being opposite in the cases of compression and expansion.

We have analyzed a large volume of the published theoretical and experimental data, including 156 effective charge values (taken from more than 15 sources, including [6, 10, 14–24]; monograph [10] contains the data for 132 systems), in terms of relationships (1)–(3). The results of this analysis allowed us to formulate the following integral criterion for the mass transfer:

—if the hydrodynamic flow of inert labels is directed toward the light component (subscript 1), the component with a greater atomic volume is characterized by a negative effective charge;

—if the hydrodynamic flow of inert labels is directed toward the heavy component (subscript 2), the melt component with a smaller atomic volume is characterized by a negative effective charge;

—if the hydrodynamic flow of inert labels is absent, no field-induced separation of the melt components must take place.

This general criterion yields several particular relationships that are conveniently applied in practice:

(a) If $\Delta D_{1-2} = D_1 - D_2$ and $\Delta\Omega_{1-2} = \Omega_1 - \Omega_2$ are of the same sign, the component with a smaller density is characterized by a negative effective charge.

(b) If ΔD_{1-2} and $\Delta\Omega_{1-2}$ are of opposite sign, the component with a greater density is characterized by a negative effective charge.

(c) If $\Delta\Omega_{1-2}$ and $\Delta\rho_{1-2} = \rho_1 - \rho_2$ are of opposite sign, the light component is characterized by a negative effective charge.

(d) If $\Delta\Omega_{1-2}$ and $\Delta\rho_{2-1}$ are of the same sign, the heavy component is characterized by a negative effective charge.

The above relationships are conveniently written in the following form:

$$\mathrm{sgn}[(\Omega_1 - \Omega_2)(D_1 - D_2)] = -\mathrm{sgn}(z_1^* - z_2^*). \qquad (4)$$

3. Data on the direction of charge transfer predicted using the above criterion for 26 binary systems (selected from a total of more than 160 presently tabulated) are presented in the table. Published data available for some of these systems are given as well. The other experimental results (for the previously uninvestigated systems) were obtained by the method of contact melting with charge transfer. All experiments were performed with metals of special purity grade.

As can be seen from data presented in the table, the signs of the effective charges predicted using the proposed criterion coincide both with the signs determined experimentally using the contact melting technique (systems 1–9) and with the published data.

Using the proposed criterion, it is possible to solve the inverse problem as well and predict the direction of displacement for the inert labels occurring in the region of contact once the effective ion charges of the melt components are known.

The mechanism of charge separation during the mutual diffusion in a melt in the presence of charge transfer is determined by changes in the combination of interrelated parameters, including the atomic volume, partial diffusion coefficients, and effective charges of the melt components. In our opinion, the relationship between the partial diffusion coefficients plays the dominating role.

REFERENCES

1. D. D. Saratovkin and P. A. Savintsev, Dokl. Akad. Nauk SSSR **33** (4), 303 (1941).
2. S. P. Savintsev and A. A. Akhkubekov, Zavod. Lab. **47** (3), 30 (1981).
3. E. V. Kalashnikov, Rasplavy, No. 3, 40 (1990).
4. I. V. Rogov, A. A. Akhkubekov, P. A. Savintsev, and V. I. Rogov, Izv. Akad. Nauk SSSR, Met., No. 2, 66 (1983).
5. I. V. Rogov, P. A. Savintsev, A. A. Akhkubekov, and V. I. Rogov, Metally, No. 1, 56 (1986).
6. D. K. Belashchenko, *Transport Phenomena in Liquid Metals and Semiconductors* (Atomizdat, Moscow, 1970).
7. S. E. Bresler and G. E. Pikus, Zh. Éksp. Teor. Fiz. **28** (10), 2282 (1958).
8. B. V. Fiks, Fiz. Tverd. Tela (Leningrad) **1** (1), 16 (1959) [Sov. Phys. Solid State **1**, 14 (1959)].
9. D. K. Belashchenko, Usp. Khim. **34** (3), 530 (1965).
10. V. A. Mikhaĭlov and D. D. Bogdanova, *Charge Transfer in Liquid Metals: Theory and Applications* (Nauka, Novosibirsk, 1978).
11. N. I. Gavrilov, V. I. Rogov, and P. A. Savintsev, Fiz. Met. Metalloved. **27** (3), 638 (1974).
12. P. A. Savintsev and V. I. Rogov, Zavod. Lab., No. 1, 195 (1969).
13. K. P. Gurov, B. A. Kartashkin, and Yu. É. Ugaste, *Interdiffusion in Multiphase Metallic Systems* (Nauka, Moscow, 1981).
14. E. I. Khar'kov and L. N. Korochkina, Fiz. Met. Metalloved. **32** (2), 259 (1971).

15. D. K. Belashchenko, *Investigation of Melts by Methods of Charge Transfer* (Atomizdat, Moscow, 1974).

16. P. P. Kuz'menko, *Charge, Heat, and Mass Transfer in Metals* (Vishcha Shkola, Kiev, 1983).

17. P. P. Kuz'menko, E. I. Khar'kov, and V. I. Lozovoĭ, Dokl. Akad. Nauk SSSR **160** (6), 1343 (1965).

18. F. P. Golotyuk, P. P. Kuz'menko, and E. I. Khar'kov, Fiz. Met. Metalloved. **1**, 88 (1965).

19. P. P. Kuz'menko, E. I. Khar'kov, L. N. Korochkin, and G. A. Repchenko, Ukr. Fiz. Zh. **12** (3), 467 (1967).

20. A. V. Vanyukov, D. K. Belashchenko, and U. K. Samedinov, Fiz. Met. Metalloved. **29** (1), 182 (1970).

21. I. V. Rogov, A. A. Akhkubekov, and P. A. Savintsev, USSR Inventor's Certificate No. 104394, Byull. Izobret., No. 33 (1983).

22. P. A. Savintsev, V. I. Rogov, A. A. Akhkubekov, *et al.*, USSR Inventor's Certificate No. 1303919.

23. A. A. Akhkubekov, M. M. Baĭsultanov, and S. N. Akhkubekova, Vestn. KBGU, Ser. Fiz.-Mat. Nauk **1**, 181 (1996).

24. A. A. Akhkubekov, M. M. Baĭsultanov, and S. N. Akhkubekova, in *Proceedings of the 1st International Conference "Metallurgy and Education," Yekaterinburg, 2000*, p. 19.

Translated by P. Pozdeev

Technical Physics Letters, Vol. 28, No. 1, 2002, pp. 70–72. Translated from Pis'ma v Zhurnal Tekhnicheskoĭ Fiziki, Vol. 28, No. 2, 2002, pp. 67–73.

The Vortex Formation Determines the Temperature Field during a Submerged Stream Efflux into a Transverse Flow

V. G. Volkov, V. V. Lebedev, and S. O. Shiryaeva

Yaroslavl State University, Yaroslavl, Russia

e-mail: shir@uniyar.ac.ru

Received March 16, 2001; in final form, July 24, 2001

Abstract—By numerically modeling the efflux of a weak submerged stream into a transverse flow possessing a higher temperature, it is shown that the resulting temperature field is strongly affected by a pairwise vortex structure appearing in the vicinity of the efflux site, where the stream interacts with the main flow. This effect was previously reported only for intense transverse streams. *© 2002 MAIK "Nauka/Interperiodica".*

Introduction. A promising approach to protecting streamlined surfaces against the action of high-temperature and chemically aggressive gas flows consists in using hydrodynamic methods whereby a cooling or otherwise protecting gas is injected into the near-wall region through the surface to be protected. In particular, this situation takes place in projecting a gas screen cooling the blades of nozzle assemblies in high-temperature gas turbines and in some aviation and space vehicle constructions [1–3].

A special feature of the problem is the use of rather weak protecting streams, the relative momentum of which is comparable to a specific momentum of the main flow. In this case, the process of mixing of the cooling agent and the main flow occurs in a thin near-wall layer of the medium. To the present, by no means all aspects of this cooling method are rationalized within the framework of strict physical models. This is mostly related to the fact that it is very difficult to obtain exhaustive experimental data on the physical fields in the vicinity of a protected surface without introducing significant distortions into this pattern. In this context, a promising approach to the system analysis is offered by the methods of numerical modeling based on the most general equations.

Model description. In order to analyze the pattern of flow arising upon forming a gas screen by a series of equidistant cooling streams injected into the main transverse flow, we have developed a special program for calculating a three-dimensional turbulent flow. The program is based on a complete system of the Navier–Stokes equations (averaged according to Reynolds), which can be written in the following dimensionless form [4]:

$$\frac{\partial \rho}{\partial t} + \mathrm{div}(\rho \mathbf{V}) = 0,$$

$$\frac{\partial}{\partial t}(\rho \mathbf{V}) + \mathrm{div}(\rho V_n V_m) + \mathrm{grad}\left(p + \frac{2}{3}\rho k\right)$$

$$+ \frac{1}{\mathrm{Re}_0}\left(\mathrm{grad}\left(\frac{2}{3}\mu_* \mathrm{div}\mathbf{V}\right) - \mathrm{div}(2\mu_* S_{nm})\right) = 0,$$

$$\frac{\partial}{\partial t}(\rho H) - \mathrm{div}(\rho \mathbf{V} H) - (\gamma_0 - 1)M_0^2\left[\frac{\partial p}{\partial t} - \mathrm{div}\left(\frac{2}{3}\rho k \mathbf{V}\right)\right]$$

$$+ \frac{(\gamma_0 - 1)M_0^2}{\mathrm{Re}_0}\mathrm{div}\left[\frac{2}{3}\mu_* \mathbf{V}\mathrm{div}\mathbf{V} - 2\mu_* V_n S_{nm}\right]$$

$$- \frac{1}{\mathrm{Re}_0 \mathrm{Pr}_0}\mathrm{div}\mathbf{q} = 0,$$

$$\rho = \frac{1 + \gamma_0 M_0^2 p}{T}.$$

Here, $H = h + 0.5(\gamma_0 - 1)M_0^2 V^2$ is the total enthalpy; h is the enthalpy; p is the dynamic pressure related to the dimensional pressure p' by the relationship $p = (p' - p_0)/(\rho_0 V_0^2)$; V, ρ, and T are the gas velocity, density, and temperature, respectively; μ_* is the effective viscosity equal to a sum of the molecular and turbulent viscosities; k is the kinetic energy of the turbulent flow oscillations; ε is the rate of dissipation of the kinetic energy of turbulent oscillations; and S_{nm} is the deformation rate tensor (symbol "div" denotes the tensor field divergence operator).

The scaling factors entering into the above system of equations are determined by the conventional expressions:

$$\mathrm{Re}_0 = \frac{\rho_0 V_0 L_0}{\mu_0}, \quad \mathrm{Pr}_0 = \frac{\mu_0 C_p}{\lambda_0},$$

$$M_0 = \frac{V_0}{\sqrt{\gamma_0 R T}}, \quad \gamma_0 = \frac{C_p}{C_v}.$$

1063-7850/02/2801-0070$22.00

Here, the subscript "0" indicates the scaling values of the physical quantities characterizing the main flow at the entrance of the spatial region studied: L_0 is the linear scale; Re_0 is the Reynolds number; Pr_0 is the Prandtl number; M_0 is the Mach number; C_p and C_v are the heat capacities at constant pressure and volume, respectively; λ_0 is the thermal conductivity; γ_0 is the adiabate exponent; and R is the universal gas constant. The system of equations is closed by a low-Reynolds $k - \varepsilon$ Chen's turbulence model [5].

Modeling results and discussion. Taking into account the translational symmetry of the problem, we may restrict the consideration to a single cell comprising one stream injected into the main flow. This will imply the use of a periodic boundary condition at the side walls of the cell. The configuration of a spatial region studied (elementary cell) is depicted in Fig. 1. The length, width, and height of this cell (expressed in units of the diameter d of a hole through which the stream is injected) amount to $Y^* = 26d$, $X^* = 3d$, and $Z^* = 11.4d$, respectively. The solid wall coincides with the plane $Z = 0$. The axis of the injected stream (side channel) makes an angle α with the wall, deviating toward the Y axis direction.

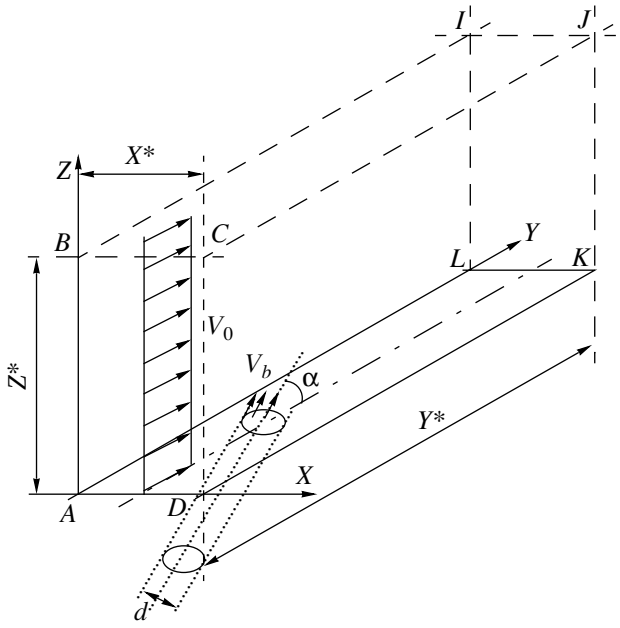

Fig. 1. Calculated flow cell configuration.

At the entrance of the calculated cell (*ABCD* plane), we set the distributions of dimensionless temperature, density, velocity, and turbulence characteristics of the main flow. The exit cross section (*IJKL* plane) was characterized by soft boundary conditions (with zero first derivatives of all parameters in the longitudinal direction). The side edges of the cell (*ABIL* and *DCJK*) obeyed periodic boundary conditions. The top boundary (*BIJC*) was characterized by impermeability, while the bottom (solid wall) was described by the conditions of adherence, zero turbulent viscosity, and adiabaticity ($\partial T/\partial Z = 0$), which is commonly accepted in solving the problems of effective cooling screen design. The condition of impermeability on the top edge is selected in order to provide for the flow core integrity: the heat and mass exchange processes in real systems are localized in the vicinity of the protected wall surface. At the hole exit ($Z = 0$), the injected stream was described by setting homogeneous velocity, density, and temperature profiles.

The calculation was performed for the Mach number $M_0 = 0.3$ and Reynolds number $\mathrm{Re}_0 = 3330$ (determined using the main flow velocity and the injector hole diameter). The ratio of the temperatures of the injected and main flows was 0.5. The injected stream was characterized by the parameter $m = \rho_b V_b/\rho_0 V_0$ varied from 0.5 to 2 (subscript "*b*" refers to the injected stream boundary characteristics at the hole edge). The calculations were performed using a Pentium II PC, each computation variant taking about 20 h. The calculated cell contained about 100 000 sites. The difference scheme was obtained using the conventional methods of control volumes, compressibility scaling, and splitting. The problem was solved using a method based on the vector trials. The difference scheme provided accuracy up to the second order with respect to the spatial variable and to the first order, with respect to time.

Figure 2 shows the projections of the velocity vector on the plane $Y/d = 6.54$, which is perpendicular to the main flow and is situated immediately behind the injector hole, for the injection parameter $m = 1$ and the angle $\alpha = 60°$. The top scale arrow represents the main flow velocity at the entrance of the calculated cell. As can be seen, relatively large values of the transverse velocity components are observed in the vicinity of the wall surface in the region where the injected stream is spread before being oriented by the main flow. Note the regions of rotational motion appearing at the wall surface on the left and right sides of the injected stream. Here (on the leeward stream side), two vortices rotating in the opposite directions are formed as a result of interaction of the stream and the main flow. The larger the injection angle α, the stronger the vorticity manifestations. The most pronounced vortex structure is observed for $\alpha = 90°$.

The formation of a pair of such vortices in the case of strong injected streams was experimentally studied by Kamotani *et al.* [6]. The results of our calculations showed that this phenomenon is also well pronounced for weak injected streams. As the injected stream parameter m decreases, the centers of the two vortices approach one another and the vortex dimensions drop. The vortex formation is also much less pronounced for the streams injected at small angles to the main flow. The vortex formation significantly affects the temperature distribution both in the flow and on the wall, which is related to the fact that vortices trap the cold medium inside and pump the hot medium under the stream.

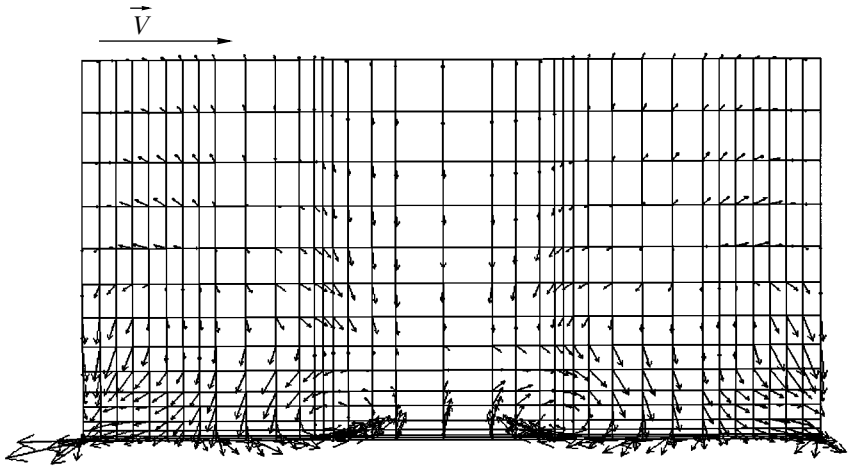

Fig. 2. A diagram showing projections of the flow velocity onto the $Y/d = 6.54$ plane for a stream injected at $m = 1$ and $\alpha = 90°$.

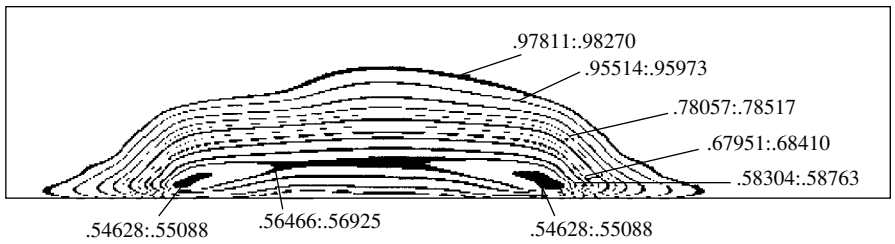

Fig. 3. The temperature field in the cross section $Y/d = 6.54$ for a stream injected at $m = 1$ and $\alpha = 60°$ (figures at the level lines indicate the temperature intervals).

Figure 3 shows a temperature field (in terms of the level lines) in the flow cross section $Y/d = 6.54$ for $m = 1$ and $\alpha = 60°$. Each level line corresponds to a certain temperature interval. The pattern displays local temperature minima situated in the region of the vortex pair, with a warmer medium occurring at the wall. Note that the stream exhibits virtually no thermal axis in the usual sense.

Conclusion. The interaction of a cold submerged stream with a surging transverse flow possessing a higher temperature leads to the formation of a vortex pair in the region of injection and downstream. The presence of these vortices significantly affects the temperature distribution in the flow and on the protected wall surface, since the vortices trap the cold medium inside and provide the access of the hot medium to the wall. This phenomenon, previously reported for the intensive streams, is also inherent in relatively weak injected streams.

REFERENCES

1. S. Friendrichs, H. P. Hatson, and W. N. Dawes, Trans. ASME **119** (10), 786 (1997).
2. R. J. Goldstein, P. Jin, and R. L. Olson, J. Turbomach. **121** (4), 225 (1999).
3. V. G. Lushchik and A. E. Yakubenko, Izv. Akad. Nauk, Mekh. Zhidk. Gaza, No. 6, 34 (2000).
4. L. A. Zaĭkov, M. Kh. Strelets, and M. L. Shur, Teplofiz. Vys. Temp. **32** (6), 850 (1994).
5. J. Y. Chien, AIAA J. **20** (1), 33 (1982).
6. Y. Kamotani and I. Greber, AIAA J. **10**, 1425 (1972).

Translated by P. Pozdeev

Technical Physics Letters, Vol. 28, No. 1, 2002, pp. 73–75. Translated from Pis'ma v Zhurnal Tekhnicheskoĭ Fiziki, Vol. 28, No. 2, 2002, pp. 74–80.

High-Efficiency Electron Beam Generation in an Open Discharge without Anode Grid

P. A. Bokhan and D. E. Zakrevsky

Institute of Semiconductor Physics, Siberian Division, Russian Academy of Sciences, Novosibirsk, 630090 Russia

e-mail: zakrdm@isp.nsc.ru

Received August 16, 2001

Abstract—The open discharge of a new type characterized by the continuous electron beam generation efficiency practically exceeding 98% is demonstrated for the first time. The conditions of discharge functioning were determined and the discharge current–voltage characteristics are measured. The results are explained within the framework of a photoelectron mechanism of the electron emission. © *2002 MAIK "Nauka/Interperiodica".*

Glow discharges in which a considerable fraction of the current is carried by fast electrons are widely used for the excitation of lasers [1], as well as in many other technological applications [2]. A common disadvantage of these devices is a sharp drop in the working voltage and in the electron beam generation efficiency η with increasing working gas pressure. For this reason, the pressure (with respect to helium) is typically restricted to ~10^{-1} Torr in technological discharge devices [2] and to ~1 Torr in lasers [3]. The general reason for this decrease in efficiency of the electron beam generation is a drop in the ion- and fast-atom-induced electron emission coefficients with decreasing energy [2], which results in that η drops to 60% already at a helium pressure of p_{He} ~ 1 Torr [3].

The discovery of a discharge now referred to as the open discharge [4], in which the main source of electrons is photoemission [5], allowed the range of working pressures and working media in the electron-beam-pumped lasers to be significantly increased [6, 7]. In the open discharge devices, a high efficiency (η > 90%) is retained at a pressure of up to p_{He} ~ (10–20) Torr in a continuous mode and up to several dozens of Torr in the pulsed mode [8]. However, the need for using an anode grid with limited transmission (~70–80%) leads to a significant decrease in the practical η value for the electron beam generation, thus creating a serious technical problem in the development of laser cells possessing large volumes and capable of operating at high temperatures.

Here we report on the first experiments with a discharge structure of the open type in which the anode unit does not trap electrons, which allowed us to reach in practice η > 98% in a continuous operation mode at p_{He} ~ 10 Torr. The main difference of the proposed open discharge structure from the traditional systems consists in the method of suppressing the ion current j_i to the cathode. In the traditional open discharge scheme, a decrease in j_i is provided by a small (d ~1 mm) cathode–anode gap [9]. The optimum parameter ($p \times d$) in the traditional system is ~2 Torr cm for a pulsed open discharge in helium [10] and ~1 Torr cm for the continuous open discharge, which coincides with the ($p \times l_c$) ~ 1 Torr cm known for a normal glow discharge (l_c is the length of the cathode potential fall region). In our system, the ion current is suppressed using a dielectric lattice with a small characteristic spacing between walls of the current-carrying channel, which is mounted in the cathode–anode gap. The ions drifting toward the cathode are lost on the channel walls as a result of the ambipolar diffusion. As a result, the ion current to cathode sharply decreases and the η value increases.

Figure 1 shows a schematic diagram of a cell implementing the open discharge without anode grid. The

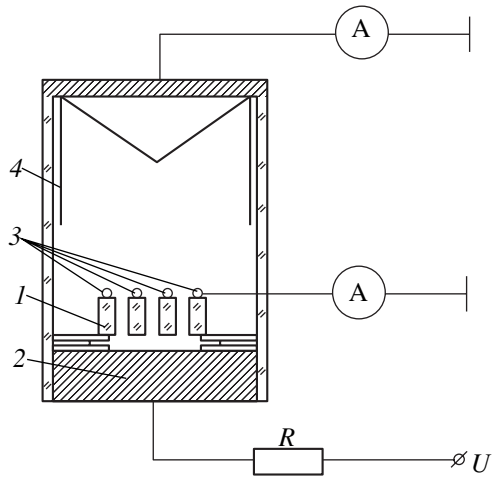

Fig. 1. A schematic diagram of the gas discharge cell realizing the open discharge without anode grid (see the text for explanations).

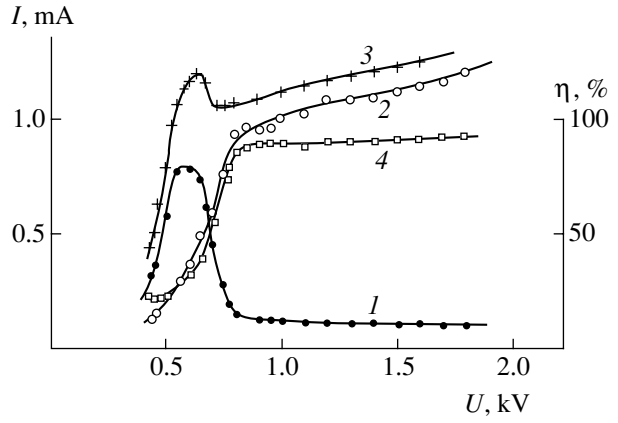

Fig. 2. Variation of the discharge parameters with increasing working voltage U in the open discharge at p_{He} = 8.3 Torr: (*1*) anode current; (*2*) collector current I_e; (*3*) total current; and (*4*) electron beam generation efficiency η.

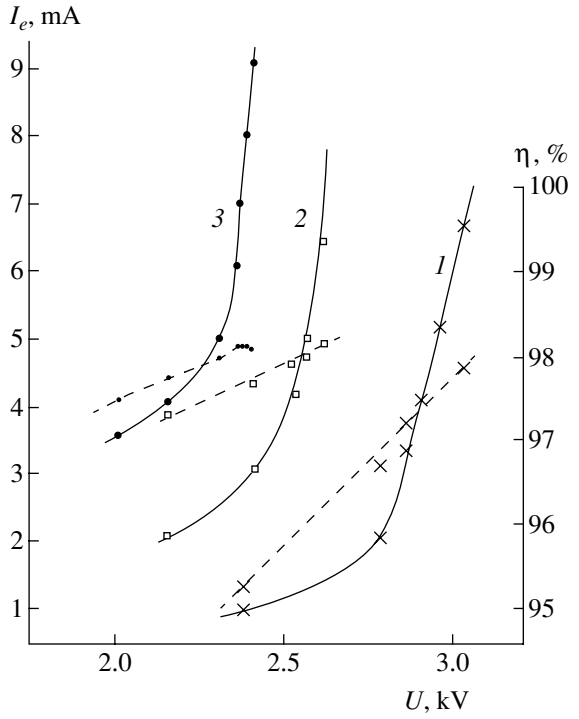

Fig. 3. The plots of collector current I_e (solid curves) and electron beam generation efficiency η (dashed lines) versus voltage U at various working gas pressures p_{He} = 8 (*1*), 9 (*2*), and 10 Torr (*3*).

main element of this discharge structure are dielectric (quartz) plates *1* spaced by 1 mm from a stainless steel cathode *2*. The quartz plates are 5 mm high, 3 mm wide, 20 mm long, and are spaced 3 mm apart. For a working cathode surface diameter of 18 mm, the area of the open part (not shielded by plates *1*) is ~1 cm^2. The Mo anode rods *3* are 2 mm in diameter. For this reason, the fast electrons freely pass between the quartz plates to strike the electron collector *4*. The distance between anode and the nearest collector edge is 2–8 cm, the collector diameter is 34 mm, and the total length of the drift space is 10 cm. The experiments were performed in a weak (~0.2 cm^3/s) flow of the working gas. The working medium was high-purity helium additionally purified on an activated charcoal trap cooled with liquid nitrogen. Without such an additional purification of helium, the system parts not subject to the ion bombardment are contaminated and (within a few tens of hours) the electron beam generation efficiency decreases.

Figures 2 and 3 show typical current–voltage (*I–U*) characteristics of the discharge studied. As can be seen, the *I–U* curves reveal four sharply differing regions corresponding to various working voltages U. In the region from the discharge initiation threshold (~420 V) to $U \leq$ 600 V, the system features the usual anomalous discharge (see Fig. 2) characterized by steep *I–V* buildup and a typical electron beam generation efficiency of 20–30%. The transition from anomalous to open discharge takes place in the region from 600 to 800 V, which is distinguished by a sharp decrease of the anode current (compensating the ion current to cathode) and by an increase in the electron beam generation efficiency. The anode current drop is so large that it gives rise to a descending total current region in the *I–U* curve. The position and magnitude of the anode current maximum and the total current minimum strongly depend on the working gas pressure and purity as well as on the state of the cathode surface. The cleaner the experimental conditions, the sharper the transition regions. The region of voltages $U \geq$ 800 V corresponds to a well-developed open discharge characterized by a slow growth in the current and the electron beam generation efficiency. For an electron collector length of ~2 cm, application of the transverse magnetic field deviates the electron beam toward the cell wall and can completely suppress the current to the collector.

As the voltage increases further, the character of variation of the electron beam generation efficiency is retained (Fig. 3). Beginning with some U (depending on p_{He}), the electron beam current growth changes from slow to fast. The higher the working gas pressure, the more pronounced is the current growth with increasing voltage. A prolonged (several tens of hours) operation of the cell at a reduced p_{He} and increased currents and voltages is accompanied by a gradual rise of the voltage and a decrease in the electron beam generation efficiency, which eventually stabilizes on a significantly lower level (70–80%). Examination of the cathode surface showed evidence of a considerable erosion, mostly in an 0.5-mm-wide central part of the gap between plates *1*. The eroded area exposed a clean, bright cathode metal surface typically resulting from the ion etching. In contrast, the cathode surface at the periphery was strongly contaminated. It was suggested that the contamination resulted from decomposition of the

K-400 sealing glue composition used for the cell hermetization.

The results can be well interpreted within the framework of a photoelectron model of the open discharge. This is confirmed by the following experimental facts.

1. An extremely high electron beam generation efficiency: for p_{He} = 8.5–9 Torr and an electron beam current density of j_e = 5–7 mA/cm^2, the efficiency reaches η = 98.3%. This corresponds to the ratio j_e/j_i = 58, which can be provided (at an anode voltage of 2.5–3 kV) only by the photoelectron emission mechanism. A deep suppression of the ion current to cathode results in that the total current density in the open discharge is lower by more than three orders of magnitude as compared to that in the anomalous discharge (j_{AD} = $2.5 \times 10^{-12} p_{He}^2 U^3$ [11]) and by three orders of magnitude as compared to the high-voltage glow discharge with the electron beam [3] (in the latter two cases, the electron beam current was mostly due to the electron emission induced by heavy particles).

2. A strong dependence of the electron beam current j_e on U (Fig. 3) at a voltage above a certain level ($j_e \sim$ const $\times U^{21}$ for $I > 6$ mA at p_{He} = 10 Torr), which makes it necessary to employ a ballast resistor that stabilizes the open discharge operation. This is explained by the fact that a discharge with dominating photoemission, as well as any normal glow discharge, must be unstable (in the first approximation) with respect to the voltage U.

3. A strong contamination of the cathode surface not subject to ion etching leads to a decrease in the photoelectron current contribution, an increase in the working voltage, and a drop in the electron beam generation efficiency. On the contrary, in the case of ion-induced electron emission, the electron beam generation efficiency always grows with increasing voltage.

Thus, we have demonstrated the realization of an open discharge in which the electron beam generation efficiency in practice exceeded 98%.

REFERENCES

1. I. G. Ivanov, E. L. Latush, and M. F. Sém, *Ion Metal Vapor Lasers* (Énergoatomizdat, Moscow, 1990).
2. M. A. Zav'yalov, Yu. E. Kreĭndel', A. A. Novikov, and L. P. Shanturin, *Plasma Processes in Technological Electron Guns* (Énergoatomizdat, Moscow, 1989).
3. J. J. Rocca, J. D. Meyer, Z. Yu, *et al.*, Appl. Phys. Lett. **41** (9), 811 (1982).
4. P. A. Bokhan and A. R. Sorokin, Zh. Tekh. Fiz. **55** (1), 88 (1985) [Sov. Phys. Tech. Phys. **30**, 50 (1985)].
5. A. P. Bokhan and P. A. Bokhan, Pis'ma Zh. Tekh. Fiz. **27** (6), 7 (2001) [Tech. Phys. Lett. **27**, 220 (2001)].
6. P. A. Bokhan and A. R. Sorokin, Opt. Quantum Electron. **23** (4), 523 (1991).
7. S. V. Arlantsev, B. L. Borovich, V. V. Buchanov, *et al.*, J. Russ. Laser Res. **16** (2), 99 (1995).
8. G. V. Kolbychev, Opt. Atmos. Okeana **6** (6), 635 (1993).
9. P. A. Bokhan, Zh. Tekh. Fiz. **61** (6), 61 (1991) [Sov. Phys. Tech. Phys. **36**, 620 (1991)].
10. P. A. Bokhan and G. V. Kolbychev, Pis'ma Zh. Tekh. Fiz. **6** (7), 418 (1980) [Sov. Tech. Phys. Lett. **6**, 180 (1980)].
11. K. A. Klimenko and Yu. D. Korolev, Zh. Tekh. Fiz. **60** (9), 138 (1990) [Sov. Phys. Tech. Phys. **35**, 1084 (1990)].

Translated by P. Pozdeev

Technical Physics Letters, Vol. 28, No. 1, 2002, pp. 76–79. Translated from Pis'ma v Zhurnal Tekhnicheskoĭ Fiziki, Vol. 28, No. 2, 2002, pp. 81–89.

High-Efficiency Subnanosecond Microwave Pulse Generation in a Relativistic Backward Wave Tube

S. D. Korovin, G. A. Mesyats, V. V. Rostov, M. R. Ul'maskulov, K. A. Sharypov, V. G. Shpak, S. A. Shunailov, and M. I. Yalandin

Institute of Electrophysics, Ural Division, Russian Academy of Sciences, Yekaterinburg, Russia
Institute of High-Current Electronics, Siberian Division, Russian Academy of Sciences, Tomsk, Russia
e-mail: yalandin@ief.uran.ru
Received August 13, 2001

Abstract—The regime of nonstationary oscillations with a short-time power burst, which is typical of the initial stage of a transient process developed when a beam current significantly exceeds the starting level, is studied in a relativistic backward wave tube (BWT) operating in the millimeter wavelength range. The results of numerical calculations allowed conditions to be established that provide for a nearly 90% efficiency of the power transfer from an electron beam with the parameters 300 keV, 2 kA, 1 ns to the microwave pulse with a duration of 8–10 periods of the microwave field oscillations. The experiments showed the possibility of generating such pulses with a width of 200–250 ps and a power of up to ~400 MW at a central frequency of about 38 GHz. © *2002 MAIK "Nauka/Interperiodica".*

Introduction. The possibility of a sharp initial power burst in a backward wave tube (BWT), up to a level several times that corresponding to a stationary generation regime, was pointed out by Ginzburg *et al.* [1]. Although this oscillation regime was experimentally realized, showing a relatively high peak power level (on the order of 100–200 MW) in a wavelength range of 8 mm [2–5] and 3 cm [6], all possibilities of increasing the electron beam efficiency were by no means exhausted. For a traditional scheme of the relativistic BWT employed, with a corrugated slow-wave structure (SWS) in which the wave reflection on the cathode side is provided by a below-cutoff waveguide section, the main power limitations in the first peak were analogous to those in the stationary regime. One of the most important factors was apparently the effect of a space charge on the generation efficiency. Another factor limiting the maximum power in the output electromagnetic pulse with a finite spectral width (~10%) was the wave packet dispersion in the SWS.

Below we report the results of numerical modeling and experimental investigation of a relativistic BWT with an increased SWS cross section and with a band reflector for the radiation extraction [7]. This BWT design not only facilitates solving the aforementioned problems, but opens good prospects for attaining a high-efficiency electromagnetic pulse generation at a lower strength of the beam-transporting magnetic field such that $\omega_b \le \omega$, where ω_b is the cyclotron frequency and ω is the circular frequency of the wave. The task of reducing the magnetic field strength is of special importance for realization of the BWT operation in a periodic-pulse mode. For example, the pulse repetition rate in a BWT based on a hybrid high-voltage modulator [8] can reach 10^3 Hz and above.

BWT design and regime modeling. The SWS geometry was developed so as to provide for the BWT excitation at a central frequency of 38 GHz. The design was based on a preliminary calculation using a one-dimensional nonstationary model [1] with an allowance for the experimental data [3–7]. Then the BWT geometry was optimized in a full-scale numerical experiment using the particle-in-cell method (KARAT code) [9]. The total length of the SWS (depicted in Fig. 1a) accommodated 18 corrugation periods. The corrugation amplitude gradually increased over the first nine of these, which was followed by a regular section of six periods with an average diameter of 11.2 mm. The output section comprising three periods with decreasing corrugation amplitude and period ensured a broadband matching to the round waveguide. The geometry of a lumped reflector in the form of a deep groove was selected so as to provide for a possibly low diffraction quality (~3) of the locked TM02 mode. The electrodynamic properties of the reflector were calculated by various methods. The band characteristics were determined using the scattering matrix technique. The reflection coefficient with respect to power was not less than 0.9 in a 16% frequency band. The reflection of a wave packet with the full width at half-maximum (FWHM) ~200 ps was modeled using the KARAT code. It was found that the energy transmitted through the band filter did not exceed 2%.

The microwave generator was simulated using a self-consistent vacuum diode model. The accelerating voltage pulses applied to the cathode had a trapezoidal

1063-7850/02/2801-0076$22.00 © 2002 MAIK "Nauka/Interperiodica"

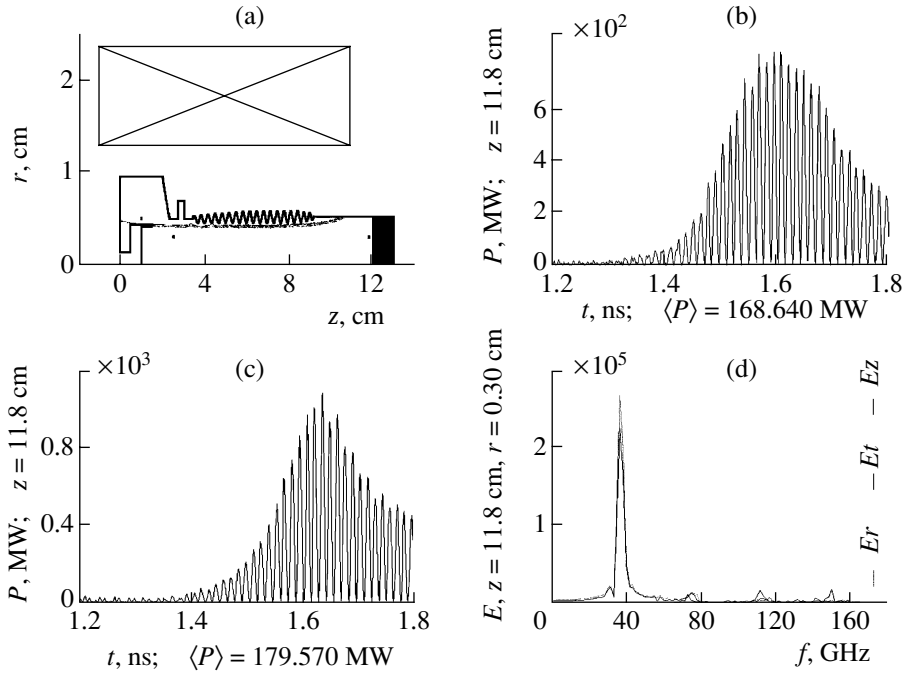

Fig. 1. The results of numerical modeling of a BWT generating subnanosecond pulses: (a) electron injector and SWS geometry; (b, c) non-averaged power flux of microwave pulses for a beam-transporting magnetic field strength of 2 and 5.5 T, respectively; (d) typical spectrum of a subnanosecond microwave pulse.

shape with 150-ps-wide leading and trailing fronts and 1-ns-wide central flat part. This pulse shape was close to that realized in the experiment described below. Figures 1b and 1c shows the (nonaveraged) power flux in the SWS output cross section behind the beam collector for two values of the external magnetic field strength. The results of the numerical experiment were used to select the optimum reflector position relative to the SWS, the SWS length, and the inhomogeneous resistance profile for the beam coupling with a synchronous spatial harmonic. It was found that variation of the reflector position was accompanied by a much smaller change (20–30%) in the first radiation peak power as compared to that observed in the case of a stationary generation regime [6, 10]. This is explained by the fact that, within a relatively short period of time during which the maximum wave amplitude is attained, the field strength in the vicinity of the reflector does not reach the maximum value and the reflector does not perform the modulating gap function. The modulating effect was nevertheless quite pronounced, influencing to a greater extent the microwave pulse duration. It should be also noted that the peak power could be increased in the model calculation by a factor of 1.3–1.4 at the expense of a rather moderate profiling of the coupling coefficient at the SWS input.

Thus, the numerical modeling showed that the efficiency of the beam power transmission to the microwave pulse (with a duration of 8–10 FWHM) can be increased up to approximately 85% for a strong magnetic field (5.5 T) and up to about 65% for $B \cong 2$ T (Figs. 1b and 1c).

The optimum geometry found in the numerical experiment for the electron injector, focusing solenoid, and SWS of the microwave generator was reproduced in the experimental setup. The SWS was made of copper by a galvanoplastic method reproducing the model with 20-μm precision.

Experiment. The experiments were performed using a high-current subnanosecond electron accelerator system [11] comprising a small-size high-voltage 5-ns generator of the RADAN-303BP type [12] with an additional inductance–capacitance unit with high-pressure nitrogen dischargers for the voltage pulse compressing and shaping [13], a transforming coaxial line, and a coaxial vacuum magnetically isolated electron diode with an explosive-emission graphite edge tube cathode and a pulsed solenoid (maximum magnetic induction, up to 5.5 T). The accelerator produced a thin-walled tubular electron beam with a diameter of 8.6 mm, a duration (FWHM) of 1.2 ns, a current of up to 2.2 kA, and an electron energy in the drift space of up to 310 keV. The beam energy and current could be controlled by varying the cathode voltage and the accelerating gap width. In our experiments, these parameters were maintained on a level of 290 keV and 2.1 kA, respectively, with a deviation of not greater than 5%, which corresponded to a beam power of ~600 MW.

The accelerating pulses were monitored with the aid of a calibrated capacitive voltage divider (transient time, below 120 ps) and a Tektronix TDS-684B digital

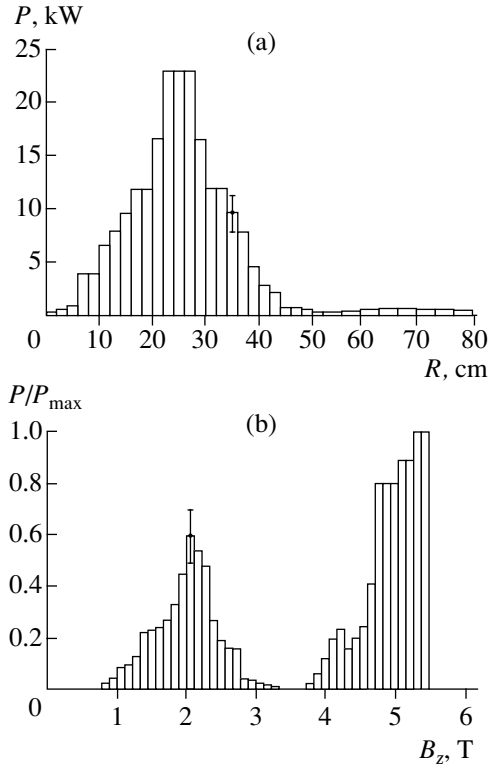

Fig. 2. The experimental BWT characteristics: (a) directivity pattern for the TM01 mode measured by a scanning detector; (b) normalized BWT output power versus transporting magnetic field strength.

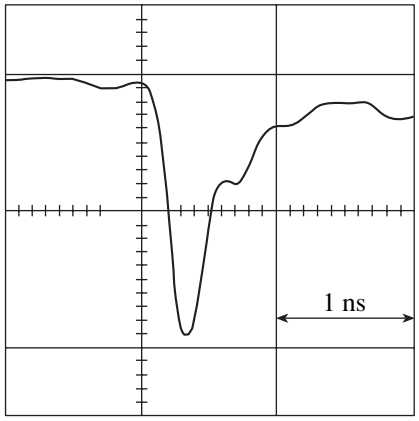

Fig. 3. A typical pulse measured with a germanium microwave detector situated at the maximum of the directivity pattern and monitored by an C7-19 oscilloscope.

oscilloscope (frequency bandwidth, 1 GHz). The beam current probe (Faraday cylinder) was mounted on the edge of a coaxial line (~3 Ω) output-matched to a strip line voltage divider. During the measurements, the probe was installed instead of the SWS into the generator drift chamber.

The output microwave pulses were detected using a noncooled hot-carrier germanium detector calibrated with a meagnetron generator. Previously, such a detector was successfully used to measure the radiation pulses with a front width as small as 75–100 ps [3]. The detector signal was fed to an C7-19 oscilloscope (bandwidth, 5 GHz) with a voltage sweep calibrated to within 5% using test pulses with a front rise time of 90 ps. The delay line in the oscilloscope was based on a broadband cable with porous teflon insulation.

The amplitude attenuation coefficients of the microwave detector cable ducts and the delay line were calibrated and the degree of subnanosecond signal broadening in the measuring tract was estimated using a set of test pulses with an amplitude of 1 V, a front width of 100–200 ps, and a duration (FWHM) of 150–300 ps. The calibration experiments were performed with a Tektronix TDS-820 digital stroboscopic oscilloscope (bandwidth, 6 GHz). The aforementioned calibration measurements were performed with an accuracy no worse than 3–5%.

Results and discussion. The BWT microwave pulse power was determined by integrating the detector signal over the directivity pattern scanned in a horizontal plane at a distance of 2 m from the output horn antenna. The directivity pattern was symmetric and corresponded to the TM01 mode (Fig. 2a). The oscillograms were processed with an allowance for a nonlinear sensitivity of the detector. The region of small amplitudes, where the nonlinearity was small, corresponded to a part of the directivity pattern with a detected power level of up to 5 kW. In this region, distortions of the microwave pulse envelope were insignificant and the detected pulse had a duration (FWHM) of ~200–250 ps. In the receiving antenna position corresponding to the maximum of the main interference ring of the TM01 mode, the detector operated in a nonlinear calibration region and the pulse detected by the oscilloscope exhibited broadening up to 300–350 ps (Fig. 3). This change of the pulse duration required the corresponding variation of the attenuation coefficients in the cable and delay line tracts for calculating the real power measured by the detector, since an overstated pulse duration could result in an excess error during the power measurement at the periphery of the main interference ring. With the error of the oscilloscopic determination of the microwave pulse duration (FWHM) taken equal to 50 ns, the calculation of the total microwave generator power yielded 240–280 MW. These values were obtained by directly integrating over the directivity pattern measured with a transporting magnetic field strength of 2 T (Fig. 2a). It should be noted that, determined for a series of pulses detected for an accelerating voltage amplitude deviation of up to 5%, the mean square deviation of the microwave power values measured by the detector did not exceed 15–18%.

Figure 2b shows a normalized plot of the output microwave power versus the strength of the transporting magnetic field. This diagram was constructed with an allowance for the pulsed field strength in the coil

decreased as a result of the skin effect in the copper SWS wall possessing a characteristic thickness of 1–1.5 mm. The measurements were performed at the reference point of the directivity pattern. As can be seen, the microwave power measured for a magnetic field strength above 5 T increases approximately by half as compared to the power observed with a magnetic field strength of 2 T and reaches 360–420 MW. Note that the change by a factor of 1.5 is much less pronounced in comparison to an analogous dependence [3, 4] obtained previously for an SWS with a characteristic cross-section size ($D \approx \lambda$), where at least a fourfold difference was observed.

Conclusion. It was demonstrated that a relativistic BWT operating in the regime of subnanosecond microwave pulses with a central frequency of 38 GHz can provide for an output peak power of 240–280 MW at a relatively low magnetic field strength (~2 T). With the magnetic field strength increased above 5 T, the measured power of microwave pulses with a duration (FWHM) of 200–250 ps attained up to 400 MW. These results agree quite well with the BWT electron beam power conversion efficiency estimated by numerical modeling. It should be noted that, due to the small pulse duration, no breakdown took place during the experiments in the output window of the microwave generator or inside the slow wave system despite the power flux reaching 300–400 MW/cm^2.

Acknowledgments. The authors are grateful to N.S. Ginzburg, V.P. Tarakanov, I.V. Pegel, and A.I. Klimov for stimulating discussions of the results, valuable advice, and useful remarks.

REFERENCES

1. N. S. Ginzburg, S. P. Kuznetsov, and T. N. Fedoseeva, Izv. Vyssh. Uchebn. Zaved., Radiofiz. **21** (7), 1037 (1978).
2. V. G. Shpak, S. A. Shunailov, M. R. Ul'maskulov, *et al.*, Izv. Vyssh. Uchebn. Zaved., Fiz. **39** (12), 89 (1996).
3. N. S. Ginzburg, N. Yu. Novozhilova, I. V. Zotova, *et al.*, Phys. Rev. E **60**, 3297 (1999).
4. M. I. Yalandin, V. G. Shpak, S. A. Shunailov, *et al.*, IEEE Trans. Plasma Sci. **28** (5), 1615 (2000).
5. M. I. Yalandin, V. G. Shpak, S. A. Shunailov, *et al.*, Pis'ma Zh. Tekh. Fiz. **25** (10), 19 (1999) [Tech. Phys. Lett. **25**, 388 (1999)].
6. V. P. Gubanov, S. D. Korovin, I. V. Pegel, *et al.*, Proc. SPIE **2843**, 228 (1996).
7. I. K. Kurkan, V. V. Rostov, and E. M. Tot'meninov, Pis'ma Zh. Tekh. Fiz. **24** (10), 43 (1998) [Tech. Phys. Lett. **24**, 388 (1998)].
8. M. I. Yalandin, S. K. Lyubutin, S. N. Rukin, *et al.*, Pis'ma Zh. Tekh. Fiz. **27** (1), 81 (2001) [Tech. Phys. Lett. **27**, 37 (2001)].
9. V. P. Tarakanov, *User's Manual for Code KARAT* (Berkeley Research Associates, 1992).
10. S. D. Korovin, I. K. Kurkan, V. V. Rostov, *et al.*, Izv. Vyssh. Uchebn. Zaved., Radiofiz. **42** (12), 1189 (1999).
11. V. G. Shpak, S. A. Shunailov, M. R. Ulmaskulov, *et al.*, in *Proceedings of XI International Conference on High Power Particle Beams, Prague, 1996*, Vol. 2, p. 913.
12. V. G. Shpak, S. A. Shunailov, M. I. Yalandin, *et al.*, Prib. Tekh. Éksp., No. 1, 149 (1993).
13. M. I. Yalandin and V. G. Shpak, Prib. Tekh. Éksp., No. 3, 5 (2001).

Translated by P. Pozdeev

Technical Physics Letters, Vol. 28, No. 1, 2002, pp. 80–81. Translated from Pis'ma v Zhurnal Tekhnicheskoĭ Fiziki, Vol. 28, No. 2, 2002, pp. 90–94.

Development of the Rayleigh–Taylor Instability at the Boundary of a Friable Medium Layer Accelerated by a Compressed Air Flow

M. V. Bliznetsov, I. G. Zhidov, E. E. Meshkov, N. V. Nevmerzhitskiĭ, E. D. Sen'kovskiĭ, and E. A. Sotskov

Institute of Experimental Physics, Russian Federal Nuclear Center, Sarov, Russia

e-mail: root@gdd.vniief.ru

Received September 10, 2001

Abstract—The results of experiments with a friable medium layer driven by a compressed gas flow are reported. A layer of polypropylene particles was accelerated in a square channel under the action of air pressure. The initial perturbation on the unstable layer boundary had a nearly sinusoidal shape. Since the medium possesses no tensile strength (and exhibits no surface tension), the unbound particles occurring in the protruding front regions (spikes) of the unstable layer boundary fall into the gas. In the depressed front regions (bubbles), the medium probably exhibits a certain densification and the resulting compressive strength hinders the bubble growth in the initial stage of instability development. The gas penetrating into the layer leads to expansion and fluidization of the layer. © *2002 MAIK "Nauka/Interperiodica".*

If a boundary between two media moves with acceleration directed normally to the interface from a lighter to heavier component, the boundary exhibits instability of the Rayleigh–Taylor type [1]. There is extensive investigation of such instabilities taking place at the phase boundaries of various types, including gas–gas, gas–liquid, liquid–liquid, gas–solid, etc. It is also of interest to study the case when one phase (or both) represents a friable medium: such fluids are frequently encountered in practice and this analysis can be of considerable value.

The strength of one of the contacting media (or of both media) at an unstable interface is a factor stabilizing the system. However, this factor does not necessarily prevent the development of instability and turbulent mixing. The finite strength implies the existence of critical values of the amplitude and wavelength of the initial perturbation, above which the perturbation can exhibit unlimited growth [2]. Friable media, as well as the usual elastic media, possess a certain compressive strength; however, the former possess virtually no tensile strength, differing in this respect even from liquids exhibiting the surface tension. As a result, the Rayleigh–Taylor instability development at the boundary of a friable medium accelerated by a compressed gas flow exhibits certain special features.

Below we describe the results of experiments on the acceleration of a friable medium layer by gaseous explosion products, which illustrate the aforementioned features of the instability development.

In our experiments, the layer of a friable medium was accelerated by the pressure of gaseous products of an acetylene–oxygen explosive mixture in a square (4×4 cm) vertical channel with transparent walls. The friable medium represented polypropylene (PP) particle with a characteristic average size of $\delta \sim 0.5$ mm. The PP particles were distributed in a ~30-mm-thick layer over a 5-μm-thick lavsan (Dacron analog) film dividing the channel into two compartments. Then an initial two-dimensional perturbation of a nearly sinusoidal shape was created at the unstable boundary between the accelerated layer and the compressed gas flow.

The upper part of the channel, representing a closed chamber, was filled with a stoichiometric mixture of acetylene and oxygen. Detonation of the mixture was initiated simultaneously at 64 points on the square cylinder top edge. The bottom edge of the lower compartment was open to contact with the atmosphere. The flow pattern in the channel was monitored by a high-speed camera.

Figure 1a shows a series of shots illustrating the results of an experiment in which the layer of PP particles was accelerated in the channel by the pressure of gaseous products formed upon explosion of the acetylene–oxygen mixture. The absence of both a tensile strength and the surface tension results in that unbound particles occurring in the protruding perturbed front regions (called spikes) of the unstable layer boundary fall upward into the gas (as viewed by an observer located on the layer boundary), exhibiting acceleration equal to that of the layer (the spike front approximately coincides with the initial upper boundary of the PP layer). In the initial stage, the density of particles falling into the gas is rather low: the spikes appear as quite transparent.

1063-7850/02/2801-0080$22.00

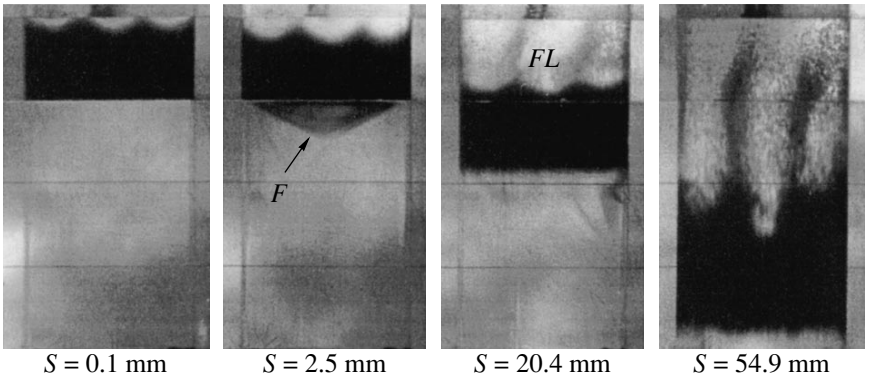

Fig. 1. A sequence of shots illustrating the two-dimensional instability development on the unstable boundary of a friable medium layer (PP particles on a thin supporting film) accelerated by a compressed gas flow (gaseous explosion products) in a square vertical channel: (*FL*) friable layer; (*F*) film supporting the initial layer; (*S*) layer path length (determined by the bottom stable layer boundary).

In the depressed front regions (called bubbles), the friable medium possesses certain compressive strength that apparently completely suppresses the initial bubble growth. In a later stage, the bubbles expand and probably form a fluidized layer. Then the instability development is analogous to the process of the Rayleigh–Taylor instability development at the boundary of a liquid layer accelerated by a compressed gas flow.

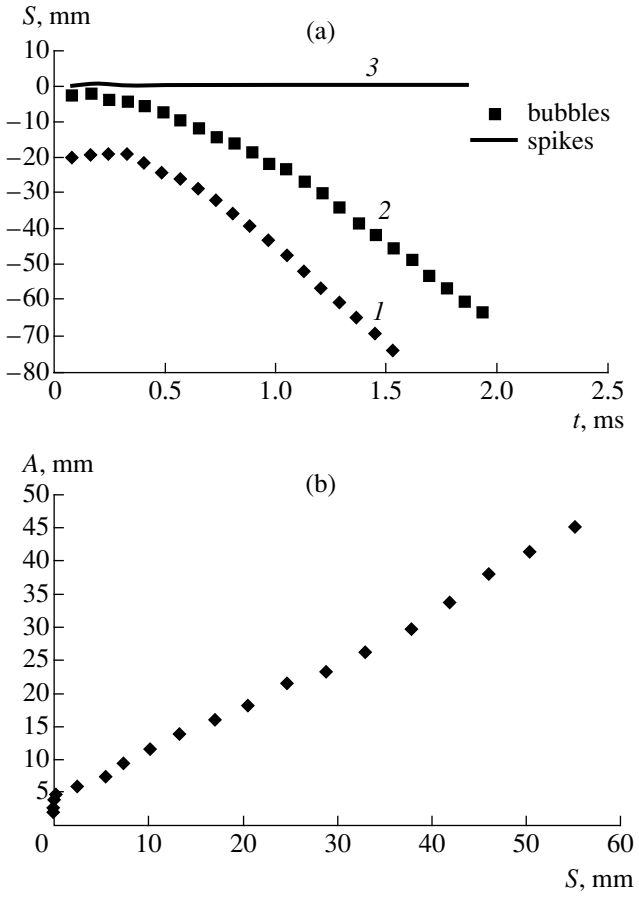

Fig. 2. (a) The *S* versus *t* diagrams illustrating the accelerated layer motion: (*1*) bottom stable layer boundary; (*2*) bubble front; (*3*) spike front. (b) The *A* versus *S* diagram illustrating the perturbation development.

A significant role in the course of the instability development in the system belongs to the stage of compressed gas penetration into the accelerated friable medium layer. The friable medium presents no obstacle to penetration of the gaseous explosion products, which is confirmed by the behavior of the polymer film on which the friable layer initially resides. As can be seen, the compressed gaseous products readily penetrating the friable layer begin to expand the film (*F*), forming a spherical bubble surface (for a layer path length of $S = 2.5$ mm). This bubble breaks for $S = 54.9$ mm, which is followed by expansion of the compressed gas penetrating into the PP layer and by the expansion of the friable layer material.

Figure 2a shows the *S* versus *t* diagrams, where *S* is the layer path length (determined for the bottom stable layer boundary) and t is the time measured from the moment of the onset of layer motion. Figure 2b presents the plot of *A* versus *S*, where *A* is the perturbation amplitude determined on the unstable layer boundary. In an analogous experiment reported by Rogue *et al.* [3], a layer of particles was also accelerated in a vertical shock tube, but the film holding the initial layer was situated on the unstable boundary and hence could influence the instability development.

REFERENCES

1. G. I. Taylor, Proc. R. Soc. London, Ser. A **201**, 192 (1950).
2. A. I. Lebedev, P. N. Nizovtsev, V. A. Rayevsky, *et al.*, in *Proceedings of the 5th International Workshop on Compressible Turbulent Mixing, Stony Brook, USA, 1995*, Ed. by R. Young, J. Glimm, and B. Boston (World Scientific, Singapore, 1996), p. 231.
3. X. Rogue, G. Rodríguez, J. F. Haas, and R. Saurel, Shock Waves **8**, 29 (1998).

Translated by P. Pozdeev